Hydraulic fracturing flowback and produced water as a feedstock for mineral carbonation

by

Bizhou Zhu

A thesis submitted in partial fulfillment of the requirements for the degree of

Master of Science

Department of Earth and Atmospheric Sciences
University of Alberta

ABSTRACT

Hydraulic fracturing and produced water or FPW has potential use as a feedstock to supply divalent Ca and Mg cations for mineral carbonation at standard temperature and pressure. The carbonation potential of real FPW samples produced by oil and gas companies has not previously been tested in laboratory environments under ambient conditions. As such, the effects of pH and pCO_2 on the rate and efficiency of mineral carbonation reactions under ambient conditions were tested in this thesis. The results of this work show that calcite ($CaCO_3$) and aragonite ($CaCO_3$) precipitate from FPW at alkaline pH conditions (i.e., 8.5–12.0) under ambient conditions and atmospheric pCO_2 (i.e., 0.04%). These minerals sequester CO_2 from air. Brucite [$Mg(OH)_2$] and occasional portlandite [$Ca(OH)_2$] precipitate at greater pH from the residual CO_2-depleted FPW and both minerals have potential to capture additional CO_2 owing to their high reactivity. The resulting high purity Ca-carbonate and Ca- and Mg-hydroxide minerals could be used to maximum effect for Carbon Dioxide Removal as part of a Ca- and Mg-looping operation, where the hydroxide precipitates could be regenerated by calcining while CO_2 is stored in underground sedimentary reservoirs. When a higher pCO_2 gas (10%) is injected into FPW titrated to pH 10.5, precipitation of calcite is promoted at the expense of brucite dissolution. The mineral carbonation reactions reach steady-state within 40 minutes of CO_2 injection under these conditions. Although brucite and hydrated Mg-carbonate minerals are undersaturated at pCO_2 = 10%, the maximum amount of CO_2 captured by precipitates was 8× higher than that measured in experiments at atmospheric pCO_2 after 24 hours. Residual Ca remained unreacted in experiments conducted at pCO_2 = 10%, which implies that alkalinity in the FPW limits the extent of CO_2 capture. Therefore, step-wise alkalinity swings, or maintenance of pH >10.5, could be used to drive the carbonation reaction to completion. In addition, the experiments showed that B, Ba, Fe, Mn, Ni, Pb, S, Si, Sr, and Zn are

immobilized by the precipitates during mineral carbonation, which offers an opportunity to recover valuable elements and sequester potentially toxic elements from FPW. Lastly, an assessment of FPW resources suggests that the FPW produced in Canada in 2020 could be used to sequester 151 kt CO_2/year with a value of ~7.55 M CAD under federal carbon pricing which will reach 50 CAD/t in 2022.

PREFACE

Chapter 1 presents an introduction to mineral carbonation and hydraulic fracturing flowback and produced waters. In addition, it provides an overview of existing studies that have utilized hydraulic fracturing flowback and produced water resources for mineral carbonation.

Chapter 2 of this thesis is in preparation for submission to *Environmental Science & Technology* as "Hydraulic fracturing flowback and produced water as a feedstock for carbon dioxide removal or emissions reduction via mineral carbonation". The author designed and conducted the experiments, collected, and analyzed XRD, ICP-MS and SEM data, conducted geochemical modelling, interpreted the data, and wrote the manuscript. S.A. Wilson provided the idea of the project and assisted with designing the experiments, collection of XRD data, data interpretation and manuscript writing. N. Zeyen and M.J. Raudsepp assisted with the collection and interpretation of SEM data and geochemical modelling. B. Wang, K.N. Snihur and K. von Gunten facilitated ICP-MS data collection. B.J. Rostron collected samples from the field sites and assisted with data interpretation. A.L. Harrison contributed to geochemical modelling. D.S. Alessi contributed to samples collection, ICP-MS data collection and interpretation, and geochemical modelling.

Chapter 3 of this thesis is in preparation for submission to *Environmental Science & Technology* as "Accelerating mineral carbonation with hydraulic fracturing flowback and produced water using elevated pCO_2 gas". The author was responsible for designing and conducting the experiments, building the experimental apparatus, collecting, and analyzing XRD, ICP-MS, SEM and alkalinity data, geochemical modelling, data interpretation and manuscript writing. S.A. Wilson provided the idea for the project and assisted with experimental design, the collection of XRD data, data interpretation, and manuscript writing. C.J. Vessey assisted with conducting experiments. K.N. Snihur and S. Safari facilitated the collection and analysis of ICP-

MS data. S. Riechelmann collected the stable isotope data. C. Paulo and I.M. Power contributed to the collection and interpretation of DIC data. N. Zeyen assisted with the experimental design. M. J. Raudsepp assisted with collection and interpretation of alkalinity data. B.J. Rostron assisted project conception and design. D.S. Alessi contributed to project conception and design, collected samples, and contributed to ICP-MS data collection and interpretation.

Chapter 4 presents a summary of the results from the two sets of experiments in this thesis. It also envisions future research directions to efficiently explore the use of existing FPW resources for practical implementation of mineral carbonation at scale.

ACKNOWLEDGMENTS

Foremost, I would like to thank my supervisor, Dr. Sasha Wilson, for her persistent guidance and encouragement during my Master's program. She is a supportive, thoughtful, and cheerful person who creates an inclusive and inspiring research environment. I am inspired by her passion and dedication for the scientific research. I learned from her not only the knowledge and technical skills in the research field, but also the interpersonal skills for future career and enthusiasms for science. I am very grateful that she would always generously provide me resources and freedom to explore what I want to achieve. I would also like to thank my co-supervisor Dr. Daniel Alessi and Dr. Ben Rostron, who provided me the samples for my research and facilities for analyses of my samples.

I would also like to thank everyone in the Environmental Economic Geology Laboratory for their guidance and help in lab works. Particularly, I would like to thank Dr. Maija Raudsepp and Dr. Nina Zeyen for their patience in answering questions regarding to my thesis and lab procedures. I am very grateful for the time that Katherine Snihur, Konstantin von Guten, and Salman Safarimohsenabad contributed for the assistance of my ICP-MS analyses. I would like to thank Mark Labbe for his help in building my experimental apparatus. A warm thank you to Maureen Soon from the University of British Columbia, Dr. Anna Harrison from GET-CNRS, Dr. Sylvia Riechelmann from the Ruhr-Universität Bochum, and Prof. Ian Power and Dr. Carlos Paulo from Trent University for their assistance with my sample analyses. I would like to thank NSERC and Canada Research Chairs Program for providing the funding source for this project.

Finally, I would like to thank my grandmother and the rest of my families overseas in China for their supports during the process of accomplishing this Master's degree.

TABLE OF CONTENT

LIST OF FIGURES

LIST OF TABLES

CHAPTER 1: Introduction

The Paris Agreement aims to maintain global warming below 1.5 °C compared to pre-industrial levels. The global economy must be carbon neutral by the mid 21-century to achieve this goal and avoid the most adverse effects of climate change.[1–2] This agreement demands a societal shift to a low-carbon world, wherein Carbon Capture, Utilization and Storage (CCUS), including Carbon Dioxide Removal (CDR), are part of the plan to mitigate surplus anthropogenic CO_2 in atmosphere.[1] Mineral carbonation (also called carbon mineralization) is a rapid and permanent CCUS method that traps atmospheric CO_2 gas into stable carbonate minerals.[1,3–4]

Carbonate phases formed via mineral carbonation utilize divalent metal cations, typically Ca and Mg, and incorporate dissolved CO_2 from aqueous solutions.[5-17] The formation of Ca-carbonate and hydrated Mg-carbonate minerals have been observed to occur both in laboratory and natural environments at ambient conditions (i.e., room temperature and atmospheric pressure).[5–17] As such, mineral carbonation reactions typically produce the following phases at low temperature: amorphous calcium magnesium carbonates (ACMC), the calcium carbonate polymorphs, calcite, vaterite and aragonite ($CaCO_3$), and the common hydrated magnesium carbonates dypingite [$Mg_5(CO_3)_4(OH)_2 \cdot \sim 5H_2O$], hydromagnesite [$Mg_5(CO_3)_4(OH)_2 \cdot 4H_2O$], lansfordite ($MgCO_3 \cdot 5H_2O$), and nesquehonite ($MgCO_3 \cdot 3H_2O$).[3,5–7,18–23]

Calcite precipitation is a common chemical process at Earth's surface. The precipitation of hydrated Mg-carbonate minerals is also observed in nature, such as during the chemical weathering of mafic and ultramafic rocks (e.g. Wilson et al., 2009)[5] and during biologically-induced mineralization of carbonate sediments in alkaline lakes[22–23]. However, natural silicate weathering and mineral carbonation reactions are slow and occur at a smaller scale, ~1 Gt/year, compared to the more than 36 Gt of CO_2 equivalent greenhouse gases that are emitted to the atmosphere each

year.[24] Mineral carbonation as a CCUS technology aims to enhance the rate and efficiency of carbonation for feedstock materials. In mineral carbonation, the feedstocks are usually referred as reactive Ca- and Mg-rich materials.

Common feedstocks for CCUS include mafic and ultramafic mine tailings[5–9, 25–29], steel slags[29–30], cements[29,31–32], and red mud[29,33-34], which are highly alkaline and contain reactive Mg- and Ca-rich phases such as silicates (e.g. forsterite, Mg_2SiO_4; serpentine minerals, $Mg_3Si_2O_5(OH)_4$; wollastonite, $CaSiO_3$), hydroxides [e.g. brucite, $Mg(OH)_2$; portlandite, $Ca(OH)_2$], and oxides (e.g., periclase, MgO; lime, CaO). Valorizing these materials to sequester atmospheric and industrial CO_2 is economical and has co-benefits such as commercial production of construction materials from carbonated wastes[4,35–36]. In addition to these and other well-explored feedstock materials, Ferrini et al.[37] proposed that hydraulic fracturing flowback and produced water or FPW has potential to supply Mg cations for mineral carbonation. They showed that reaction between synthetic FPW and CO_2 is rapid and efficient at alkaline pH and ambient conditions. Gigalitres of FPW are produced annually during oil and gas recovery from horizontally drilled wells that require hydraulic fracturing in the US and Western Canada.[38] In China, the production of FPW will reach a comparable (i.e. GL) scale by 2030 owing to the surge in hydrocarbon production from the Sichuan Basin.[39] FPW are brines that contain dissolved inorganic species inherited from underground rock formations, recycled hydraulic fracturing fluids, and chemical additives that promote oil and gas recovery. The high salinity of FPW is inherited from the formation water and considered to be originated from evaporated ancient seawater that trapped by intergranular pores.[40] The inorganic components in FPW consist primarily of aqueous Na, Ca, K, Cl, Br, Mg, Sr, B, Li, S, Mn, Pb and Zn, [41–45] of which Ca and Mg (and possible Sr) can be used for mineral carbonation.

The concentrations of these elements in any given sample of FPW depend on the mineralogy of the rock formation and the timing of sampling following well stimulation.[46]

Although FPW has previously been proposed as a source of divalent metals for mineral carbonation[37], the rate and efficiency of FPW carbonation has yet to be tested on real samples under readily scalable, ambient conditions. Importantly, Druckenmiller and Maroto-Valer[47] have reported calcite precipitation from pH-adjusted FPW at 75 °C and 150 °C and pressures of 600 psi and 1500 psi; however, their application was to better understand carbonation under reservoir conditions, which cannot be emulated in an above-ground carbonation plant without substantial energy input and capital expenditure. Prior experiments have shown that synthetic Mg-rich brines and brucite slurries are easily carbonated under alkaline conditions and that supplying concentrated CO_2 gas overcomes the slow rate of atmospheric CO_2 dissolution into these saline waters.[6,7,37]

Mineral carbonation can be summarized into three steps: (1) releasing divalent cations through dissolution of feedstock minerals; (2) dissolution of atmospheric CO_2 gas into solution; and (3) precipitation of carbonate minerals from supersaturated solutions. Dissolution of relatively unreactive Mg- and Ca-bearing minerals, such as silicates, in solid feedstocks is usually the rate-limiting step of mineral carbonation, and it typically requires the addition of chemicals to extract divalent cations.[48] The use of solid feedstocks that contain highly reactive minerals, such as brucite and portlandite, is rapid because the weak acidity of aqueous CO_2 gas is sufficient to extract divalent cations,[6–7] and hence no strong acids are needed. However, highly reactive phases, such as brucite and portlandite, are considerably less abundant on the Earth's surface compared to the less reactive silicate phases, and the demand for CCUS and CDR (Gt/yr) are significantly greater than the CO_2 capture capacity of hydroxide minerals. Direct use of Mg- and Ca-rich FPW as a feedstock for carbonation reactions is advantageous as there is no need to overcome the slow

dissolution of feedstock minerals. As such, an exploration of FPW carbonation can focus on understanding and optimizing steps 2 and 3 (i.e. CO_2 supply and carbonate mineral precipitation) of the mineral carbonation process. Hence, this thesis focuses on promoting the rate and efficiency of mineral carbonation by exploring the conditions that drive CO_2 dissolution and mineral precipitation in FPW.

The idealized net reaction for FPW carbonation can be represented by Eq. 1.

$$M^{2+}\,(aq) + CO_2\,(g) + nH_2O\,(l) \rightarrow MCO_3{\cdot}(n{-}1)H_2O\,(s) + 2H^{+}\,(aq) \qquad \text{(Eq. 1)}$$

In the equation above, M^{2+} is a divalent metal cation, and $MCO_3{\cdot}(n{-}1)H_2O$ represents the precipitated carbonate phase(s). In order to drive the overall reaction towards the right and yield more carbonate minerals, the pH value of solution must be alkaline and CO_2 dissolution must be promoted.

One motivation to embed mineral carbonation in the day-to-day operations of the natural resources, energy and manufacturing industries is the opportunity to recover critical metals that are needed for the sustainable energy transition. Hamilton et al.[49,50] recently identified in laboratory and field-based studies that divalent transition metals (Ni, Mn, Co, and Cu) are released during dissolution of serpentine and brucite and subsequently captured by the precipitated carbonate phases, nesquehonite, hydromagnesite, and pyroaurite [$Mg_6Fe_2(CO_3)(OH)_{16}{\cdot}4H_2O$] as well as in syngenetic Fe-(oxy)hydroxides. Reeder et al.[51] and many previous researchers have observed substitution of ions such as Co^{2+}, Fe^{2+}, Mn^{2+}, and Zn^{2+} for Ca^{2+} in calcite. Increasing the pH value of FPW should favour carbonate precipitation, provided there is a supply of CO_2, while yielding Fe-(oxy)hydroxide precipitates, which form readily from the oxidation of FPW.[52] Formation of Fe-(oxy)hydroxides is known to immobilize a variety of transition metals, including divalent Ni,

Mn, Co, and Cu.[42,54] Mineral carbonation could thus be used to immobilize such heavy metals from FPW.

Moreover, according to Canadian Water Quality Guidelines for the Protection of Aquatic Life[55], B, Cu, Fe, and Zn should be maintained below the 1s–10s ppm level and Cd, Pb, Ni and Mn should be maintained below the ppb level in freshwater. Depending on the composition of the host formation, the concentrations of these elements in FPW may exceed regulatory limits and potentially be toxic to freshwater aquatic life. The water chemistry of FPW reported in previous studies by Folkerts et al.[44] and Zhong et al.[45] indicates that B is present at 10s–100s ppm, which is higher than the guideline benchmark value, and Cu, Mn, and Pb can also have higher concentrations than the recommended limits. Large Sr cations commonly substitute for Ca in carbonate minerals[56–57] and there is a well-known, albeit limited, amount of borate that can be incorporated into the carbonate sites of Ca-carbonate minerals under alkaline conditions.[58–59] Therefore, precipitation of Ca-carbonate minerals from FPW during mineral carbonation has potential to partially immobilize these elements of concern in addition to potentially toxic transition metals (e.g. Cu, Mn, and Pb).

In this thesis, two sets of laboratory experiments were designed and performed to assess the carbonation potential of FPW samples collected from the Western Canadian Sedimentary Basin. Carbonation experiments were conducted across a range of circumneutral to alkaline pH conditions and with gases having two different pCO_2 values (i.e. 0.04% and 10%), which reflect atmospheric CO_2 and the use of combustion flue gas or a dilute CO_2 stream from a Direct Air Capture (DAC) plant. The behaviour of 20 elements of interest (for their value as critical metals and/or as potentially toxic elements) during mineral carbonation of FPW is also examined in this work.

This thesis is the first study to test the rate and efficiency of carbonating real Ca and Mg-rich FPW samples from oil and gas operations. It is the first study of its kind to provide detailed and coupled crystal chemistry, mineralogy, and aqueous geochemistry in such a system. The two sets of experiments in this thesis go on to investigate whether existing and future FPW resources are viable feedstocks for mineral carbonation. The results from the various pH and pCO_2 conditions studied in these experiments offer some insights for further optimization of the carbonation reactions studied herein while recovering valuable metals and/or sequestering toxic ones. Finally, this thesis provides a first assessment of the potential of FPW carbonation to serve as a negative emissions technology (NET) in countries where horizontal drilling is widely applied. It provides the starting point for a discussion of how to viably implement and modify our experimental methods at commercial scale for CDR or CO_2 abatement relevant to the oil and gas sector.

CHAPTER 2: Hydraulic Fracturing Flowback and Produced Water as a Feedstock for Carbon Dioxide Removal via Mineral Carbonation

2.1 Abstract

Hydraulic fracturing flowback and produced waters (FPW) and produced water (PW) are saline brines generated during oil and gas extraction. Here, we investigate the use of FPW as a source of calcium and magnesium for carbon dioxide (CO_2) storage in carbonate minerals. We performed pH titration experiments to precipitate calcium and magnesium carbonates from three FPW samples and one PW sample from Alberta and Saskatchewan, Canada. Depending on the pH (8.5–12), calcite ($CaCO_3$) and brucite [$Mg(OH)_2$], with occasional aragonite ($CaCO_3$) and portlandite [$Ca(OH)_2$] precipitate from FPW within 24 hours of reaction at atmospheric pCO_2 and ~18 °C. We estimate that the carbon capture potential of FPW in the US, Canada and China, is on the scale of 10s–1,000s kt CO_2/year using pH adjustments and relying solely upon passive capture of CO_2 from air. This result can be improved by an order of magnitude if all magnesium and calcium are extracted from FPW by using higher pCO_2 gases, such as flue gases from fossil energy generation or gas streams produced by Direct Air Capture (DAC) plants.

2.2 Introduction

Limiting anthropogenic climate warming to 1.5 °C requires a combination of energy efficiency, deep decarbonization, Carbon Dioxide Removal (CDR) from the atmosphere and carbon storage to reach net zero greenhouse gas emissions (GHG) by 2050.[1] Mineral carbonation is a form of CDR or CCUS (when using industrial CO_2 streams) that reacts alkaline Earth metals, such as Ca and Mg, with gaseous or aqueous CO_2 to precipitate carbonate minerals.[5–17] Typical sources of Ca and Mg for mineral carbonation include alkaline wastes such as mafic and ultramafic rocks and

mine tailings,[5–9,20,25–28]steel slag,[29–30] red mud,[20,33–34] and cement.[20,31–32] These feedstocks typically contain high abundances of Mg- and Ca-silicate minerals, that must first be dissolved to form carbonate minerals,[48] with occasional lower abundances of phases such as Mg- and Ca-hydroxides and oxides which react readily with CO_2 under ambient conditions.[6-7,18,25–27,60,61] Chemical treatments, such as pH-swing methods,[8] are typically required to promote the dissolution of more recalcitrant silicate minerals and to improve conversion to carbonate minerals. As such, dissolution of feedstock minerals tends to be the rate-limiting step when using solid waste as feedstocks.[48] In addition, the surface passivation effects of solid feedstocks, water saturation during reaction, and clogging of the pore spaces due to rapid precipitation hinder the efficiency of mineral carbonation in porous rock media.[62] Those limitations can be circumvented by using an aqueous metal feedstock that already contains Mg and Ca in solution.

Hydraulic fracturing flowback and produced waters (FPW) are fluids produced by the fossil energy industry, and FPW is a mixture of the brines found within a geological formation (> 95 vol.%), hydraulic fracturing fluids, and dissolved organic compounds introduced as additives to facilitate fracturing.[42–44,63–65] Produced waters (PW) are sometimes referred to as fracturing fluids that return to the surface days after the hydraulic fracturing operation and that contain higher concentrations of total dissolved solids (TDS) and lower organic constituents than the earlier returning fluids.[44] Herein, we refer PW as fluids that are brought to the surface by oil and gas operations and that have compositions close to those of subsurface formation brines. Both FPW and PW contain elevated concentrations of Na and Cl, alkaline earth metals (e.g., Ca, Mg, and Sr), and transition metals (e.g., Mn and Zn) compared to freshwater. [42–45,63–65] FPW has been identified to have sub-lethal effects and acute toxicity on aquatic animals, which are attributed to the high salinity and high dissolved organic content of FPW.[44,66–68] The TDS of FPW and PW varies from one geologic

formation to another, and it is also affected by flowback time, with large volumes of low-TDS water generated in the early stage and progressively higher-TDS water produced in the late stage until the solution chemistry equilibrates with in-situ brine;[45,69–70] nonetheless, TDS in FPW/PW is typically hundreds to thousands of times greater than the drinking water limit (500 mg/L)[71] and the limit for agricultural irrigation (100s mg/L)[55]. Therefore, spills[72] and improper disposal of FPW/PW can be potentially detrimental to ecosystems and affect drinking water safety.

Concentrations of Ca and Mg in FPW generated from horizontal wells range from 10s–10,000s ppm and 1s–1000s ppm, respectively.[45,69,72] The concentration of Ca can infrequently reach ~100,000 ppm in FPW[69] and PW[70], which makes FPW/PW attractive resources for mineral carbonation. Druckenmiller and Maroto-Valer[47] demonstrated rapid formation of calcite ($CaCO_3$) from FPW samples under elevated temperature (75 °C and 150 °C) and pressure (600 and 1500 psi) at a pH of ~9 in experiments designed to simulate Carbon Capture and Storage in a saline aquifer. Ferrini et al.[37] proposed that the Mg in saline brines generated by desalination plants and hydraulic fracturing could be used for mineral carbonation under ambient conditions by reaction with high pCO_2 waste gases. They used synthetic, Mg-rich and Ca-poor brines to demonstrate precipitation of the hydrated Mg-carbonate mineral, nesquehonite ($MgCO_3 \cdot 3H_2O$), under high salinity conditions.[37]

In this study, we use hydraulic fracturing flowback and produced water (FPW) and conventional produced water (PW) samples, both collected from the Western Canadian Sedimentary Basin (WCSB). Based on previously published analyses, these samples consist predominantly of formation water, and they contain minor amounts of hydrocarbon additives.[42,44–45,70] The additives in FPW and PW may inhibit mineral precipitation and it is challenging to model aqueous speciation and the saturation indices (SI) of minerals in hypersaline fluids. As such, we adjusted solution pH

to values of 8.5 to 12 (n=8, in pH increments of 0.5) to empirically assess which conditions are most favorable for precipitation of carbonate minerals at atmospheric pCO_2 and ambient temperature. We report detailed geochemical analyses of mineral precipitates and solution chemistry, and we assess the utility of thermodynamic modelling to predict the most suitable conditions for brine carbonation. Our experimental conditions were designed to test conditions for storage sites and treatment plants for FPW and PW that could be built near hydraulic fracturing wells. Based on our results, we provide guidance for design and optimization of industrial-scale carbonation of FPW, PW and other waste brines under ambient conditions.

2.3 Methodology

Three samples of FPW and one sample of PW were used as carbonation feedstocks. The FPW samples, FPW1a, FPW1b and FPW2, were collected from a single horizontally drilled and hydraulically fractured well at 54° 28.9' N, 117° 10.4' W from the Duvernay Formation, Alberta, Canada. The PW sample, described as sample 'U of A 01- 159B' by Rostron et al.[70], was collected in 2001 at 49°17.7' N, 102°50.3' W from the Red River Formation in the Kingsford field, Saskatchewan, Canada. Table A-1 provides a summary of the composition and sources of these brine samples.

Prior to titration experiments, 300 mL of FPW1a and PW samples and 600 mL of FPW1b and FPW2 samples were filtered with Basix™ 0.22 μm PES membranes and stored in polypropylene Nalgene® bottles. Aliquots (30 mL) of each filtered sample were titrated with 1.0 M NaOH to pH values between 8.5 and 12.0 (n=8, in increments of 0.5 pH units; Table A-1) in polypropylene containers using a Thermo Scientific Orion Star T910 Auto-titrator. The electrical conductivity (EC) and pH of the initial brines and brines after reaction for 24 hours were measured. Precipitates

were separated from solutions after reaction and characterized using powder X-ray diffraction (XRD) and scanning electron microscopy (SEM) with energy dispersive X-ray spectrometry (EDX). Quantitative phase analysis with the Rietveld method[73–75] was done using XRD patterns. The elemental composition of separated precipitates, and brines was determined using inductively coupled plasma mass spectrometry (ICP-MS). Geochemical modelling was done using PHREEQC version 3[76] with the phreeqc.dat database, which has been recommended to model reactions in high ionic strength hydraulic fracturing brines.[77] Please refer to the Appendix A for detailed information about experimental procedures and analytical methods.

2.4 Results and Discussion

2.4.1 Titration experiment and evolution of solution chemistry

The Ca concentrations in untreated FPW1a, FPW1b, FPW2 and PW are 11,000 ± 100 ppm, 10,800 ± 290 ppm, 8,180 ± 40 ppm, and 17,300 ± 310 ppm, respectively. The Mg concentrations in FPW1a, FPW1b, FPW2 and PW are 793 ± 46 ppm, 841 ± 15 ppm, 699 ± 26 ppm and 1,920 ± 110 ppm, respectively. The Sr concentrations in untreated FPW1a, FPW1b, FPW2 and PW are 1,050 ± 30 ppm, 952 ±16 ppm, 759 ± 20 ppm, and 595 ± 11 ppm, respectively.

The initial pH values of FPW1a, FPW1b, FPW2 and PW were 5.1, 5.2, 6.1, and 6.0, respectively. Immediately following titration, all pH-modified brines were left to react with atmospheric CO_2 at room temperature (18.0 ± 2.0 °C) for 24 hours. The pH of all brines decreased by 0.5–1.0 units within 24 hours of mineral precipitation and completion of the titration experiments (Figure A-1B). Exceptions were observed for FPW1a and PW at pH 12.0: following titrations, the pH of FPW1a increased from 12.0 to 13.0 whereas that of PW remained constant at pH 12.0, even after 24 h of reaction (Figure A-1B). The dissolved inorganic carbon (DIC) concentrations of all pH-

modified brines after the reaction for 24 hours were less than 10 mg/L (Figure A-1C). No clear trend for DIC versus titration pH is observed for any of the four brines; however, DIC reached a maximum value at pH 8.5 for FPW1a and FPW2. DIC concentrations of FPW1a and FPW2 decreased as the solutions were titrated to higher pH.

In general, the concentrations of both Ca and Mg decreased with increasing of pH endpoint of titration within the pH-modified brines after 24 hours of reaction with atmospheric CO_2 (Figure 2-1). The Ca concentration decreased in all the pH-modified brines compared to the original brines. The Ca concentrations declined between pH 8.5–12.0 (FPW1a), pH 9.0–12.0 (FPW1b), pH 8.5–12.0 (FPW2), and pH 8.5–12.0 (PW). The Ca concentrations in FPW1a and PW, which were of the first-batch titration experiments, decrease dramatically from pH 11.5–12.0 and 11.0–12.0, respectively. At pH 12.0, the Ca concentrations remaining in FPW1a, FPW1b, FPW2, and PW are 28.1%, 84.4%, 72.5% and 41.6% of that in the original brines, respectively. The dramatic decreases of Ca concentrations in FPW1a and PW might be due to the pH change after titration. After titration to pH 12.0 and reacted for 24 hours, the pH of FPW1a and PW increased to pH > 12.0 while the pH of FPW1b and FPW2 decreased.

Mg concentrations in the pH-modified brines after reaction remained at approximately the same level as the original brines when the pH endpoint of titration is 8.5–9.5 (FPW1a), 9.0–10.0 (FPW1b), 8.5–10.0 (FPW2), and 8.5 (PW). The Mg concentrations decrease abruptly at pH endpoint values of 10.0–11.0 (FPW1a), 10.0–11.0 (FPW1b), 10.0–11.0 (FPW2), and 9.5–10.0 (PW). When the pH endpoint value reaches 11.5–12.0 (FPW1a), 12.0 (FPW1b), 12.0 (FPW2), and 11.0–12.0 (PW), the Mg concentrations after reaction with atmospheric CO_2 are below the sample-specific detection limits of ICP-MS measurements, which ranges from 84.5–90.0 ppm (Table A-6). At those pH endpoint values, less than 10.8% (FPW1a), 10.5% (FPW1b), 12.1% (FPW2), and

4.5% (PW) of the Mg remain in the solutions (Table A-5) after reaction. The Mg concentrations that are below the detection limits are plotted only intending to illustrate the trend of Mg concentration as a function of pH endpoint. The concentrations of other elements can be found in Table A-5.

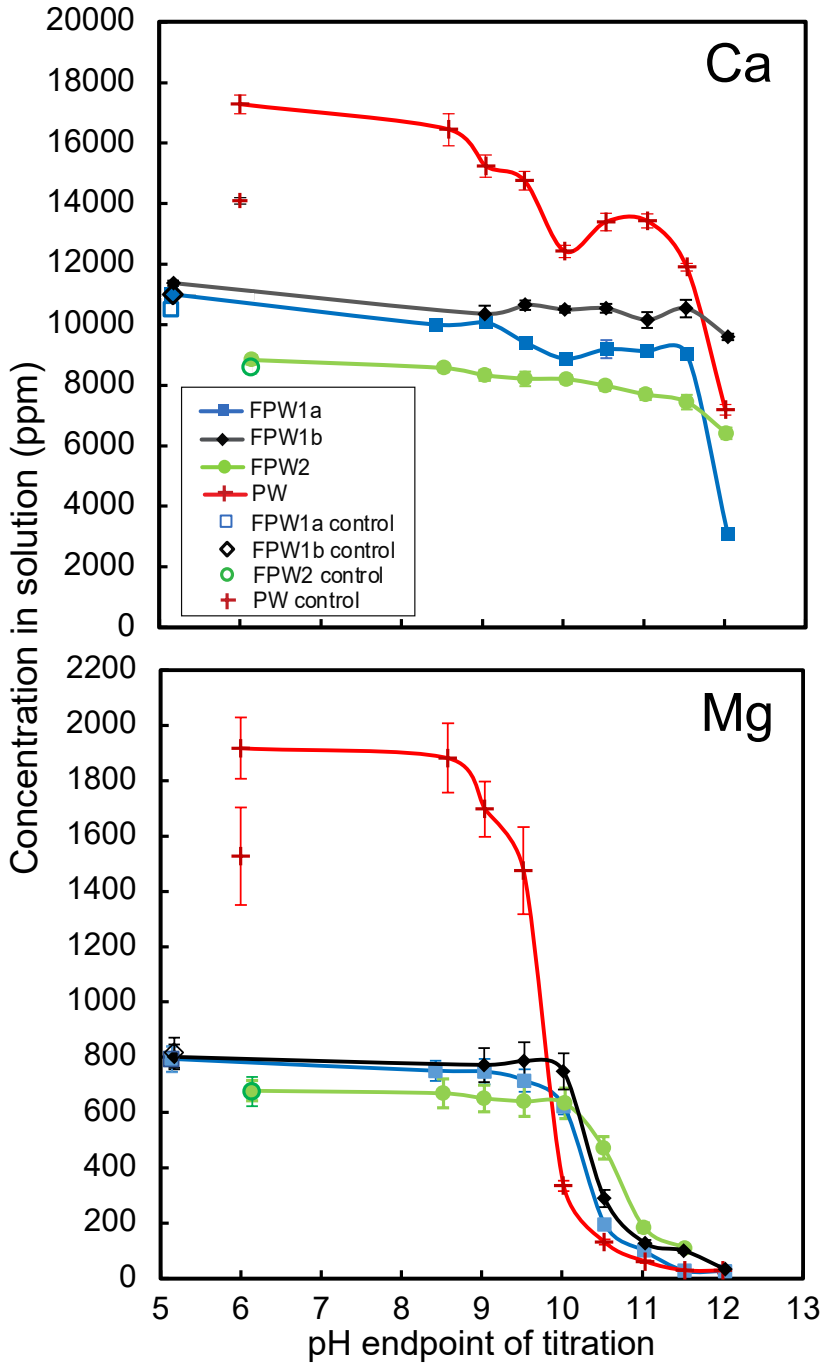

FIGURE 2-1. Ca and Mg concentrations (ICP-MS) of the four brine samples after reaction with atmospheric CO_2 for 24 hours as a function of pH endpoint of titration. The concentrations of pH-modified brines and controls have been corrected for evaporative loss of water. The Ca and Mg

concentrations of FPW1b and FPW2 are average values of the duplicate samples. The analytical errors for Ca and Mg concentrations are given as ± one standard deviation and are the overall analytical error of concentrations from the duplicated samples. Error bars smaller than the labels are not shown.

2.4.2 Mineralogy of precipitates

White, cloudy precipitates were first observed in all four samples at pH 9.0–9.5. Samples of the precipitates were recovered successfully for the following experiments: pH 9.5–12.0 (FPW1a), pH 10.0–12.0 (FPW1b), pH 9.5–12.0 (FPW2) and pH 9.5–12.0 (PW). The precipitates at pH 9.5 from FPW1a and FPW2 were only analyzed with SEM (Table A-7) due to their very limited quantities (<< 10 mg/L). The other precipitates were analyzed with XRD (Figures A-2, A-3) for mineral identification and quantitative phase analysis using the Rietveld method (Table A-7).

The precipitates at 9.5 from FPW1a (Figure A-4, A-5, Table A-7) contain calcite only. At pH 9.5 in FPW2, both calcite and a poorly crystalline Mg-silicate phase can both be detected using XRD (Figure A-5). The precipitates at 9.5 from PW contains aragonite, brucite, and trace amount of calcite. Precipitates at pH 10.0–10.5 contain both calcite and brucite in varying abundances depending on brine chemistry (Table A-7). XRD results show that both calcite and brucite are present in precipitates at pH values of 10.0–12.0 (FPW1a), 10.5–12.0 (FPW1b), 10.5–12.0 (FPW2). The precipitates at pH 9.5–11.5 from PW contain aragonite, brucite, and calcite. At pH 12.0, the precipitates from FPW1a are composed of brucite, calcite, and portlandite [$Ca(OH)_2$], whereas the precipitates from PW are composed of aragonite, brucite, calcite, and portlandite. Portlandite was not observed in precipitates generated from FPW1b or FPW2. Aragonite was only

observed for experiments using PW. Overall, the Rietveld refinement (Table A-7) results show that phase abundance depends on titration pH and brine chemistry.

SEM images (Figures A-4, A-5, A-7–A-9) show aggregates of 1–3 μm subhedral to euhedral calcite rhombohedra, which are commonly coated in plates of brucite and portlandite with the occasional presence of a Mg-silicate phase.

PHREEQC modelling (Figure A-10) with phreeqc.dat was performed to predict SI of brucite, aragonite, calcite, and portlandite (which are the phases were observed to form during experiments) when titrating the original FPW1a to experimented pH. Notably, the difference between the pH value when SI = 0 from the modelling prediction and the pH value of observed mineral precipitation is between a unit of 0–1.5 for the four phases (see SI for more discussion).

2.4.3 Yield of Ca and Mg and CO_2 sequestration in precipitates

The total yield of precipitates (reported in gram of precipitate per litre of brine) increases as a function of pH for all the brine samples (Table A-7). The total yield of precipitates in FPW1a doubles when the titration pH increased from 10.0 to 10.5 and is nearly 9× greater at pH 12.0 than at pH 10.0. The total yield of precipitates increases abruptly when pH changed from 10.0 to 10.5 (FPW1b) and from 10.5 to 11.0 (FPW2). The total yield of precipitates in PW increases by an order of magnitude when pH increases from 9.5 to 10.0 and doubles when pH increases from 11.5 to 12.0. These large increases in the total yield of precipitates correspond to the increasing production of brucite when pH increases from 10.0 to 10.5 (FPW1a, FPW1b) or from 10.5 to 11.0 (FPW2). Differences in total yield and mineralogy can be attributed to the initial Mg and Ca concentrations in the brines. Mg and Ca concentrations are greatest in PW and their concentrations decrease in the order: FPW1a, FPW1b and FPW2 (Table A-5). The total mass yield of precipitates

at a given pH value follows the same trend, from greatest to lowest yield: PW, FPW1a, FPW1b and FPW2. The significant increase in total precipitate yield between pH 11.5 and 12.0 in FPW1a and PW is attributable to the precipitation of portlandite.

The mass of Ca and Mg (the 'yield') and the mass of CO_2 captured in the precipitates can be calculated using Eqs. 1, 2 and 3, respectively:

$$\text{Ca yield} = \sum_{i=1}^{n} \left[\frac{\text{Ca}_i \times phase_i \times M_{yield}}{V_{brine}}\right] \quad (1)$$

$$\text{Mg yield} = \sum_{i=1}^{n} \left[\frac{\text{Mg}_i \times phase_i \times M_{yield}}{V_{brine}}\right] \quad (2)$$

$$\text{CO}_2 \text{ sequestered} = \sum_{i=1}^{n} \left[\frac{\text{CO}_{2i} \times phase_i \times M_{yield}}{V_{brine}}\right] \quad (3)$$

where, Ca_i, Mg_i, and CO_{2_i} are the respective weight percent abundances of Ca, Mg and CO_2 in a given precipitate mineral i using its stoichiometric formula, $phase_i$ is the weight abundance of that precipitate mineral i as estimated using Rietveld refinement, M_{yield} (g) is the total mass of precipitate yielded by an experiment, and V_{brine} (L) is the volume of brine from which the precipitate was obtained. The method we applied here assumes ideal endmember stoichiometry and that all phases are well crystallized. The calculated results for Ca and Mg yield and the mass of CO_2 sequestered are plotted as a function of pH endpoint of titration in Figure A-11 and 2-2, respectively.

Overall, the yields of Ca and Mg in the precipitates increase with increasing pH (Figure A-11). The yield of Ca increases sharply (from ~0.5 g/L to ~2.5 g/L) between pH 11.5 and 12.0 in FPW1a and PW during precipitation of calcite and portlandite. Ca is precipitated between pH 10.0 and 12.0 during formation of calcite in FPW1b and FPW2. The yield of Mg has a sharp increase in the

precipitates between pH 10.0 and 10.5 from PW1a, FPW1b and FPW2 and from pH 9.5–10.0 in PW. Among the studied brines, the yield of Mg shows a strong correlation with the original Mg concentration in the brine samples. PW (1,920 ± 110 ppm) yields more Mg than FPW1a (793 ± 46 ppm), FPW1b (841 ± 15 ppm) and FPW2 (699 ± 26 ppm). In contrast, the yield of Ca in precipitates has no correlation with the initial Ca concentration in the brines. Some caution is called for when using Rietveld refinement results to conduct a mass balance of Ca, Mg, and CO_2 in solid samples because XRD data provide only an indirect description of crystal chemistry[9]. 14 precipitate samples (Table A-8) were digested for ICP-MS analysis to assess the reliability of our XRD results (Figure A-12). Our estimates of Ca and Mg abundance using XRD data are comparable to the results obtained using ICP-MS (Figure A-12) with the caveat that the trend to be slightly overestimated. As a result, results from Eq.3 should provide an equally robust estimate of CO_2 removal from air were obtained at pH 12.

The CO_2 captured readily by precipitates (Figure 2-2A) is attributed to calcite precipitation. The calculation follows Eq. 3 when Ca abundance can be estimated by the Rietveld refinement based on the XRD patterns of obtained precipitates: pH ≥ 10.0 (FPW1a), pH ≥ 10.5 (FPW1b), pH ≥ 10.5 (FPW2), and pH ≥ 9.5 (PW). The minimum CO_2 captured is 0.33 g/L at pH = 10.0 from FPW1a, 0.27 g/L and 0.24 g/L at pH 10.5 from FPW1b, 0.06 g/L and 0.15 g/L at pH 10.5 from FPW2, and 0.06 g/L at pH 9.5 from PW. The values increased over pH and reach 1.46 g/L (FPW1a), 0.36 g/L and 0.31 g/L (FPW1b), 0.45 g/L and 0.38 g/L (FPW2), and 1.76 g/L (PW) at pH 12.0.

If the brucite and portlandite in precipitates are completely converted to nesquehonite ($MgCO_3 \cdot 3H_2O$) and calcite/aragonite, respectively, via exposure to atmospheric CO_2 and higher pCO_2 gas stream, the mass of CO_2 captured by precipitates (Figure 2-2B) has potential to be increased to 0.40 g/L at pH = 10.0 from FPW1a, 1.54 g/L and 1.50 g/L at pH 10.5 from FPW1b,

0.18 g/L and 0.32 g/L at pH 10.5 from FPW2, and 0.32 g/L at pH 9.5 from PW. The values increased over pH and reach 4.38 g/L (FPW1a), 2.33 g/L and 2.52 g/L (FPW1b), 1.76 g/L and 1.62 g/L (FPW2), and 6.98 g/L (PW) at pH = 12.0.

The mass of CO_2 that can be potentially sequestered when all Ca and Mg removed from solution is respectively carbonated to nesquehonite and calcite/aragonite (Figure 2-2C) are calculated from the ICP-MS results of the Ca and Mg concentrations in solutions (Figure 2-1). The Ca and Mg removed from solutions are calculated following $\Delta[M]_{\text{pH endpoint of titration}} = [M]_o - [M]_{\text{pH endpoint of titration}}$, where M represents Ca or Mg concentrations and $[M]_o$ is the concentration of Ca or Mg in original FPW/PW samples. Then, the mass of CO_2 sequestration potential per liter of FPW/PW is converted from the mass of Ca or Mg removed per liter of FPW/PW stoichiometrically based on the chemical formula of calcite/aragonite and nesquehonite, respectively. Accordingly, the CO_2 sequestration potential at pH 8.5 are 1.19 g CO_2/L (FPW1a), 0.309 g CO_2/L (FPW2), 0.984 g CO_2/L (PW), respectively, and the value at pH 9.0 by FPW1b is 1.17 g CO_2/L if all the Ca and Mg removed from solutions are converted to carbonates. The CO_2 sequestration potential is 2.65 g CO_2/L at pH = 10.0 from FPW1a, on average of 1.85 g CO_2/L at pH 10.5 from FPW1b, on average of 1.31 g CO_2/L at pH 10.5 from FPW2, and 3.57 g CO_2/L at pH 9.5 from PW. The values increased over pH and reach 10.1 g CO_2/L (FPW1a), on average of 3.34 g CO_2/L (FPW1b), on average of 3.81 g CO_2/L (FPW2), and 14.5 g CO_2/L (PW) at pH = 12.0. When all the Ca and Mg in the four brines are carbonated, the maximum CO_2 sequestrated can reach 13.5 g CO_2/L (FPW1a), 12.2 g CO_2/L (FPW1b), 10.9 g CO_2/L (FPW2), and 22.5 g CO_2/L (PW) (horizontal lines in Figure 2-2C).

Generally, the Ca extracted from the solution given by ICP-MS analysis of the solution is significantly higher than that given by XRD analysis of the precipitates, and Mg extracted from the solution given by ICP-MS aligns with that given by XRD analysis of the precipitates. The

actual CO_2 captured (Figure 2-2A) and CO_2 sequestration potential by precipitates (Figure 2-2B) based on XRD patterns of the obtained precipitates represents the minimum values as separating the solid and the solution through centrifugation is likely to cause partially loss of Ca-carbonate or hydroxide nanoparticles. The CO_2 sequestration potential based on ICP-MS results varies from 1 to 11-fold of the values estimated based on XRD analysis of precipitates at pH 10.0 (FPW1a), 10.5 (FPW1b and FPW2), and 9.5 (PW), which is likely due to the variation of sample loss during solid collection. At higher pH, the CO_2 sequestration potential based on ICP-MS analysis is generally close to 2-fold of the values estimated based on XRD analysis.

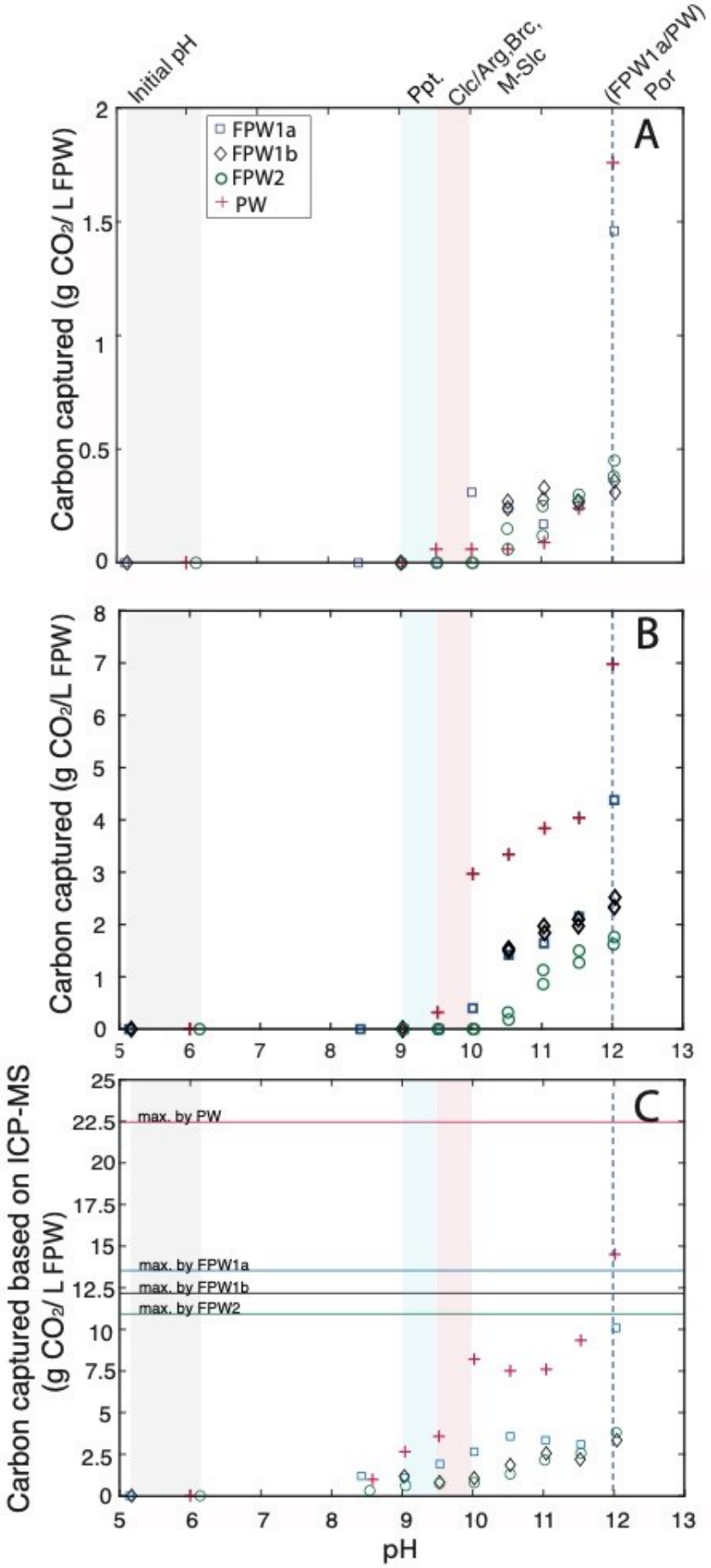
Initial pH
Ppt.
Clc/Arg,Brc,
M-Slc
(FPW1a/PW)
Por
FPW1a
FPW1b
FPW2
PW
A
B
C
Carbon captured (g CO2/ L FPW)
Carbon captured (g CO2/L FPW)
Carbon captured based on ICP-MS
(g CO2/ L FPW)
max. by PW
max. by FPW1a
max. by FPW1b
max. by FPW2
pH

FIGURE 2-2. (A) Observed mass of CO_2 captured during titration experiments using XRD data. (B) Mass of CO_2 that can be sequestered when remaining portlandite and brucite are completely carbonated to calcite/aragonite and nesquehonite, respectively, via exposure to atmospheric CO_2 or a higher pCO_2 gas stream (using XRD data). (C) Mass of CO_2 that can be sequestered when all Ca and Mg removed from solution is carbonated to nesquehonite and calcite/aragonite, respectively, using ICP-MS data from solutions from Figure 2-1. Blue, black, green, and red lines plot the maximum CO_2 sequestration potential by FPW1a, FPW1b, and FPW2, and PW, respectively, when all the Mg and Ca in solutions are carbonated.

2.4.4 CO_2 supply limits carbonation rate of brines

Our experimental results show that brines precipitated Mg-hydroxide (brucite) in favor of hydrated Mg-carbonate minerals at alkaline pH. We conducted thermodynamic modelling using PHREEQC version 3 (Figure A-10) using the solution chemistry of FPW1a and between pH 5.0–13.0. The starting DIC value used for modelling was measured from untreated FPW1a in contact with atmospheric pCO_2 at room temperature (18 ± 2 °C). The common hydrated Mg-carbonate minerals produced during mineral carbonation [dypingite, $Mg_5CO_4(OH)_2 \cdot \sim 5H_2O$; hydromagnesite, $Mg_5(CO_3)_4(OH)_2 \cdot 4H_2O$; and nesquehonite, $MgCO_3 \cdot 3H_2O$] are undersaturated in FPW1a at pH 5.0–13.0 owing to the low concentration of DIC (Figure A-1C) in the initial solution and after titration. Although magnesite ($MgCO_3$) and disordered dolomite [$CaMg(CO_3)_2$] reach supersaturation, we did not observe those phases because their nucleation is kinetically inhibited at room temperature unless catalyzed using carboxyl functional groups on abiological substrates or microbial cell walls[78-80].

Both aragonite and calcite/aragonite are supersaturated in FPW1a at elevated pH, which is consistent with the observed mineralogy of the precipitates. However, aragonite was only observed in precipitates from PW (Table A-7). The lack of aragonite in FPW1a and other brine precipitates may be due to their undersaturation (Figure A-10) and original Mg/Ca ratio[81] (Table A-5) when minerals precipitated, which favors calcite precipitation. Formation of portlandite [$Ca(OH)_2$] is predicted from geochemical modelling (Figure A-10) as observed at pH ~12.0 for FPW1a and PW.

The nanoscale morphology of hexagonal platelets and rosettes of both brucite (e.g., Figures A-4C, A-4D and A-9A) and portlandite crystals (e.g., Figure A-9C) reflects rapid precipitation, as do the broad peaks observed for these phases in XRD patterns. Although this morphology should provide a large reactive surface for carbonation reactions,[31,62] our results show that pH > 10.5 (FPW1a, FPW1b and FPW2) and pH > 9.5 (PW) precipitates contain more hydroxide phases than carbonate phases (Table A-7). This indicates that mineral precipitation outpaces the dissolution of atmospheric CO_2 into the brines. Carbon limitation in this system can likely be overcome by increasing DIC concentration using a concentrated supply of high pCO_2 gas.[6–7] We therefore propose that carbonation of brines using higher pCO_2 gas streams should be explored. The greatest yield of Ca and Mg, and the greatest CO_2 sequestration, are likely to be achieved at one of two pH intervals if the pH condition is maintained: (1) within the pH range of 9.5–10.0 (FPW1a, FPW1b, and FPW2), where Ca-carbonate minerals (aragonite or calcite) are most favoured to form over portlandite and brucite or (2) at pH >10.5 (FPW1a, FPW1b, FPW2, and PW), to maximize precipitation of reactive, nanocrystalline hydroxide minerals (brucite[6-7,61] and/or portlandite[18]) for further carbonation. The latter energy strategy has potential to utilize the full carbonating potential of the brine by carbonating Mg as well as Ca; however, a greater amount of base is needed to achieve this outcome. It should be noted that the exact pH ranges for these reactions will depend

on the solution chemistry of a specific brine. The expense and embodied carbon involved in using NaOH, or another base as well as CaO, to achieve the desired pH will also need to be considered as part of a Life Cycle Assessment (LCA) and Techno-Economic Assessment (TEA). If all the precipitated hydroxides can be carbonated with the supply of high pCO_2 gas (Figure A-2B), the carbon capture capacity can be increased by at least 4 times at pH > 10.5 than it is under atmospheric pCO_2 (Figure A-2A) based on the XRD results.

2.4.5 Prospects for implementation of brine carbonation in the oil and gas sector

Oil and gas operations including extraction, processing, and transportation, which do not involve utilization of the fuel, were indirectly responsible for ~5.2 Gt CO_2 equivalent (CO_2e) emissions in 2018 globally.[82] The Canadian oil and gas sector was indirectly responsible for 191.4 Mt CO_2e emissions in 2019, and the transport sector contributed another 185.8 Mt CO_2, representing 52% of the 730 Mt CO_2 emitted nationally.[83] Traditional Carbon Capture and Storage (CCS) associated with enhanced oil and gas recovery currently only stores ~260 Mt CO_2e worldwide every year.[84] With >36 Gt CO_2e emitted per year globally,[85] achieving net zero GHG emissions by 2050 will likely require capturing CO_2 directly from air as well as from large point-sources of industrial CO_2.[86–89]

Our results show that pH adjustments can be used to produce Ca-carbonate minerals and highly reactive brucite and portlandite for CO_2 removal from air. The global scale of FPW production suggests these brines may be available at sufficient scale to be useful feedstocks for mineral carbonation. Kondash et al. (2017)[90] estimated that each hydraulic fracturing well produces a median volume of 1.7 to 14.3 ML/year of water during its first 5–10 years of operation. In Western Canada alone, there are more than 10,000 hydraulically fractured wells that have been drilled

within the past 10 years.[91–93] Zolfaghari et al.[94] estimated that 66.8 million m^3 of FPW were produced in Canada during 2020 from the 16,068 registered hydraulic fracturing wells that were drilled after 1990 in the WCSB. Unconventional oil and gas production in the United States is estimated to have produced 803 GL of hydraulic fracturing fluids within the past 6 to 10 years.[95] More recent estimates by Zolfaghari et al. reveal that hydraulically fractured wells in the US generated 356.4 GL of brine in 2019 alone.[94] In China, it is estimated that a total of 2.16 GL of FPW were generated from the Fuling shale gas field in the Sichuan Basin between 2014–2015.[96] With the recent surge in shale gas exploration in China,[96–97] it is predicted that the gas fields in the Sichuan Basin will yield 20–55 GL/year of FPW from 2020 to 2030[98] and that production will increase as more gas fields are exploited.

Here we provide a first, high-level estimate of the capacity for hydraulic fracturing brine carbonation for the USA, Canada and China based on following data from our experiments: (1) observed precipitated carbonates (Figure 2-2A), (2) precipitated hydroxides when carbonated (Figure 2-2B), and (3) Ca and Mg removal in brines (Figure 2-2C). The source of annual FPW production data and results of our calculations are summarized in Tables A-9 and A-10, respectively. If the average solution chemistry of our four brine samples can represent the average solution chemistry of the brines produced in Canada, US, and China, adjusting pH of the brines to 10.5–12.0 and reacting them for 1 day with ambient CO_2 in air, with the total FPW production can readily capture 4.70–31.7 kT (Canada, 2020), 52.7–355 kT (US, 2019), and 0.319–2.15 kT (China, 2014–2015) of CO_2 based on our XRD results of the obtained precipitates (Figure 2-2A) with the variation depends on the pH endpoint of titration. If a comparable amount of hydroxide minerals observed in our experiments can be fully converted to carbonate minerals (Figure 2-2B), the CO_2 capture capacity can be enhanced to 59.3–123 kT (WCSB, Canada; 2020), 665–1,380 kT (US,

2019) and 4.03–8.36 kT (Fuling shale, China; 2013–2014). Moreover, if all the Ca and Mg removed from the solutions provided by the ICP-MS results can be completely converted to carbonates (Figure 2-2C), the CO_2 capture capacity can reach 117–252 kT (WCSB, Canada; 2020), 1,310–2,830 kT (US, 2019) and 7.94–17.1 kT (Fuling shale, China; 2013–2014).

Zolfaghari et al.[94] showed that both Ca and Mg concentrations in FPW from Canada ranges between 500–70,000 mg/L. The estimated average concentration of Ca is 2,650 mg/L and that of Mg is 2,100 mg/L based on the solution chemistry of 16,068 hydraulic fracturing wells. Assuming similar average Ca and Mg concentrations, we estimated 151 kT (WCSB, Canada; 2020), 1.69 MT (US, 2019) and 10.3 kT (Fuling shale, China; 2013–2014) CO_2 can be captured with full conversion of Ca and Mg in brines to calcite/aragonite and nesquehonite, respectively. Accordingly, the estimated CO_2 captured in Canada is equivalent to ~0.079% of the embodied carbon (~190 Mt CO_2e)[83] from oil and gas industry in Canada and will save 7.55 M of CAD per year given the price[99] of 50 CAD per tonne of CO_2 in 2022. The produced carbonate minerals can be possibly used as construction materials to further offset the operation cost of this technique.The average Ca and Mg concentrations in China and the US differ from the estimated Canadian average value, hence, a more comprehensive estimation of the CO_2 capture is needed to be performed in the future study.

Both direct air capture (DAC) and Ca and Mg looping technology are forms of CDR technology. DAC sequesters CO_2 directly from the ambient air,[88–90] which is via sparging air through alkaline solutions or solid sorbent filters.[100] It has great potential to offset CO_2 but the current techniques require enormous areas of land and it is cost-inefficient. Ca and Mg looping methods would reuse mineral feedstocks after reacting with CO_2 in air by calcining the resultant Ca- and Mg-carbonates repeatedly.[87–88] Several recent studies have proposed that Ca and Mg looping methods could be

used to scale-up the carbon capture capacity of limited natural or industrial feedstocks for mineral carbonation,[87–89] such that the technology might be scaled to the Gt CO_2 per year level. It is possible that this approach might be used to capture an infinite amount of CO_2 from air at ambient temperature, pressure and pCO_2.[87–88]

The mineral carbonation using FPW as feedstock solutions described in our study can be deployed with industrial waste gas as the CO_2 source or via DAC with CO_2 sourced from the ambient air (Figure 2-3). The pH-modified FPW serves as an aqueous sorbent in such systems and the precipitated Ca- and Mg- hydroxides or carbonates could be combined with Ca[101–103] and Mg[87–88,104–107] looping technologies for further extraction of concentrated CO_2. The purified CO_2 from calcination then either could be transported using the growing network of CO_2 pipelines (e.g., the Alberta Carbon Trunk Line in the WCSB) for injection into geologic formations dedicated to storage or for utilization in the manufacture of value-added products.[87–88] Finally, the MgO and CaO calcination products can be reused to scavenge more CO_2 from air. Unlike most of the previously developed looping systems[102,105–107], in which carbon mineralization happens at high temperature and pressure conditions, both the initial carbonate mineral precipitation and reuse of MgO and CaO calcination products take place at the ambient conditions as proposed by Kelemen et al.[87] and McQueen et al.[88]. Using FPW as a source of Mg and Ca for looping also negates the need to calcine magnesite, dolomite or limestone as feedstocks for CDR, maintaining permanent storage of the CO_2 in these mineral deposits within the rock record. Future directions on maximizing the efficiency of using FPW for CRD are summarized in Appendix A Section A4.

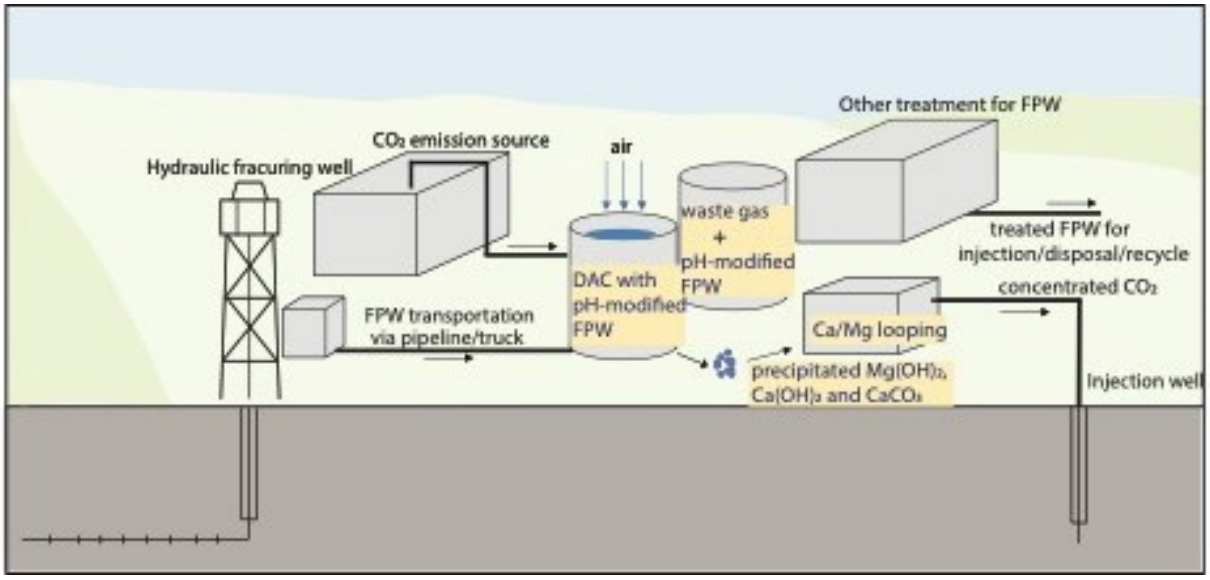

FIGURE 2-3. Schematic illustration of FPW carbonation via CDR coupled to Ca/Mg looping plus injection into a sedimentary formation. The design of the installation is based on publicly accessible information on hydraulic fracturing operations[93], wastewater treatment plants[108], and looping methods[87–88].

CHAPTER 3: Accelerating Mineral Carbonation with Hydraulic Fracturing Flowback and Produced Water Using Elevated pCO_2 Gas

3.1 Abstract

Mineral carbonation removes anthropogenic carbon dioxide (CO_2) from the atmosphere through precipitation of carbonate minerals. Hydraulic fracturing flowback and produced water (FPW) is Ca- and Mg-rich wastewater produced by the petroleum industry that has potential to be used to sequester CO_2 in minerals. Here, we describe the rate and efficiency of carbon mineralization achieved by sparging 10% CO_2/90% N_2 gas into pH-adjusted FPW (pH = 10.5) from the Duvernay Formation, Western Canadian Sedimentary Basin. We report data for water chemistry, mineralogy, and gas composition for the duration of each experiment. Our results indicate that calcite ($CaCO_3$) precipitated at the expense brucite [$Mg(OH)_2$] dissolution following CO_2 injection. As such no Mg-carbonate precipitates were formed. The carbonation reaction reached steady state within 1 hour and 14.2% of the Ca in the FPW was extracted to form calcite. Precipitated calcite sequestered 1.56 ± 0.33 g CO_2 per liter of FPW; however, carbonating all the Ca and Mg in the FPW offers a greater CO_2 sequestration potential of 12.5 ± 0.3 gram of CO_2 per liter of water sample (g CO_2/L). Our stable carbon isotope results, DIC measurements and PHREEQC models indicate that CO_2 mineralization can be maximized by maintaining solution at pH ≥ 10 during CO_2 sparging.

3.2 Introduction

Between 1 to 15 $GtCO_2$ per year must be removed from the atmosphere beginning in 2018 to limit global warming to 1.5 °C before 2050.[1] Mineral carbonation is a nature-inspired Carbon Dioxide Removal (CDR) process that converts atmospheric CO_2 into carbonate minerals by dissolving and reacting Mg- and Ca- silicate and hydroxide minerals[10,109–110] with dissolved inorganic carbon

(DIC). It can also be used as a Carbon Capture Utilization and Storage (CCUS) technology to sequester CO_2 from industrial point sources. *Ex situ* mineralization of CO_2 includes carbonation of alkaline industrial and mine wastes at Earth's surface,[5,25,27–29,34,50,111] whereas *in situ* mineralization is achieved by injecting CO_2 gas into basalt, serpentinite or peridotite.[112–115] At full scale, mineral carbonation has the potential to provide negative emissions on the scale of several Gt CO_2/yr.[29,116] Pilot projects for *in situ* mineral carbonation include the Carbfix and Carbfix2 projects in Iceland,[117–121] the Nagaoko project in Japan,[121] and the Wallula project in the United States,[123–125] which have tested or commercialized subsurface mineralization in basalt. DeBeers Project CarbonVault[126–129] is piloting *ex situ* carbonation of processed kimberlite from diamond mines. Mineral carbonation and enhanced weathering start-up companies such as Project Vesta,[130] Heirloom[131] and 44.01[132] are expected to begin field trials in the coming years as well.

Most mineral carbonation studies have sourced Mg and Ca from rocks or mineral wastes owing to their high concentration in these materials (e.g., 29.9 wt.% Mg in dunite, 24.1 wt.% Mg in serpentinite, 3.7 wt.% Mg and 6.7 wt.% Ca in basalt; Lackner et al.[10]). However, only a fraction of the Mg and Ca in rocks is contained in minerals that are highly reactive with CO_2 and able to contribute to fast carbonation reactions. For instance, the fast reactivity of serpentinite to CO_2 depends primarily on the abundance of the highly reactive mineral, brucite [$Mg(OH)_2$]. [6,25,111] A serpentinite that contains 5 wt.% brucite will not have much more *highly reactive* Mg than the ~2.9 wt.% contained in brucite (assuming ideal stoichiometry), which is on the order of 10% of the total Mg in this rock type. Waste brines, such as those produced by the oil and gas sector, have received less attention as feedstocks for mineral carbonation. This is, in part, because they have a lower overall concentration of Mg and Ca than rocks and waste minerals. However, they contain

comparable concentrations of highly reactive Mg and Ca, and these elements are already in solution.

Approximately 420 Mt/year of ultramafic mine tailings are currently produced each year.[3] Renforth (2019)[29] estimated that as much as 3.5 Gt/year of ultramafic mine tailings may be produced by 2100 owing to demand for critical metals such as nickel, cobalt, and platinum group elements. By comparison, hydraulic fracturing (HF) generated an estimated 66.8 million m^3/year (~66.8 Mt/year) and 356.4 million m^3/year (~356.4 Mt/year) of FPW in Canada during 2020 and in US during 2019, respectively.[38] Thus, the scale of FPW production alone is comparable to that of ultramafic mine tailings. Considering the much larger amount of waste brines generated by non-HF wells, total brine production in North America alone will be even higher than the above estimation using only FPW. For example, accounting for the well drilled after 1990 in North America, conventional wells in 2020 from US produced additional 892.7 million m^3 and from Canada produced additional 171.3 million m^3.[38] Therefore, waste brines offer considerable potential for mineral carbonation.

Hydraulic fracturing flowback and produced water (FPW) is brine from geological formations, which mixes with recycled water from previous fracturing and with chemical additives that enhance petroleum recovery. [42,43,64,65] FPW has previously been identified as a potential feedstock solution for mineral carbonation owing to its elevated Ca and Mg content.[37,47] Ferrini et al.[37] demonstrated that nesquehonite ($MgCO_3 \cdot 3H_2O$) is produced from synthetic waste brines via injection of CO_2 gas, and they suggested this method can be applied to FPW or waste brines from desalination plants at ambient conditions. Druckenmiller and Maroto-Valer[47] studied calcite ($CaCO_3$) precipitation from FPW under high temperature and pressure conditions as an analog to mineral carbonation in saline aquifers. In a previous study (Chapter 2; Zhu et al., in preparation)[133],

we demonstrated that brucite [$Mg(OH)_2$], a highly reactive phase that can easily be carbonated to hydrated Mg- carbonates[6,7,60], and calcite ($CaCO_3$) form by reaction of atmospheric CO_2 and pH-modified FPW at room temperature (~20 °C).

In this study, we describe the results of laboratory carbonation experiments using FPW and 10% CO_2 (i.e., simulated flue gas[134]). This work builds on our previous study of FPW carbonation using CO_2 capture from ambient air (Chapter 2; Zhu et al, in preparation[133]). The compositions of solids, solutions and gases are monitored throughout the experiments to understand the efficiency of FPW carbonation. Our results provide information on how the carbonation of FPW and other highly saline solutions, such as seawater or mine leachates, might be optimized using high pCO_2 gas streams such as flue gas or purified CO_2 from Direct Air Capture plants (e.g., McQueen et al., 2021)[135].

3.3 Materials and Methods

Solutions of 1M NaOH were made from Sigma-Aldrich® sodium hydroxide pellets 1 day prior to the carbonation experiments to limit uptake of atmospheric CO_2. The FPW sample used in this study was collected 324 hours after well stimulation from the Duvernay Formation (Sample FPW1, described in detail in Chapter 2; Zhu et al., in preparation)[133]. It was filtered using 0.22 μm syringe filters to remove suspended particles and microbes. Prior to each experiment, approximately 1.2 L of filtered FPW were titrated to pH 10.5, sealed with parafilm and allowed to equilibrate for about 40 minutes. Cloudy, white precipitates were observed immediately after NaOH was added to the FPW.

A custom gas mix of 10% CO_2 in N_2 was supplied into a 2 L Nalgene® polypropylene vacuum flask containing 1.2 L of FPW. Experiments were conducted in a fume hood using a setup (Fig.

S1) that was modified from that of Harrison et al. (2012)[7] and Wilson et al. (2010)[6]. A Cole-Parmer® flow meter was used to supply the gas into FPW through a Chemglass Life Sciences® gas dispersion tube with medium frits to decrease the size and increase the amount of gas bubbles. The CO_2 concentration of the outflow was analyzed using a CO2METER K33 ICB 10% CO_2 sensor (accuracy of ±100 ppm). The experimental apparatus was sealed, except during sampling, with only 10% CO_2 in N_2 gas flowing in from the gas sparger and gas flowing out to the CO_2 meter through the side-arm of the vacuum flask.

The 10% CO_2/90% N_2 (by molar) gas mix was supplied to pH-modified FPW at a constant flow rate of 250 mL/min for 27.5 hours in two (duplicate) carbonation experiments, which we refer to hereafter as Experiments CA and CB. Experiment CA was conducted under ambient laboratory conditions at a temperature between 16.5–17.7 °C and a relative humidity of 16.0%. Experiment CB was conducted 1 week later at a temperature between 17.6–18.7 °C and a relative humidity between 21.0–27.9%. Samples were taken at 23 time points in each of the two experiments: samples (n =1) were taken right after pH titration of the FPW; in the first 0.5 h after supplying CO_2 gas, samples were taken every 5 minutes (n = 7); in the second 0.5 h after supplying CO_2 gas, samples were taken every 10 minutes (n = 3); from 1.5 h to 5.5 h, samples were taken every 30 minutes (n = 8); and thereafter samples (n = 4) were taken at 8, 22, 27, and 27.5 hours. Approximately 7 mL of solution were collected at each sampling point. Prior to sampling, the solutions and suspended precipitates were mixed well by vigorous shaking. The mass of the experimental apparatus was recorded before and after collection of each sample to monitor evaporative mass loss and CO_2 uptake into precipitates. The mass of each sample of solution and suspended precipitate was also recorded, and the samples were then centrifuged at 7800 rpm for 5 minutes to separate liquid from solids with an Eppendorf 5430 Centrifuge. The separated solids

were washed 3 times with MilliQ water (>18.2 MΩ·cm) to remove halite crystals formed by evaporation of residual FPW and then centrifuged at 7800 rpm for 5 minutes after each wash to remove liquid.

The washed precipitates were then dried for 1 week in a desiccator containing Drierite^{TM} at room temperature, weighed, and split into subsamples for powder X-ray diffraction (XRD), scanning electron microscopy (SEM), inductively coupled plasma mass spectrometry (ICP-MS), and stable carbon and oxygen isotope analyses. The separated solutions were filtered with 0.22 μm membranes and split into subsamples for analysis. Subsamples for stable isotope analysis and dissolved inorganic carbon (DIC) analysis were stored in ~2.5 mL glass vials with zero headspace, sealed with parafilm to avoid further reaction with air, and stored at 4 °C. The pH and conductivity of the remaining solutions were measured immediately with a Thermo Scientific® Orion Star A215 pH/Conductivity meter. Alkalinity values of the solutions from Experiment CA were analyzed immediately while those of solutions from Experiment CB were analyzed within 24 hours of sampling. The remaining solutions were stored at 4 °C for (ICP-MS) analysis. Detailed analytical methods are included in the Appendix B of this thesis.

3.4 Results

3.4.1 Evolution of solution chemistry during carbonation experiments

The pH values of the initial FPW used in Experiments CA and CB were 6.0 ± 0.1 and 5.7 ± 0.1, respectively. Experiments CA and CB had initial conductivity values of 202.0 mS/cm and 202.3 mS/cm, respectively. The initial concentration of dissolved inorganic carbon (DIC) was measured with a CO_2 coulometer to be 1.82 mg C/L and 0.64 mg C/L for Experiments CA and CB, respectively. The elemental concentrations of aqueous species in the initial FPW were determined

using ICP-MS (Table B-6). Na and Cl are the most abundant dissolved elements. Na concentrations are 56,900 ± 1,960 ppm (CA) and 56,900 ± 1,950 ppm (CB), whereas the Cl concentration is 124,000 ppm in both Experiments CA and CB. Ca is the third most concentrated element with 10,200 ± 100 (CA) and 9,930 ± 180 (CB) ppm. The concentration of Mg is 791 ± 25 ppm and 780 ± 28 ppm in Experiments CA and CB, respectively. Sr is also present at high abundance: 934.3 ± 25.4 ppm and 927.0 ± 24.0 ppm in Experiments CA and CB, respectively. Si concentrations in Experiments CA and CB are 12.6 ± 0.4 and 11.5 ± 0.4 ppm, respectively. Small differences in the elemental composition of the brine used in Experiments CA and CB can be explained by analytical error. The initial concentrations of other elements in the FPW are listed in Table B-6.

The pH the FPW used in the two duplicate experiments (CA and CB) was titrated to a value of 10.5 in order to supply alkalinity for further carbonation. This pH value was selected because it allows for brucite precipitation while using a minimum amount of NaOH (after Zhu et al., in preparation)[42]. A total of 94.4 mL and 93.9 mL of 1 M NaOH solution was added to 1.2 L of FPW in each of Experiments CA and CB, respectively. The pH-modified solutions were then sealed within plastic sidearm flasks to restrict interaction with the laboratory atmosphere for approximately 40 minutes while installing the experimental apparatus. The conductivity of solution in both experiments was generally stable between 190–210 mS/cm for their entire duration (Figure B-2A). The pH of both experiments at t = 0 min (right before supplying 10% CO_2) had dropped to a value of 10.4 (Figure 2-1), which is attributed to the precipitation of solid phase(s) following pH titration. After CO_2 gas was supplied to the pH-adjusted FPW, the pH value of solution decreased between t = 0–10 min from a value of 10.4 (CA and CB) to either 9.7 (CA) or 9.9 (CB). The pH changed more slowly between t = 10–15 min, declining from 9.9 to 9.7 in

Experiment CA and increasing slightly from 9.7 to 9.8 in Experiment CB. pH values then decreased dramatically between t = 15–40 min and plateaued at a value of approximately 6.4 (CA) and 6.3 (CB) from t = 90 min until the experiments were stopped at 1650 min (27.5 hours).

The DIC samples of brines were collected immediately at each sampling time point during the experiments and were sealed with parafilm before the measurements at Trent University a week after. The concentrations of DIC in the original solutions were 1.82 mg C/L (CA) and 0.64 mg C/L (CB) (Figure 3-1B, Tables B-7 and B-8). DIC concentrations in both experiments remained relatively unchanged between t = 0–40 min. At t = 40 min, the concentration of DIC increased to 36.9 mg C/L (CA) and 35.8 mg C/L (CB). The DIC concentration of Experiment CA increased progressively to a maximum value of 69.0 mg C/L at t = 90 min and that of Experiment CB reached a maximum of 63.9 mg C/L at t = 240 min. DIC values decreased thereafter and plateaued at 28.9 mg C/L (CA) and 55.7 mg C/L (CB).

The alkalinity (Figure B-2B) of the solutions was measured as $[HCO_3^-] + 2[CO_3^{2-}]$ after each sampling. When pH = 6.0–6.4, the alkalinity is approximately equal to $[HCO_3^-]$. Alkalinity values (reported as mg C/L) follow a similar trend to those obtained for the concentration of DIC, but are typically greater in magnitude (Figure 3-1). In Experiments CA and CB, the alkalinity of the initial brine before titration was 11.9 mg C/L and 10.4 mg C/L, respectively. In Experiment CA, the alkalinity increased rapidly following injection of CO_2 gas and then decreased from 252.8 mg C/L to 28.8 mg C/L from t = 0–30 min. Thereafter, the alkalinity of Experiment CA increased to an average value of 73.7 ± 15.6 mg C/L between t = 50–1650 min. In Experiment CB, the alkalinity declined following initial injection of CO_2 from 251.8 mg C/L to 37.4 mg C/L, and then maintained an average value of 24.4 ± 6.7 mg C/L between t = 40–1650 min. The difference in the steady-state alkalinity values for Experiments CA and CB are likely attributable to CO_2 degassing and the

amount of time that had passed before alkalinity was measured after sampling: measurements were performed approximately 5 minutes after sampling for Experiment CA, whereas alkalinity was measured ~27.5 hours after sampling for Experiment CB.

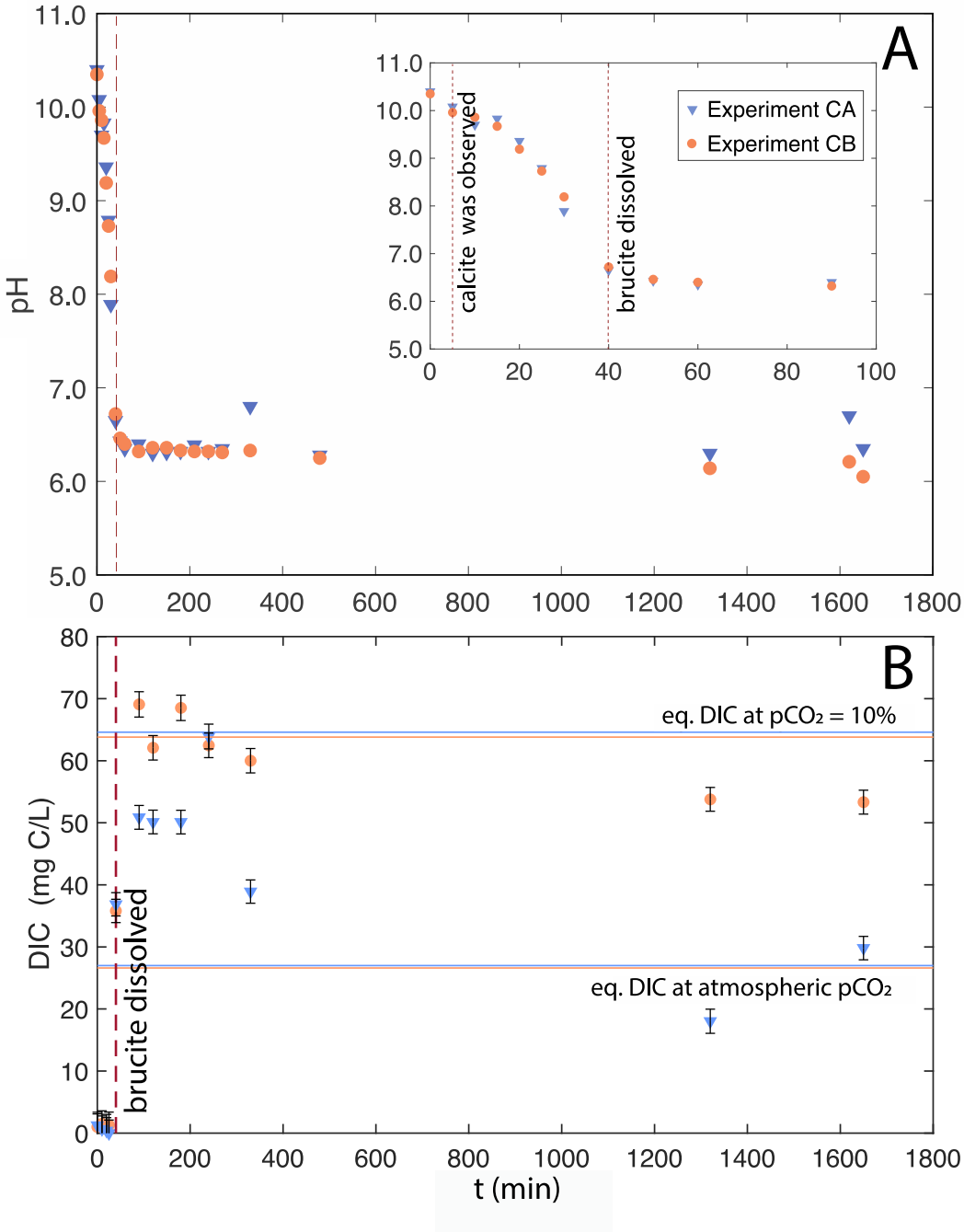

FIGURE 3-1. Time dependence of (A) solution pH and (B) concentration of DIC. The inset in (A) shows the region of the pH–*t* plot bounded by the dashed vertical line through $t = 100$ min.

Plots of ICP-MS results for Ca and Mg concentrations over time are given in Figure 3-2. Considering the dilution caused by NaOH addition before carbonation experiments, the Ca concentrations of the original, diluted FPW samples can be recalculated as 9,480 ± 100 ppm (CA) and 9,240 ± 180 ppm (CB). The measured Ca concentrations were 9,360 ± 160 ppm (CA) and 8,950 ± 110 ppm (CB) at $t = 0$ min, just before addition of 10% CO_2 into experiments. The small decrease in Ca concentration following addition of NaOH, but prior to addition of CO_2 gas, could be associated with the formation of the white precipitate; however, these values are within error, suggesting that most if not all Ca remained in solution. The concentration of Ca progressively decreased to 7,800 ± 190 ppm from $t = 0$–40 min (CA) and to 7,660 ± 60 ppm from $t = 0$–30 min (CB). The Ca concentration in Experiment CA stabilized from $t = 40$ min at 7,820 ± 240 ppm, whereas that of CB stabilized from $t = 30$ min at a value of 7,640 ± 160 ppm. The final Ca concentrations reflected removal of 13.4% (CA) and 14.9% (CB) of this element from the FPW.

Accounting for dilution with 1 M NaOH, the Mg concentrations of the original brines were 737 ± 23 ppm (CA) and 727 ± 26 ppm (CB). Mg concentrations decreased to 210 ± 6 ppm (CA) and 214 ± 8 ppm (CB) following titration ($t = 0$ min) such that 71.5% and 70.5%, respectively, of the Mg originally in solution had been removed by the precipitate. As the carbonation experiment proceeded, the concentration of Mg progressively increased to 720 ± 17 ppm (CA) and 681 ± 17 ppm (CB) from $t = 0$–40 min and then stabilized at average values of 715 ± 18 ppm (CA) between $t = 40$–1650 min and 698 ± 18 ppm (CB) between $t = 50$–1650 min. Approximately 0.03% (CA) and 0.04% (CB) of the Mg originally in solution had been removed from the brines when the solution reached steady state.

Sr concentrations were 860 ± 15 ppm (CA) and 856 ± 29 ppm (CB) following titration with 1 M NaOH (t = 0 min). The Sr concentrations had declined to average values of 820 ± 20 ppm (CA) and 810 ± 19 ppm (CB) by t = 15 min in both experiments and did not change significantly between t = 15–1650 min. The concentration of Si (Figure B-3) shows the same trend as observed for Mg. Si was below the detection limit (5.5–5.6 ppm) between t = 0–25 min for both experiments. In Experiment CA, its concentration increased from t = 0–40 min and then plateaued at a value of 9.7 ± 1.1 ppm from 40 minutes until the end of the experiment. In Experiment CB, the concentration of Si increased from t = 0–50 minutes and thereafter plateaued at a value of 9.8 ± 0.5 ppm.

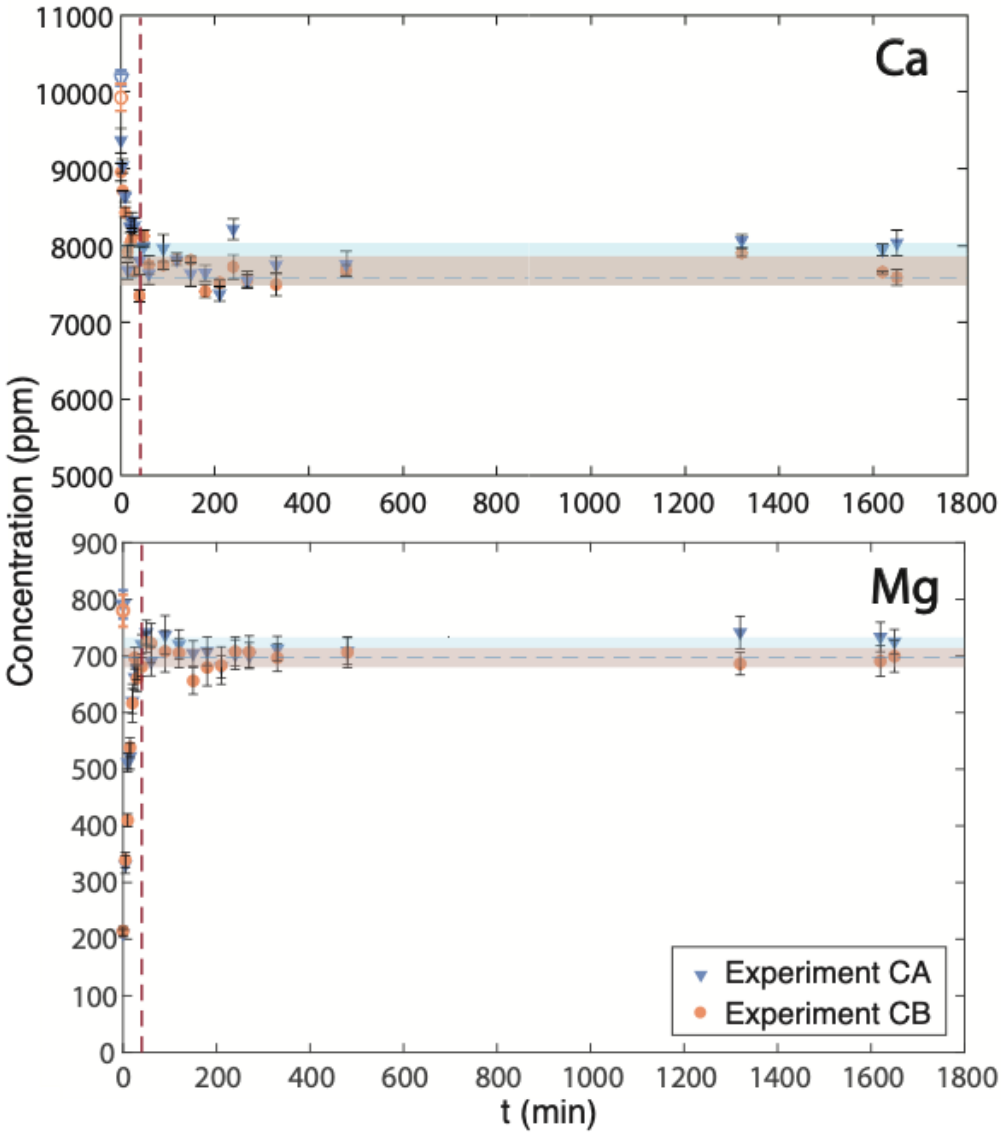

FIGURE 3-2. Mg and Ca concentrations as a function of time. Analytical errors are plotted as one standard deviation. One standard deviation of the average Mg and Ca concentrations when reaching steady state is shaded in blue (Experiment CA) and greyish orange (Experiment CB). The lower boundary of analytical errors of Experiment CA when reaching steady state is plotted as horizontal blue dashed line: area shaded in orange above the line is within one standard deviation of the averaged concentration of Experiment CA when reaching steady state.

3.4.2 Composition of precipitates

Precipitates were characterized using XRD, SEM and ICP-MS. XRD results indicate brucite precipitated immediately upon addition of 1M NaOH to FPW in both experiments. No other crystalline phase was observed in the precipitates at t = 0 min. At t = 5–30 min, calcite was observed in addition to brucite (Figures 3-3, S4 and S5). The abundance of calcite increased from 0 to 100 (wt%) and brucite decreased from 100 to 0 (wt%) between t = 0–40 min (Tables B-9 and B-10). No brucite was detected using XRD in either experiment after 40 minutes, and calcite remained the only detectable crystalline phase from t = 40–1650 min.

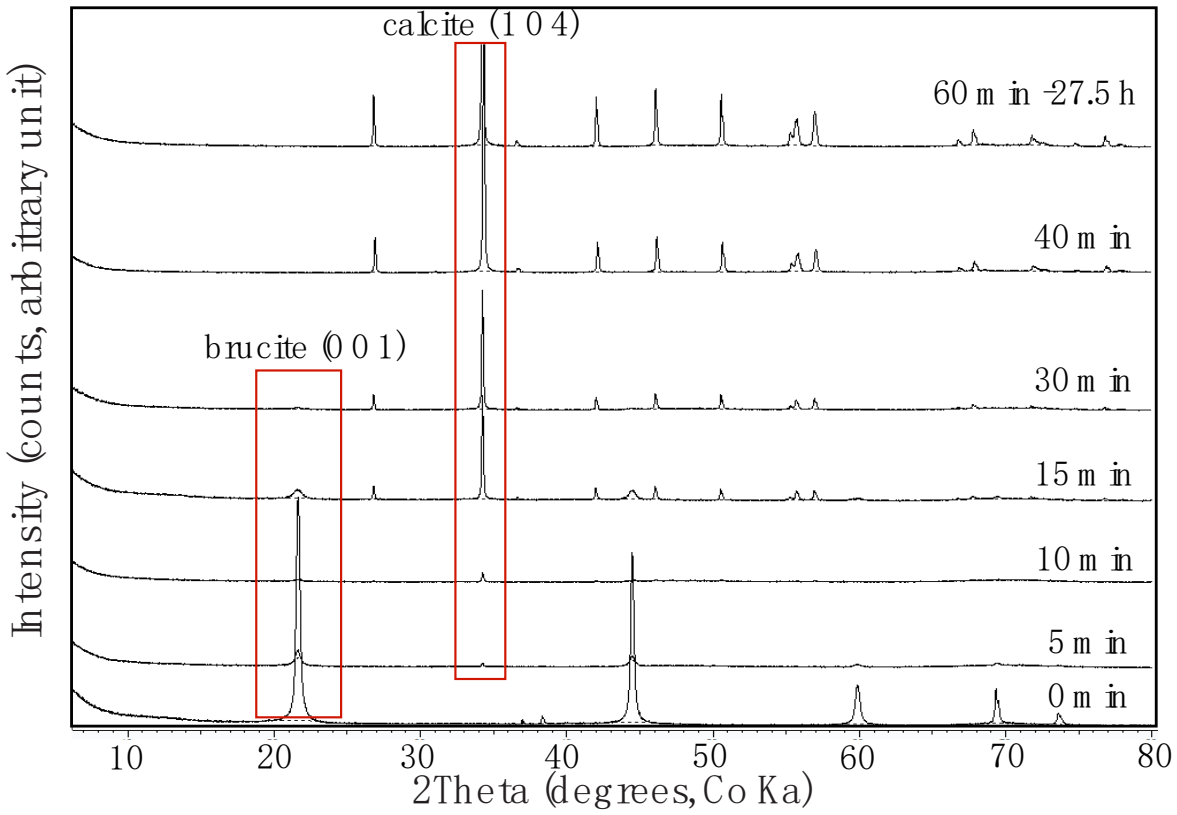

FIGURE 3-3. Representative XRD patterns of the precipitates during carbonation experiments. The most intense peaks of calcite (C) and brucite (B) are labelled with their Miller indices. XRD patterns of all precipitates from the experiments are provided in the Appendix B.

SEM imaging (Figure B-6A) shows that the precipitates from Experiment CA at t = 0 min are composed of ~100 nm brucite crystals. EDX spectra (Figure B-6B) indicate that Si and Mn are commonly associated with brucite. Figure B-6C shows larger (~2 μm) calcite rhombs sampled at t = 240 min. Calcite precipitates consistently contained minor amounts of Mg, Sr and S (Figure B-6D).

3.4.3 Stable carbon and oxygen isotopes

$\delta^{13}C$ and $\delta^{18}O$ values were obtained for nine samples of calcite from Experiment CA and ten samples from Experiment CB (Figure 3-4 and Tables B-7 and B-8). The most negative $\delta^{13}C$ values, -39.7‰ (CA) and -46.6‰ (CB) were obtained at t = 30 min and t = 15 min, respectively. The $\delta^{13}C$ values of calcite became more positive in both experiments until the values stabilized between -32.8‰ and -31.6‰ (CA) and -33.2‰ and -33.5‰ (CB) after t = 270 min. In general, the $\delta^{18}O$ values of calcite became more positive over time, increasing from values of 11.1‰ (CA) and 9.9‰ (CB) at t = 30 min to values in the range of 15.6–18.0‰ (CA) and 17.1–18.1‰ between t = 150–1650 min.

The $\delta^{13}C$ values of DIC were analyzed for seven samples of solution from Experiment CA and eight samples from Experiment CB (Figure 3-4A and Tables B-7 and B-8). DIC concentrations at t < 50 min were too low to permit $\delta^{13}C$ analyses. At t = 50 min, the $\delta^{13}C$ values were -36.4‰ (CA) and -36.2‰ (CB). $\delta^{13}C$ values of DIC became progressively more positive from t = 50–150 min and plateaued from t = 150–1650 min between values from -24.4‰ to -21.0‰ (CA) and -25.7‰ to -23.9‰ (CB).

The $\delta^{18}O$ values of H_2O were analyzed for thirteen samples of solution from Experiments CA and CB (Figure 3-4B and Tables B-7 and B-8). The original brines had the most positive $\delta^{18}O$ values 1.5‰ (CA) and 0.7‰ (CB). After adjusting solution pH by addition of 1M NaOH, the $\delta^{18}O$ values decreased to -0.3‰ (CA) and -0.5‰ (CB) at t = 0 min, respectively. Following the injection of CO_2, the $\delta^{18}O$ values became progressively more negative, reaching values of -0.8‰ (CA) and -1.1‰ (CB) at t = 1650 min, respectively.

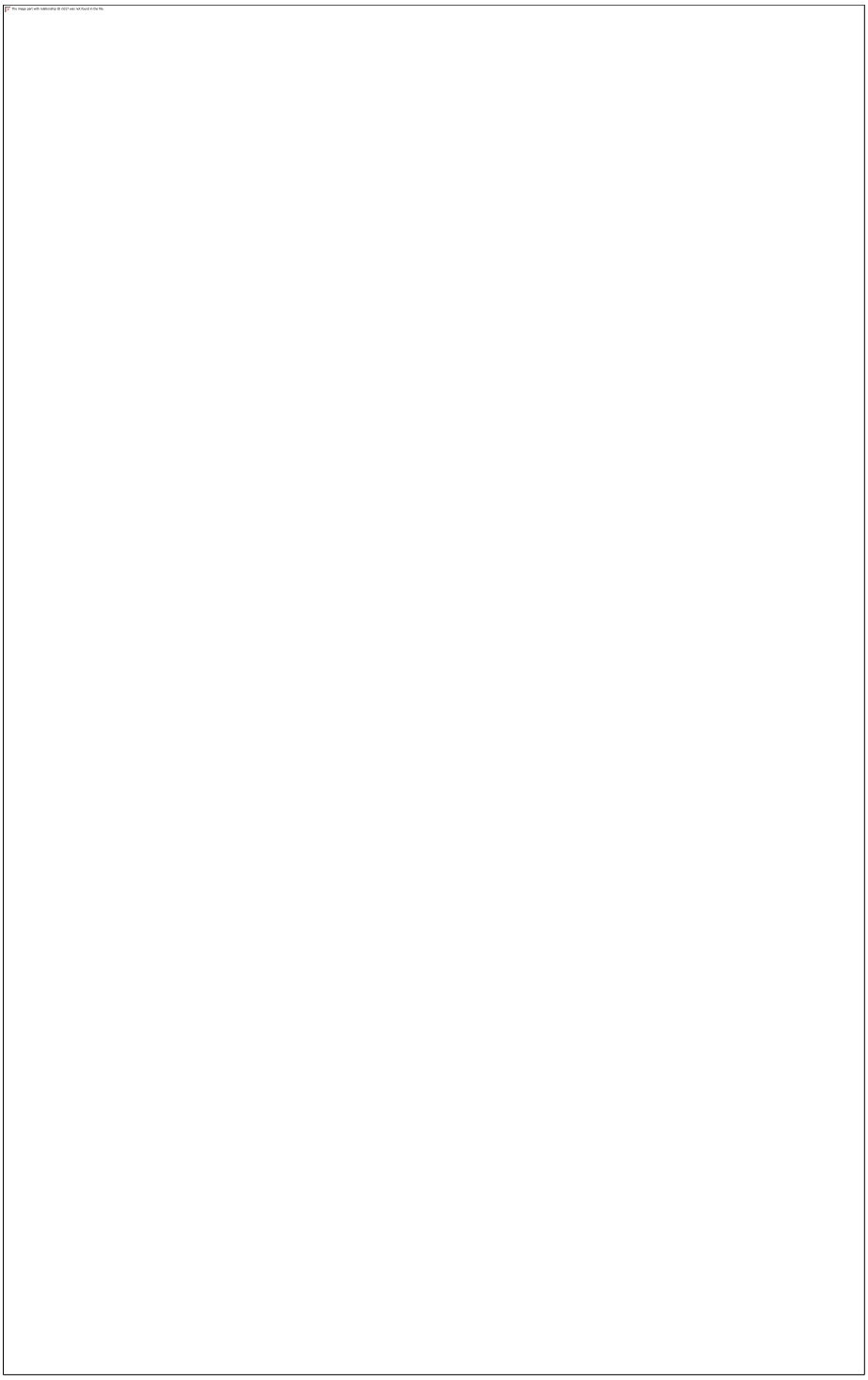

FIGURE 3-4. Stable carbon of oxygen isotope data as a function of time: (A) $\delta^{13}C$ values of DIC in brines and calcite; (B) $\delta^{18}O$ values of water and calcite; and (C) $\Delta^{13}C_{DIC-calcite}$ with respect to time. Uncertainties are smaller than the symbols employed.

3.4.4 Carbon capture over time

Calcite ($CaCO_3$) was the only crystalline phase detected at steady state using XRD and SEM. Owing to the low initial DIC concentration in FPW, the equation for CO_2 captured in precipitates can be simplified to Eq. (1):

$$Ca^{2+}\,(aq) + CO_2\,(g) + H_2O\,(l) \rightarrow CaCO_3\,(s) + 2H^{+}\,(aq) \qquad \text{Eq. (1)}$$

Ca concentrations obtained using ICP-MS (Tables B-9 and B-10) can therefore be used to track CO_2 capture and storage by calcite precipitation. Because precipitation of Ca was negligible following pH titration, the amount of Ca precipitated as calcite at time *t* can be estimated from Eq. (2):

$$\Delta[Ca^{2+}]_t = [Ca^{2+}]_{to} - [Ca^{2+}]_t \qquad \text{Eq. (2)}$$

where $[Ca^{2+}]_{to}$ is the concentration of Ca in solution at t_o = 0 min and $[Ca^{2+}]_t$ is the concentration of Ca in the solution at time *t*. These values are then used to obtain the mass of CO_2 stored (Fig. 6) using the 1:1 molar proportion of CO_2:Ca from Eq. (1). The results indicate that CO_2 removal reaches a maximum value at steady state after *t* = 40 min (CA) and *t* = 30 min (CB). The maximum values for carbon capture obtained in these experiments are 1.71 ± 0.25 g CO_2/L (CA) and 1.41 ± 0.21 g CO_2/L (CB).

Figure 3-5. CO_2 stored as a function of time between (A) t = 0–1650 min and (B) t = 0–200 min. Solid blue (CA) and orange (CB) horizontal lines show the average amount of CO_2 captured at steady state. Blue (CA) and orange (CB) shaded areas indicate 1σ of the average values. The blue dashed line indicates the lower boundary of the blue-shaded area denoting 1σ error in Experiment CA.

3.5 Discussion

3.5.1 Efficiency of carbonation

The initial concentration of Ca in Experiments CA and CB was, respectively, 11.8 times and 12.7 times greater than the Mg concentration (Tables B-9 and B-10 and Figure B-3). Assuming carbonation of Mg and Ca in FPW will produce minerals with a 1:1 molar ratio of metal cation to CO_2 (i.e., nesquehonite, $MgCO_3 \cdot 3H_2O$, and calcite), the CO_2 sequestration potential of Ca in our FPW samples is 7.13 (CA) and 7.68 (CB) times greater than that provided by Mg. If all the dissolved Ca and Mg were carbonated, the duplicate FPW samples used in our study offer carbonation potentials of 12.6 ± 0.2 g CO_2/L (CA) and 12.3 ± 0.2 g CO_2/L (CB), in which Ca can store 11.2 ± 0.1 g CO_2/L and 10.9 ± 0.2 g CO_2/L while Mg can store 1.43 ± 0.04 g CO_2/L and 1.41 ± 0.05 g CO_2/L. Our carbonation experiments indicate that supplying 10% CO_2 in N_2 gas into pH-modified FPW precipitates calcite rapidly at the expense of brucite dissolution, which sacrifices the CO_2 capture potential of Mg. Furthermore, 86.6% (CA) and 85.1% (CB) of Ca initially present in the FPW remained in solution after the experiments reached steady state. The maximum yield of brucite was observed at t = 0 min in both experiments with 71.5% (CA) and 70.5% (CB) of aqueous Mg having been precipitated. If all the precipitated brucite can be carbonated an additional 1.05 ± 0.06 g CO_2/L (CA) and 1.02 ± 0.09 g CO_2/L (CB) would be captured by per liter of FPW. Thus, modifying our methods to preserve and carbonate the precipitated brucite would increase CO_2 storage in Experiment CA from an observed value of 1.71 ± 0.25 g CO_2/L to 2.76 ± 0.31 g CO_2/L (+61.4%). Similarly, CO_2 storage in Experiment CB would increase from 1.41 ± 0.21 g CO_2/L to 2.43 ± 0.30 g CO_2/L (+72.3%). Even without optimization, the carbonation efficiency observed for our study is 13.4% (1.71 ± 0.25 g CO_2/L, CA) and 14.9% (1.41 ± 0.21 g CO_2/L, CB) of the initial Ca in the FPW.

Other mineral carbonation studies have successfully stored CO_2 under ambient conditions through dissolution of highly reactive Ca-bearing solids, such as lime (CaO) and portlandite [$Ca(OH)_2$], and less reactive phases, such as wollastonite ($CaSiO_3$), followed by precipitation of calcite or vaterite. For instance, Ho et al.[136] demonstrated that carbonation of Ca-rich (37.9 wt%) synthetic concrete fines yields 0.19 g CO_2/g of dissolved concrete fines when reacted with 14% CO_2 in N_2 gas in aqueous solution. In addition, Jo et al.[137] showed that the efficiency of Ca carbonation in leachates extracted from CaO-rich coal fly ashes, which had Ca concentrations between 106–1,073 ppm, can be ~9% using 99.9% CO_2 gas. These and other aqueous carbonation experiments requiring extraction of Ca (and Mg) from solid feedstocks generally produce leachates containing orders of magnitude lower Ca concentrations than those already available in FPW (e.g., average of 10,100 ppm used in this study). This use of FPW as a carbonation feedstock is thus advantageous because it does not require use of additional water resources and a greater mass of CO_2 can be sequestered per litre.

Many studies have observed the formation of hydrated Mg-carbonates, such as lansfordite ($MgCO_3 \cdot 5H_2O$), nesquehonite ($MgCO_3 \cdot 3H_2O$), dypingite [$Mg_5(CO_3)_4(OH)_2 \cdot \sim 5H_2O$] and hydromagnesite [$Mg_5(CO_3)_4(OH)_2 \cdot 4H_2O$] from carbonation of brucite during weathering of ultramafic rocks and mine tailings[111,138,139] and in laboratory experiments[3,6,7,61,140–142] done at ambient conditions. Although the aqueous conditions in our experiments at t = 0 min were similar to those employed in previous studies of brucite carbonation, they did not produce hydrated Mg-carbonates following injection of 10% CO_2. We performed PHREEQC modelling to investigate the factors preventing formation of hydrated Mg-carbonate minerals from brucite. Water chemistry data from t = 90 min of both experiments were used for modelling because DIC had reached a maximum value and ion concentrations had stabilized by this time point.

3.5.2 Geochemical modelling to optimize carbonation efficiency

Although the pitzer.dat database is generally more suitable for modelling solutions with high ionic strength, it lacks thermodynamic data for many aqueous species compared to the phreeqc.dat database, making it less accurate for modelling the saturation indices of minerals for FPW.[77] As such, the results described here were obtained using the phreeqc.dat database. First, models were made to predict DIC concentrations for pH-amended FPW in equilibrium with atmospheric CO_2 (0.04%) and 10% CO_2 in N_2. The FPW used in our experiments should contain 27.0 mg C/L (CA) and 26.6 mg C/L (CB) of total inorganic carbon, when in equilibrium with atmospheric CO_2. When in equilibrium with 10% CO_2, the FPW should contain 64.6 mg C/L (CA) and 63.8 mg C/L (CB) of total inorganic carbon. These results are similar to those measured for the concentration of DIC in Experiments CA and CB at t = 90 min (Figure 3-1B), indicating that the pH-modified FPW was close to equilibrium with respect to CO_2 at the time DIC sample was collected, which was sampled immediately during the experiment at t = 90 min. At the same time, hydrated Mg-carbonates (nesquehonite, dypingite and hydromagnesite) remained undersaturated at t = 90 min in both experiments. Increasing the pH of the modelled solutions at t = 90 min in PHREEQC indicates that this is the major control that limits preservation and carbonation of brucite in both experiments. Hydromagnesite reaches supersaturation between pH 10.0–10.5 (CA) and 9.5–10.0 (CB), dypingite reaches supersaturation between pH 10.5–11.0 (CA and CB), and nesquehonite cannot reach supersaturation only by adjusting solution pH, instead DIC must be increased as well to form nesquehonite. Overall, modelling results indicate that pH > 10 must be maintained to drive conversion of brucite to hydrated Mg-carbonates and to continue calcite precipitation during reaction with a continuous supply of 10% CO_2.

SEM-EDX (Figure B-6) and ICP-MS (Figure B-3) results indicate that Si was associated with brucite precipitates that formed following titration of FPW to pH 10.5, suggesting the formation of a Mg-silicate phase. Thermodynamic modelling with PHREEQC indicates that the FPW becomes supersaturated with respect to kerolite [$Mg_3Si_4O_{10}(OH)_2 \cdot nH_2O$], a low-temperature talc-like phase, at pH > 10.4. Previous studies have observed the formation of poorly ordered or amorphous Mg-rich phyllosilicates in saline and alkaline lakes at ambient conditions.[143] Tosca and Macdonald[144] and Tosca and Masterson[145] observed formation of poorly crystalline kerolite from solutions with high pH and high Mg/Si ratios at 25 °C — conditions that are similar to those in our experiments. No silicate minerals were observed in our XRD patterns; therefore, the Mg-silicate phase is likely to be amorphous, nanocrystalline and/or present below the detection limit of the conditions we used to collect diffraction data (typically <0.5 wt% for most phases).

Because aqueous silica competes with DIC for Mg during mineral carbonation, it is important to account for the role of silicic acid, H_4SiO_4. For instance, an investigation using Mg isotopes revealed that >70% of Mg released from dissolved basalts in the Carbfix project was precipitated as Mg-phyllosilicates instead of carbonate minerals.[146] Owing to the decrease in pH when 10% CO_2 was supplied to our experiments, the concentrations of aqueous Si increased over time, which indicates that the Mg-silicate phase(s) dissolved back into the solution. We did not observe any association of Si with the calcite precipitated following brucite dissolution at circumneutral pH (Figure B-6). Our elemental analyses (Figure B-3 and Tables B-9 and B-10) indicate the concentrations of Mg in the FPW samples are almost 100 times greater than those of Si, which would lead only to a small decrease in the efficiency of Mg carbonation even if all the aqueous silica in FPW were to form Mg-phyllosilicates. As a result, maintaining pH > 10 to promote brucite

carbonation and continuous formation of calcite would not sacrifice much of the carbonation potential of Mg in FPW to the formation of Mg-silicate clays.

3.5.3 Stable isotopic compositions of solution and precipitates

Precipitation of carbonate minerals preferentially takes up isotopically heavier ^{13}C from DIC, which results in precipitates with more positive $\delta^{13}C$ values.[147–149] However, our $\delta^{13}C$ results indicate that calcite was isotopically lighter than the DIC in FPW at the time of analysis (Figure 3-4C and Tables B-7 and B-8). The average values for $\Delta^{13}C_{DIC–calcite}$ were 10.3 ± 2.1‰ (CA) and 8.5 ± 1.1‰ (CB) at steady state from t = 150–1650 min (Figure 3-4C), which cannot be explained by equilibrium isotope fractionation ($10^3 ln\alpha_{CaCO3–HCO3^-}$ = 2.0‰ at t = 18.0 °C)[150] or kinetic isotopic fractionation associated with differences in precipitation rate ($\varepsilon^{13}C_{CaCO3–HCO3^-}$ = 0.4–3.4‰ at 25 °C)[151]. One possible cause of the unusual isotopic signatures in DIC and calcite is degassing of aqueous CO_2 from solutions between sampling and during measurement of stable carbon isotopes. For instance, loss of CO_2 gas was observed during sampling by Sade et al. (2020)[148] who obtained a similar result to that reported here: following partial degassing, the residual DIC was more enriched in ^{13}C than the witherite ($BaCO_3$) that had precipitated from the original DIC pool.

At Earth's surface conditions, CO_2 degasses from natural waters when there is a dramatic decrease in pCO_2 at the air–water interface. This commonly occurs at the groundwater–stream interface in watersheds and during transport of CO_2-saturated water from upstream to downstream.[149,152–156] Deirmendjian and Abril[152] demonstrated that when pCO_2 is decreased rapidly from 4.1% or 4.7% to atmospheric concentration (~0.04%), degassing of DIC from CO_2-saturated solutions (pH < 7.2) can result in an enrichment of ^{13}C in DIC of 7.8 ± 0.9‰ and 12.3 ± 1.2‰, respectively, with greater

enrichments associated with greater differences in pCO_2. As such, it is likely that some DIC was lost as CO_2 gas during sampling and filtration of FPW, when pCO_2 shifted from 10% to atmospheric level. The measured values for $\delta^{13}C$ of DIC in our study most likely reflect the isotopic composition of aqueous carbonate species after degassing whereas the $\delta^{13}C$ values of calcite reflect the composition of the DIC pool before degassing. Hence, the impact of degassing is only reflected in the $\delta^{13}C$ values of DIC.

A linear mixing model can be used to estimate how much DIC was degassed from our experiments. As the $\delta^{13}C$ values of both DIC and calcite reached steady state from t =150–1650 min, we can assume equilibrium fractionation of stable carbon isotopes between calcite and DIC before degassing. Here, we also assume that isotopic equilibrium is reached between degassed CO_2 and the residual pool of DIC left in solution. The fraction of DIC left in solution after degassing (f_{DICf}) can thus be calculated by mass-balance using Eq. (3):

$$\delta^{13}C_{DICf} \bullet f_{DICf} + \delta^{13}C_{CO2f} \bullet (1 - f_{DICf}) = \delta^{13}C_{DICi} \qquad \text{Eq. (3)}$$

The pH value of the FPW solutions at steady state (t = 150–1650 min) was ~6.1, where bicarbonate (HCO_3^-) is the dominant DIC species. The initial carbon isotopic compositions of DIC samples before degassing, $\delta^{13}C_{DICi}$, can be estimated from measured values for $\delta^{13}C_{calcite}$ using the equilibrium carbon isotopic fractionation factor of Deines et al.[150]: $\delta^{13}C_{DICi} = \delta^{13}C_{calcite} - 10^3 \ln\alpha_{calcite-HCO3^-} = \delta^{13}C_{calcite} - 2.0‰$ at 18.0 °C. Similarly, the value for $\delta^{13}C_{DICi}$ can also be determined using the following equation assuming isotopic equilibrium during degassing of CO_2: $\delta^{13}C_{DICf} = \delta^{13}C_{DICi} - 10^3 \ln\alpha_{HCO3^-–CO2(g)} = \delta^{13}C_{DICi} - 8.7‰$ at 18.0 °C based on the equilibrium carbon isotopic fractionation factor from Mook et al.[157]. $\delta^{13}C_{DICf}$ and $\delta^{13}C_{calcite}$ are measured values for the stable carbon isotopic composition of the residual DIC pool following degassing and of

calcite precipitated before degassing, respectively, at a given sampling time, *t*. Calculated values for, f_{DICf} range from 0.4–0.5 (average = 0.42) for Experiment CA and from 0.4–0.5 (average = 0.45) for Experiment CB, which means that more than half the CO_2 that was dissolved into solution was lost to degassing.

Geochemical modelling using PHREEQC with the phreeqc.dat database indicates that the equilibrium concentration of DIC at pCO_2 = 10% is 64.6 mg C/L (CA) and 63.8 mg C/L (CB) at 18.0 °C. When the DIC is in equilibrium with atmospheric CO_2 (0.04%), the concentration decreases to 27.0 mg C/L (CA) and 26.6 mg C/L (CB) at 18.0 °C (plotted in Figure 3-1B). Thus, our modelling predicts that 42%, or f_{DICf} = 0.42, of the DIC that was in solution at pCO_2 =10% would remain following equilibration with the much lower partial pressure of atmospheric CO_2. This result provides a very close match to the values obtained using stable isotope data and our linear mixing model. Therefore, the extent of CO_2 degassing is completely controlled by its solubility with respect to CO_2 partial pressure, which we have shown can be predicted accurately with geochemical modelling.

Alkalinity (Figure B-2) was measured at different times for Experiments CA and CB following sample collection. Alkalinity values of samples from Experiment CA were measured within 30 minutes of sampling whereas those for Experiment CB were measured ~27 hours after sampling. Figure B-2 shows that the alkalinity of samples from Experiment CA are closer to the modelled equilibrium DIC values for pCO_2 = 10% whereas the alkalinity values for Experiment CB are consistent with the modelled equilibrium DIC concentration at pCO_2 = 0.04%. Therefore, the results indicate that degassing was complete, and that DIC had re-equilibrated with the atmosphere, within 27 hours of stopping the supply of 10% CO_2 gas.

3.5.4 Implications for process design to enhance FPW carbonation

Our study shows that FPW can be used for CO_2 capture and storage via mineralization at ambient conditions. The process used here can be refined to access more of the carbonation potential of FPW by: (1) Adding more base (e.g., NaOH) to keep pH > 10 in order to maintain saturation with respect to brucite, to drive continued precipitation of calcite and to keep CO_2 in solution; (2) Considering a separation step where brucite precipitated at t = 0 min is filtered and removed from FPW prior to CO_2 injection so that it can be carbonated in a separate process using a lower, optimal water–rock ratio (i.e., after Assima et al.[158]; Harrison et al.[62]; Hamilton et al.[159]; McQueen et al.[88]). Increasing the flowrate of gaseous CO_2[160], stirring the solutions during carbonation and trialing the use of more economic base treatments (e.g., NH_3) may also be beneficial.

Our experiments demonstrate that calcite precipitated from duplicate FPW samples stored 1.71 ± 0.25 g CO_2/L (CA) and 1.41± 0.21 g CO_2/L (CB). Removing and carbonating brucite before calcite precipitation would increase the amount of storage to 2.76 ± 0.31 g CO_2/L (CA) and 2.43 ± 0.30 g CO_2/L (CB). Optimizing the process to carbonate all of the dissolved Ca and Mg in this FPW would store a maximum of 12.6 ± 0.2 g CO_2/L (CA) and 12.3 ± 0.2 g CO_2/L (CB). Unlocking the full carbonation potential of FPW might be achieved with the combination of high pCO_2 gas streams from Direct Air Capture plants[135] or looping methods[161]. Notably, the oil and gas industry in North America generates FPW at a scale of 10s–100s Mt annually.[38] Despite the heterogeneity of FPW across formations and countries[38,72,133], completely unlocking its carbonation potential could sequester at least kT–Mt CO_2 annually[133].

CHAPTER 4: Conclusions and Future Directions

4.1. Conclusions

It is hard to make predictions about mineral precipitation from FPW as it contains complex inorganic and organic compounds. Therefore, two batch-experiments were designed and carried out to systematically investigate the effects of pH and pCO_2 on mineral precipitation and the efficiency of CO_2 capture. I used the results of these experiments to estimate the annual CO_2 sequestration potential of the FPW produced in Canada, China, and the US. To my knowledge, this is the first assessment of this resource for its CO_2 sequestration potential considering the rate and efficiency at ambient conditions. Furthermore, I documented the fate of B, Ba, Fe, Li, Mn, Ni, Pb, S, Si, Sr, and Zn during carbonation of FPW to assess whether this process provides co-benefits for water treatment and metal resource recovery.

The first set experiments (Chapter 2) investigated the effect of pH (8.5–12.0, n = 8) on mineral precipitation and the efficiency of cation extraction from FPW using CO_2 removal from laboratory air. By recording the mass and analysing the mineralogy of precipitates, it was possible to measure the amount of CO_2 captured by the precipitates as well the maximum carbonation potential achievable by carbonating residual hydroxide minerals. Direct measurement of the amounts of Ca and Mg removed from solutions allowed another measure of CO_2 removal as well as estimates of maximum sequestration potential assuming all Ca and Mg is carbonated to calcite/aragonite and nesquehonite, respectively.

Precipitates from these experiments consisted of calcite, brucite, and occasionally aragonite and portlandite. Whether calcite or aragonite is more likely to precipitate from FPW depends on the Ca and Mg ratio of the original brines. Contrastingly, the precipitation of portlandite is only dependent on pH and it was only observed at pH > 12.0. In spite of the high ionic strength of the

FPW samples, PHREEQC modeling with the phreeqc.dat database was used to successfully predict the mineralogy of precipitates. This style of modelling could therefore be applied to support design and optimization of industrial-scale FPW carbonation reactions.

Chapter 2 also calculates (1) the minimum amount of CO_2 captured by carbonate precipitates, (2) the potential to sequester CO_2 when hydroxide precipitates are carbonated, and (3) the mass of CO_2 that can be sequestered if Ca and Mg removed from solution and carbonated. All three of these values increase with increasing pH. At pH 12.0, these three values reach 0.99 g CO_2/L, 3.87 g CO_2/L, and 7.94 g CO_2/L, respectively, from the average values of the four brine samples used in the first set of experiments. The average maximum potential of CO_2 capture of these four brine samples, 7.94 gCO_2/L, could be multiplied many times over if the precipitates were deployed in an efficient Ca- and Mg-looping plant, where multiple cycles of air capture by the precipitates and calcining were applied.

The second set of experiments, described in Chapter 3, explored whether increasing the supply of CO_2 into FPW enhances the rate and efficiency of CO_2 capture via mineral carbonation at ambient conditions. A 10% CO_2 in N_2 gas mix was used, which is within the range of CO_2 concentrations in flue gas[134]. The pH of the FPW samples was adjusted to 10.5, at which both brucite and calcite were observed to precipitate in Chapter 2. The mineral carbonation reaction reached steady-state and maximum CO_2 capture was achieved within 40 minutes. Brucite dissolved during the reaction and calcite was the only mineral phase that contributed to CO_2 sequestration, which had an average value of 1.56 ± 0.32 g CO_2/L of FPW. This represents a ~9-fold increase in the amount of CO_2 sequestered using 10% CO_2 gas compared to the amount of atmospheric CO_2 captured by precipitates (0.174 g CO_2/L) at the same pH (Chapter 2). In addition, both the atmospheric and 10% CO_2 experiments showed that elements including Ba, Br, Cu, Fe, Li, Mn, S, Sr, Pb, and Zn are

immobilized by the precipitates during mineral carbonation. The immobilized elements have potential to be recovered for use or simply removed from the FPW.

The longevity of CO_2 solubility trapping in FPW was examined using stable carbon isotopes and the concentration of dissolved inorganic carbon. The results of stable carbon isotopic modeling and PHREEQC modeling indicate that the concentrated CO_2 injected into FPW degassed to reach the equilibrium DIC concentration with respect to the pCO_2 of the atmospheric (~0.04%) within 24 hours. Thus, to prevent release of CO_2, the rate of supply needs to be controlled and it must be stopped once the reaction reaches steady state. Moreover, stable carbon isotopes provide evidence that CO_2 dissolution and mineral precipitation reactions reached equilibrium within 270 minutes even though an average of 85.9 % of the Ca and all the Mg remained in solution. Therefore, there is an opportunity to sequester more CO_2 with the remaining Ca and Mg in the solutions either by increasing the pH of the initial solutions or by titrating base throughout the carbonation reaction.

The results of Chapter 2 confirm the proposal of Ferrini et al.[37] that the Mg cations in hydraulic flowback and produced water can be used for CO_2 capture at ambient conditions. This thesis shows for the first time that both Ca and Mg can be extracted from FPW by elevating the solution pH and that most of the CO_2 sequestration potential of FWP is associated with Ca, which is easier to precipitate at circumneutral pH than Mg. At atmospheric pCO_2, precipitation of hydroxide phases from FPW indicates that mineral precipitation outpaces CO_2 dissolution within the 24-hour timeframe of these experiments. Thus, at atmospheric pCO_2, CO_2 supply is the rate-limiting step. The results of Chapter 3 then showed that increasing the pCO_2 to 10% overcame the slow rate of CO_2 dissolution, allowing both DIC concentration and mineral precipitation to reach equilibrium within 270 minutes and yielding a 9-fold increase in the amount of CO_2 sequestered. Hence, the efficiency of CO_2 capture was improved, and the reaction time of mineral carbonation was

shortened. However, there was still 85.9% of the initial Ca remaining in solution at steady state because the system was alkalinity-starved, which is attributed to the rapid consumption of alkalinity by calcite precipitation and the lack of alkalinity input during the carbonation reactions. The low concentrations of alkalinity observed when the reaction reached steady state, and a maximum value was observed for CO_2 capture, can be overcome by addition of basic chemicals (i.e. NaOH). In conclusion, increasing both pH and pCO_2 is needed to promote efficient and rapid mineral carbonation using FPW.

4.2. Future Directions

The experimental design and the combination of pH and CO_2 conditions used in this thesis might not reflect the optimal conditions or the most economic solutions needed to fully unlock the carbonation potential FPW. Therefore, further research needs to be conducted to optimize the efficiency of mineral carbonation using FPW and to assess whether it is economically feasible to implement at scale.

The unresolved challenges identified in this thesis include:

(1) The Ca and Mg in FPW were not fully extracted for mineral carbonation. Maximizing extraction of both Ca and Mg is also difficult to achieve at the same time. At elevated pCO_2, the pH of FPW must be maintained ≥ pH 8.0 to supply sufficient alkalinity until calcite precipitation goes to completion. As calcite was observed to precipitate at the expense of brucite dissolution at elevated pCO_2, remedies need to be found to fully utilize both the Ca and Mg from FPW for mineral carbonation. The optimal combination of pH and pCO_2 needed to simultaneously carbonate brucite and produce calcite should be explored. Alternatively, step-by-step extraction of Mg as brucite followed by Ca as calcite should also be considered.

(2) A comprehensive database, including the annual production volume and water chemistry of hydraulic fracturing flowback and produced waters, by formation and country, is needed before a more accurate estimation of CO_2 sequestration potential in FPW can be made. Similarly, the potential of brine carbonation should be extended to other, more plentiful waste waters produced by the oil and gas industry.

(3) The use of basic reagents (NaOH in this thesis) is needed to elevate pH and supply alkalinity for FPW carbonation. It will be important to assess the use of more economical reagents for this purpose. For example, utilizing low-cost alkaline industrial waste materials (e.g. hydrotalcite supergroup minerals from mine wastes) could be explored to deliver atmospheric CO_2 and alkalinity into solution during anion exchange and partial dissolution in FPW while buffering the system.[3]

(4) The delivery of high pCO_2 gases into the aqueous system needs to be carefully controlled and terminated when the carbonation reaction is complete to avoid release of CO_2 back to the atmosphere.

(5) Finally, Life Cycle Assessment and Techno-economic Analysis (LCA/TEA) is needed to assess the viability of this process for implementation as a CDR method for the oil and gas sector that both capitalizes on existing industry knowledge in CCS while valorizing abundant FPW as a resource.

REFERENCES

(1) IPCC, 2018: Global Warming of 1.5°C. An IPCC Special Report on the impacts of global warming of 1.5°C above pre-industrial levels and related global greenhouse gas emission pathways, in the context of strengthening the global response to the threat of climate change, sustainable development, and efforts to eradicate poverty, 2019. https://www.ipcc.ch/site/assets/uploads/sites/2/2019/06/SR15_Full_Report_High_Res.pdf (Accessed November 16, 2020).

(2) United Nations Framework Convention on Climate Change: https://unfccc.int/process-and-meetings/the-paris-agreement/the-paris-agreement

(3) Power, I. M.; Harrison, A. L.; Dipple, G. M.; Wilson, S. A.; Kelemen, P. B.; Hitch, M.; Southam, G. Carbon mineralization: from natural analogues to engineered systems. *Rev. Mineral. Geochem.* **2013**, *77*, 305–360.

(4) Rock Solid: Harnessing Mineralization for Large-Scale Carbon Management; Energy Future Initiative: Washington, DC, 2020; https://www.ourenergypolicy.org/resources/rock-solid-harnessing-mineralization-for-large-scale-carbon-management/.

(5) Wilson, S. A.; Dipple, G. M.; Power, I. M.; Thom, J. M.; Anderson, R. G.; Raudsepp, M.; Gabites, J. E.; Southam, G. Carbon dioxide fixation within mine wastes of ultramafic-hosted ore deposits: examples from the Clinton Creek and Cassiar Chrysotile deposits. *Canada. Econ. Geol.* **2009**, *104*, 95–112.

(6) Wilson, S. A.; Barker, S. L. L.; Dipple, G. M.; Atudorei, V. Isotopic disequilibrium during uptake of atmospheric CO_2 into mine process waters: Implications for CO_2 sequestration. *Environ. Sci. Technol.* **2010**, *44*, 9522−9529.

(7) Harrison, A. L.; Power, I. M.; Dipple, G. M. Accelerated carbonation of brucite in mine tailings for carbon sequestration. *Environ. Sci. Technol.* **2012**, *47*, 126−134.

(8) Park, A. H. A.; Fan, L. S. CO_2 mineral sequestration: physically activated dissolution of serpentine and pH swing process. *Chem. Eng. Sci.* **2004**, *59* (22–23), 5241–5247.

(9) Seifritz, W. CO_2 Disposal by means of silicates. *Nature* **1990**, *345*, 486. https://doi.org/10.1038/345486b0.

(10) Lackner, K. S.; Wendt, C. H.; Butt, D. P.; Joyce, E. L.; Sharp, D. H. Carbon dioxide disposal in carbonate minerals. *Energy* **1995**, *20*, 1153.

(11) Gerdemann, S. J.; O'Connor, W. K.; Dahlin, D. C.; Penner, L. R.; Rush, H. Ex situ aqueous mineral carbonation. *Environ. Sci. Technol.* **2007**, *41*, 2587–2593. https://doi.org/10.1021/es0619253.

(12) Wilson, S. A.; Raudsepp, M.; Dipple, G. M. Verifying and quantifying carbon fixation in minerals from serpentine-rich mine tailings using the Rietveld method with X-ray powder diffraction data. *Am. Mineral.* **2006**, *91* (8–9), 1331–1341.

(13) Schuiling, R. D.; Krijgsman, P. Enhanced weathering: an effective and cheap tool to sequester CO_2. *Clim. Change* **2006**, *74*, 349–354. https://doi.org/10.1007/s10584-005-3485-y.

(14) Renforth, P.; Manning, D. A. C.; Lopez-Capel, E. Carbonate precipitation in artificial soils as a sink for atmospheric carbon dioxide. *Appl. Geochemistry* **2009**, *24*, 1757–1764.

(15) Gislason, S. R.; Wolff-Boenisch, D.; Stefansson, A.; Oelkers, E. H.; Gunnlaugsson, E.; Sigurdardottir, H.; Sigfusson, B.; Broecker, W. S.; Matter, J. M.; Stute, M.; Axelsson, G.; Fridriksson, T. Mineral sequestration of carbon dioxide in basalt: a pre-injection overview of

the CarbFix project. *Int. J. Greenh. Gas Control* **2010**, *4*, 537–545. https://doi.org/10.1016/j.ijggc.2009.11.013.

(16) Kelemen, P. B.; Matter, J. In situ carbonation of peridotite for CO_2 storage. *Proc. Natl. Acad. Sci. U. S. A.* **2008**, *105*, 17295–17300. https://doi.org/10.1073/pnas.0805794105.

(17) Matter, J. M.; Stute, M.; Snaebjornsdottir, S. O.; Oelkers, E. H.; Gislason, S. R.; Aradottir, E. S.; Sigfusson, B.; Gunnarsson, I.; Sigurdardottir, H.; Gunnlaugsson, E.; Axelsson, G.; Alfredsson, H. A.; Wolff-Boenisch, D.; Mesfin, K.; Taya, D. F. d. l. R.; Hall, J.; Dideriksen, K.; Broecker, W. S. Rapid carbon mineralization for permanent disposal of anthropogenic carbon dioxide emissions. *Science* **2016**, *352*, 1312−1314.

(18) Ruiz-Agudo, E.; Kudłacz, K.; Putnis, C. V.; Putnis, A.; Rodriguez-Navarro, C. Dissolution and carbonation of portlandite [$Ca(OH)_2$] single crystals. *Environ. Sci. Technol.* **2013**, *47* (19), 11342–11349.

(19) Han, Y. S.; Gunawan, H.; Masayoshi, F.; Minoru, T. Crystallization and transformation of vaterite at controlled pH. *J. Cryst. Growth* **2006**, *289*, 269– 274.

(20) Zhao, H.; Park, Y.; Lee, D. H.; Park, A. H. A. Tuning the dissolution kinetics of wollastonite via chelating agents for CO_2 sequestration with integrated synthesis of precipitated calcium carbonates. *Phys. Chem. Chem. Phys.* **2013**, *15*, 15185–15192. https://doi.org/10.1039/c3cp52459k.

(21) Jimoh, O. A.; Ariffin, K. S.; Hussin, H. Bin; Temitope, A. E. Synthesis of precipitated calcium carbonate: a review. *Carbonates and Evaporites* **2018**, *33*, 331–346. https://doi.org/10.1007/s13146-017-0341-x.

(22) Power, I. M.; Wilson, S. A.; Thom, J.; Dipple, G. M.; Southam, G. Biologically induced mineralization of dypingite by cyanobacteria from an alkaline wetland near Atlin, British Columbia, Canada. *Geochem. Trans.* **2007**, *8*, article 13.

(23) Power, I. M.; Wilson, S. A.; Thom, J. M.; Dipple, G. M.; Gabites, J. E.; Southam, G. The hydromagnesite playas of Atlin, British Columbia, Canada: A biogeochemical model for CO_2 sequestration. *Chem. Geol.* **2009**, *260* (3–4), 286–300. https://doi.org/10.1016/j.chemgeo.2009.01.012.

(24) Friedlingstein, P.; Jones, M. W.; O'Sullivan, M.; Andrew, R. M.; Hauck, J.; Peters, G. P.; Peters, W.; Pongratz, J.; Sitch, S.; Le Quéré, C.; et al. Global carbon budget 2019. *Earth Syst. Sci. Data* **2019**, *11* (4), 1783–1838.

(25) Pronost, J.; Beaudoin, G.; Lemieux, J. M.; Hébert, R.; Constantin, M.; Marcouiller, S.; Klein, M.; Duchesne, J.; Molson, J. W.; Larachi, F.; Maldague, X. CO_2-depleted warm air venting from chrysotile milling waste (Thetford mines, Canada): evidence for in-situ carbon capture from the atmosphere. *Geology* **2012**, *40* (3), 275–278.

(26) Assima, G. P.; Larachi, F.; Beaudoin, G.; Molson, J. Dynamics of carbon dioxide uptake in chrysotile mining residues - effect of mineralogy and liquid saturation. *Int. J. Greenhouse Gas Control* **2013**, *12*, 124–135.

(27) Assima, G. P.; Larachi, F.; Molson, J.; Beaudoin, G. Emulation of ambient carbon dioxide diffusion and carbonation within nickel mining residues. *Miner. Eng.* **2014**, *59*, 39–44.

(28) Oskierski, H. C.; Dlugogorski, B. Z.; Jacobsen, G. Sequestration of atmospheric CO_2 in chrysotile mine tailings of the Woodsreef Asbestos Mine, Australia: Quantitative mineralogy, isotopic fingerprinting and carbonation rates. *Chem. Geol.* **2013**, *358*, 156–169. https://doi.org/10.1016/j.chemgeo.2013.09.001.

(29) Renforth, P. The negative emission potential of alkaline materials. *Nat. Commun.* **2019**, *10* (1), 1401.

(30) Huijgen, W. J. J.; Witkamp, G. J.; Comans, R. N. J. Mineral CO_2 sequestration by steel slag carbonation. *Environ. Sci. Technol.* **2005**, *39* (24), 9676–9682.

(31) Fernández Bertos, M.; Simons, S. J. R.; Hills, C. D.; Carey, P. J. A review of accelerated carbonation technology in the treatment of cement-based materials and sequestration of CO_2. *J. Hazard. Mater.* **2004**, *112* (3), 193–205.

(32) Xi, F.; Davis, S. J.; Ciais, P.; Crawford-Brown, D.; Guan, D.; Pade, C.; Shi, T.; Syddall, M.; Lv, J.; Ji, L.; Bing, L.; Wang, J.; Wei, W.; Yang, K. H.; Lagerblad, B.; Galan, I.; Andrade, C.; Zhang, Y.; Liu, Z. Substantial global carbon uptake by cement carbonation. *Nat. Geosci.* **2016**, *9* (12), 880–883.

(33) Renforth, P.; Mayes, W. M.; Jarvis, A. P.; Burke, I. T.; Manning, D. A. C.; Gruiz, K. Contaminant mobility and carbon sequestration downstream of the Ajka (Hungary) red mud spill: The effects of gypsum dosing. *Sci. Total Environ*. **2012**, *421–422*, 253–259.

(34) Yadav, V. S.; Prasad, M.; Khan, J.; Amritphale, S. S.; Singh, M.; Raju, C. B. Sequestration of carbon dioxide (CO_2) using red mud. *J. Hazard. Mater.* **2010**, *176* (1–3), 1044–1050.

(35) Maries, A.; Hills, C. D.; Carey, P.; Ostle, S.; Maries, A.; Hills, C. D.; Carey, P.; Ostle, S. Linked low carbon manufacture of cement and precast concrete. *Adv. Appl. Ceram.* **2013**, *112*, 202-206. https://doi.org/10.1179/1743676112Y.0000000057.

(36) Hills, C. D.; Tripathi, N.; Singh, R. S.; Carey, P. J.; Lowry, F. Valorisation of agricultural biomass-ash with CO_2. *Sci. Rep.* **2020**, *10* (1). https://doi.org/10.1038/s41598-020-70504-1.

(37) Ferrini, V.; Vito, C.D.; Mignardi S. Synthesis of nesquehonite by reaction of gaseous CO_2 with Mg chloride solution: its potential role in the sequestration of carbon dioxide. *J. Hazard.*

Mater. **2009**, *168*, 2–3.

(38) Zolfaghari, A. University of Alberta, Edmonton. Personal communication, June, 2021.

(39) Zou, C.; Ni, Y.; Li, J.; Kondash, A.; Coyte, R.; Lauer, N.; Cui, H.; Liao, F.; Vengosh, A. the water footprint of hydraulic fracturing in Sichuan Basin, China. *Sci. Total Environ.* **2018**, *630*, 349–356.

(40) Bagheri, R.; Nadri, A.; Raeisi, E.; Eggenkamp, H. G. M.; Kazemi, G. A.; Montaseri, A. Hydrochemical and isotopic ($\Delta^{18}O$, $\Delta^{2}H$, $^{87}Sr/^{86}Sr$, $\Delta^{37}Cl$ and $\Delta^{81}Br$) evidence for the origin of saline formation water in a gas reservoir. *Chem. Geol.* **2014**, *384*, 62–75. https://doi.org/10.1016/j.chemgeo.2014.06.017.

(41) Stringfellow, W. T.; Domen, J. K.; Camarillo, M. K.; Sandelin, W. L.; Borglin, S. Physical, chemical, and biological characteristics of compounds used in hydraulic fracturing. *J. Hazard. Mater.* **2014**, *275*, 37–54.

(42) He, Y.; Sun, C.; Zhang, Y.; Folkerts, E.J.; Martin, J. W.; Goss, G. G., Developmental toxicity of the organic fraction from hydraulic fracturing flowback and produced waters to early life stages of zebrafish (Danio rerio). *Environ. Sci. Technol.* **2018**, *52*, 820–3830.

(43) Flynn, S.L.; von Gunten, K.; Warchola, T.; Snihur, K.; Forbes, T. Z.; Goss, G. G.; Gingras, M. K.; Konhauser K. O.; Alessi, D. S. Characterization and implications of solids associated with hydraulic fracturing flowback and produced water from the Duvernay Formation, Alberta, Canada. *Environ. Sci.: Processes Impacts* **2019**, *21*, 242–255.

(44) Folkerts, E. J.; Blewett, T. A.; Delompré, P.; Mehler, W. T.; Flynn, S. L.; Sun, C.; Zhang, Y.; Martin, J. W.; Alessi, D. S.; Goss, G. G. Toxicity in aquatic model species exposed to a temporal series of three different flowback and produced water samples collected from a horizontal hydraulically fractured well. *Ecotoxicol. Environ. Saf.* **2019**, 180, 600–609.

(45) Zhong, C.; Li, J.; Flynn, S. L.; Nesbø, C. L.; Sun, C.; Von Gunten, K.; Lanoil, B. D.; Goss, G. G.; Martin, J. W.; Alessi, D. S. Temporal changes in microbial community composition and geochemistry in flowback and produced water from the Duvernay formation. *ACS Earth Sp. Chem.* **2019**, *3* (6), 1047–1057.

(46) Katherine N.S. Effects of salinity on the leaching of ionic species from the Duvernay Formation, a Canadian hydraulic fracturing play. M.Sc. Dissertation, University of Alberta, Edmonton, AB, 2020.

(47) Druckenmiller, M. L.; Maroto-Valer, M. M. Carbon sequestration using brine of adjusted pH to form mineral carbonates. *Fuel Process. Technol.* **2005**, *86* (14–15), 1599–1614.

(48) Power, I. M.; Harrison, A. L.; Dipple, G. M.; Wilson, S. A.; Kelemen, P. B.; Hitch, M.; Southam, G. Carbon Mineralization: From Natural Analogues to Engineered Systems. *Rev. Mineral. Geochemistry* **2013**, *77* (1), 305–360. https://doi.org/10.2138/rmg.2013.77.9.

(49) Hamilton J. L.; Wilson S. A.; Morgan B.; Turvey C. C.; Paterson D. J.; MacRae C.; McCutcheon J.; Southam G. Nesquehonite sequesters transition metals and CO_2 during accelerated carbon mineralisation. *Int. J. Greenhouse Gas Control* **2016,** *55*, 73–81

(50) Hamilton, J. L.; Wilson, S. A.; Morgan, B.; Turvey, C. C.; Paterson, D. J.; Jowitt, S. M.; McCutcheon, J.; Southam, G. Fate of transition metals during passive carbonation of ultramafic mine tailings via air capture with potential for metal resource recovery. *Int. J. Greenhouse Gas Control* **2018**, *71*, 155–167.

(51) Reeder R. J.; Lamble G. M.; Northrrup P. A. XAFS study of the coordination and local relaxation around Co^{2+}, Zn^{2+}, Pb^{2+}, and Ba^{2+} trace elements in calcite. *Am. Mineral.* **1999**, *84*, 1049–1060.

(52) Flynn, S.L.; von Gunten, K.; Warchola, T.; Snihur, K.; Forbes, T. Z.; Goss, G. G.; Gingras, M. K.; Konhauser K. O.; Alessi, D. S. Characterization and implications of solids associated with hydraulic fracturing flowback and produced water from the Duvernay Formation, Alberta, Canada. *Environ. Sci.: Processes Impacts* **2019**, *21*, 242–255.

(53) Manceau, A.; Schlegel, M. L.; Musso, M.; Sole, V. A.; Gauthier, C.; Petit, P. E.; Trolard, F. Crystal chemistry of trace elements in natural and synthetic goethite. *Geochim. Cosmochim. Acta* **2000**, *64* (21), 3643–3661.

(54) Trolard, F.; Bourrie, G.; Jeanroy, E.; Herbillon, A. J.; Martin, H. Trace metals in natural iron oxides from laterites: A study using selective kinetic extraction. *Geochim. Cosmochim. Acta* **1995**, *59* (7), 1285–1297.

(55) Canadian Council of Ministers of the Environment: https://ccme.ca/en/current-activities/canadian-environmental-quality-guidelines.

(56) Pingitore, N. E.; Lytle, F. W.; Davies, B. M.; Eastman, M. P.; Eller, P. G.; Larson, E. M. Mode of incorporation of Sr^{2+} in calcite: Determination by X-ray absorption spectroscopy. *Geochim. Cosmochim. Acta* **1992**, *56* (4), 1531–1538.

(57) Parkman, R. H.; Charnock, J. M.; Livens, F. R.; Vaughan, D. J. A study of the interaction of strontium ions in aqueous solution with the surfaces of calcite and kaolinite. *Geochim. Cosmochim. Acta* **1998**, *62* (9), 1481–1492.

(58) Mavromatis, V.; Montouillout, V.; Noireaux, J.; Gaillardet, J.; Schott, J. Characterization of boron incorporation and speciation in calcite and aragonite from co-precipitation

experiments under controlled pH, temperature, and precipitation rate. *Geochim. Cosmochim. Acta* 2**015**, *150*, 299–313.

(59) Kobayashi, K.; Hashimoto, Y.; Wang, S. L. Boron incorporation into precipitated calcium carbonates affected by aqueous pH and boron concentration. *J. Hazard. Mater.* **2020**, *383*, 121183.

(60) Hövelmann, J.; Putnis, C. V.; Ruiz-Agudo, E.; Austrheim, H. Direct nanoscale observations of CO_2 sequestration during brucite [$Mg(OH)_2$] dissolution. *Environ. Sci. Technol.* **2012**, *46* (9), 5253–5260.

(61) Zhao, L.; Sang, L.; Chen, J.; Ji, J.; Teng, H. H. Aqueous carbonation of natural brucite: Relevance to CO_2 sequestration. *Environ. Sci. Technol.* **2010**, *44*, 406−411.

(62) Harrison, A. L.; Dipple, G. M.; Power, I. M.; Mayer, K. U. Influence of surface passivation and water content on mineral reactions in unsaturated porous media: Implications for brucite carbonation and CO_2 sequestration. *Geochim. Cosmochim. Acta* **2015**, *148*, 477–495.

(63) Lester, Y.; Ferrer, I.; Thurman, E. M.; Sitterley, K. A.; Korak, J. A.; Aiken, G.; Linden, K. G. Characterization of hydraulic fracturing flowback water in Colorado: implications for water treatment. *Sci. Total Environ.* **2015**, *512–513*, 637–644

(64) Alessi, D.; Zolfaghari, A.; Kletke, S.; Gehman, J.; Allen, D.M.; Goss, G. G. Comparative analysis of hydraulic fracturing wastewater practices in unconventional shale development: water sourcing, treatment, and disposal practices. *Can. Water Resour. J.* **2017**, *42* (2), 105-121.

(65) Stringfellow, W. T.; Domen, J. K.; Camarillo, M. K.; Sandelin, W. L.; Borglin, S. Physical, chemical, and biological characteristics of compounds used in hydraulic fracturing. *J. Hazard. Mater*. **2014**, *275*, 37–54.

(66) Folkerts, E. J.; Heuer, R. M.; Flynn, S.; Stieglitz, J. D.; Benetti, D. D.; Alessi, D. S.; Goss, G. G.; Grosell, M. Exposure to hydraulic fracturing flowback water impairs mahi-mahi (Coryphaena Hippurus) cardiomyocyte contractile function and swimming performance. *Environ. Sci. Technol.* **2020**, *54*, 13579-13589.

(67) Weinrauch, A. M.; Folkerts, E. J.; Alessi, D. S.; Goss, G. G.; Blewett, T. A. Changes to hepatic nutrient dynamics and energetics in Rainbow Trout (Oncorhynchus Mykiss) following exposure to and recovery from hydraulic fracturing flowback and produced water. *Sci. Total Environ.* **2021**, *764*, 142893. https://doi.org/10.1016/j.scitotenv.2020.142893.

(68) He, Y., Flynn, S. L., Folkerts, E., Zhang, Y., Ruan, D., Alessi, D. S., Martin, J. W., Goss, G. G. Chemical and toxicological characterizations of hydraulic fracturing flowback and produced water. *Water Res.* **2017**, *114*, 78-87

(69) Ziemkiewicz, P. F.; Thomas He, Y. Evolution of water chemistry during Marcellus shale gas development: A case study in west Virginia. *Chemosphere* **2015**, *134*, 224–231.

(70) Rostron, B. J.; Kelley, L. I.; Kreis, L. K.; Holmden, C. *Economic potential of formation brines: Interim results from the Saskatchewan brine sampling program*; Summary of investigations for Saskatchewan Geological Survey: 2002.

(71) Guidelines for Canadian Drinking Water Quality -Summary Table: https://www.canada.ca/en/health-canada/services/environmental-workplace-health/reports-publications/water-quality/guidelines-canadian-drinking-water-quality-summary-table.html (Accessed November 16, 2020).

(72) Zhong, C., Zolfaghari, A., Hou, D., Goss, G. G., Lanoil, B. D., Gehman, J., Tsang, D. C. W., He, Y., Alessi, D. S. Comparison of the hydraulic fracturing water cycle in China and

North America: A critical review. *Environ. Sci. Technol.* **2021** In press. DOI: 10.1021/acs.est.0c06119

(73) Bish, D. L; Howard, S. A. Quantitative phase analysis using the Rietveld method. *J. of Ap. Cry.* **1988**, *21*, 86–91.

(74) Hill, R. J.; Howard, C. J. Quantitative phase analysis from neutron powder diffraction data using the Rietveld method. *J. of Ap. Cry.* **1987**, *20*, 467–474.

(75) Rietveld, H.M.; A profile refinement method for nuclear and magnetic structures. *J. of Ap. Cry.* **1969**, *2*, 65–71.

(76) Parkhurst, D. L.; Appelo, C. A. J. *Description of input and examples for PHREEQC Version 3—A computer program for speciation, batch-reaction, one-dimensional transport, and inverse geochemical calculations*; U.S. Geological Survey: Denver, Colorado, 2013.

(77) Haase, C.; Dethlefsen, F.; Ebert, M.; Dahmke, A. Uncertainty in geochemical modelling of CO_2 and calcite dissolution in NaCl solutions due to different modelling codes and thermodynamic databases. *Appl. Geochemistry* **2013**, *33*, 306–317.

(78) McCutcheon, J.; Wilson, S. A.; Southam, G. Microbially accelerated carbonate mineral precipitation as a strategy for in situ carbon sequestration and rehabilitation of asbestos mine sites. *Environ. Sci. Technol.* **2016**, *50* (3), 1419–1427.

(79) Power, I. M.; Kenward, P. A.; Dipple, G. M.; Raudsepp, M. Room temperature magnesite precipitation. *Cryst. Growth Des.* **2017**, *17* (11), 5652–5659.

(80) Saldi, G. D.; Jordan, G.; Schott, J.; Oelkers, E. H. Magnesite growth rates as a function of temperature and saturation state. *Geochim. Cosmochim. Acta* **2009**, *73* (19), 5646–5657.

(81) De Choudens-Sánchez, V.; Gonzalez, L. A. Calcite and aragonite precipitation under controlled instantaneous supersaturation: elucidating the role of $CaCO_3$ saturation state and Mg/Ca ratio on calcium carbonate polymorphism. *J. Sediment. Res.* **2009**, *79* (6), 363–376.

(82) *World energy outlook 2018*; IEA: Paris, 2018; https://www.iea.org/reports/world-energy-outlook-2018/oil-and-gas-innovation?language=zh#abstract.

(83) Energy and Greenhouse Gas Emissions (GHGs); https://www.nrcan.gc.ca/science-data/data-analysis/energy-data-analysis/energy-facts/energy-and-greenhouse-gas-emissions-ghgs/20063 (Accessed October 15, 2020).

(84) *Global Status of CCS 2019: Targeting climate change*; Global CCS Institute; https://www.globalccsinstitute.com/wpcontent/uploads/2019/12/GCC_GLOBAL_STATUS_REPORT_2019.pdf

(85) Friedlingstein, P.; Jones, M. W.; O'Sullivan, M.; Andrew, R. M.; Hauck, J.; Peters, G. P.; Peters, W.; Pongratz, J.; Sitch, S.; Le Quéré, C.; et al. Global carbon budget 2019. *Earth Syst. Sci. Data* **2019**, *11* (4), 1783–1838.

(86) Sanz-Pérez, E. S.; Murdock, C. R.; Didas, S. A.; Jones, C. W. Direct capture of CO_2 from ambient air. *Chem. Rev.* **2016**, *116* (19), 11840–11876.

(87) Kelemen, P. B.; McQueen, N.; Wilcox, J.; Renforth, P.; Dipple, G.; Vankeuren, A. P. Engineered carbon mineralization in ultramafic rocks for CO_2 removal from air: review and new insights. *Chem. Geol.* **2020**, *550*, 119628.

(88) McQueen, N.; Kelemen, P.; Dipple, G.; Renforth, P.; Wilcox, J. Ambient weathering of magnesium oxide for CO_2 removal from air. *Nat. Commun.* **2020**, *11* (1), 1–10.

(89) Snæbjörnsdóttir, S. Ó.; Sigfússon, B.; Marieni, C.; Goldberg, D.; Gislason, S. R.; Oelkers, E. H. Carbon dioxide storage through mineral carbonation. *Nat. Rev. Earth Environ.* **2020**, *1* (2), 90–102.

(90) Kondash, A. J.; Albright, E.; Vengosh, A. Quantity of flowback and produced waters from unconventional oil and gas exploration. *Sci. Total Environ*. **2017**, *574*, 314–321.

(91) *Water use for oil and gas activity: 2013 annual report*; BC Oil & Gas Commission; 2013; https://www.bcogc.ca/node/11263/download.

(92) *Building capacity to build trust: Key challenges for water governance in relation to hydraulic fracturing*; Canadian Water Network: Waterloo, ON, 2015; https://cwn-rce.ca/wp-content/uploads/2015/10/Moore-et-al-2015-CWN-Report-Water-Governance-and-Hydraulic-Fracturing.pdf.

(93) *2015 water and hydraulic fracturing report*; Canadian Water Network: Waterloo, ON, 2015; https://cwn-rce.ca/wp-content/uploads/2015/10/CWN-2015-Water-and-Hydraulic-Fracturing-Report.pdf.

(94) Zolfaghari, A. University of Alberta, Edmonton. Personal communication, June 2021.

(95) Kondash, A.; Vengosh, A. Water footprint of hydraulic fracturing. *Environ. Sci. Technol. Lett.* **2015**, *2* (10), 276–280.

(96) Qin, Y.; Edwards, R.; Tong, F.; Mauzerall, D. L. Can switching from coal to shale gas bring net carbon reductions to China? *Environ. Sci. Technol.* **2017**, *51* (5), 2554–2562.

(97) Liu, Q.; Lei, Q.; Xu, H.; Yuan, J. China's energy revolution strategy into 2030. *Resour. Conserv. Recycl.* **2018**, *128*, 78–89.

(98) Zou, C.; Ni, Y.; Li, J.; Kondash, A.; Coyte, R.; Lauer, N.; Cui, H.; Liao, F.; Vengosh, A. the water footprint of hydraulic fracturing in Sichuan Basin, China. *Sci. Total Environ.* **2018**, *630*, 349–356.

(99) Government of Canada Website; https://www.canada.ca/en/environment-climate-change/services/climate-change/pricing-pollution-how-it-will-work/industry/pricing-carbon-pollution.html.

(100) *Direct air capture*; IEA: Paris, 2020; https://www.iea.org/reports/direct-air-capture.

(101) Keith, D. W., Holmes, G., St. Angelo, D.; Heidel, K. A process for capturing CO_2 from the atmosphere. *Joule* **2018**, *2*, 1573–1594.

(102) Manovic, V.; Anthony, E. J. Integration of calcium and chemical looping combustion using composite CaO/CuO-based materials. *Environ. Sci. Technol.* **2011**, *45* (24), 10750–10756.

(103) Fan, Y.; Yao, J. G.; Zhang, Z.; Sceats, M.; Zhuo, Y.; Li, L.; Maitland, G. C.; Fennell, P. S. Pressurized calcium looping in the presence of steam in a spout-fluidized-bed reactor with DFT analysis. *Fuel Process. Technol.* **2018**, *169*, 24–41.

(104) Tuan, V. A.; Lee, C. H. Preparation of rod-like MgO by simple precipitation method for CO_2 capture at ambient temperature. *Vietnam J. Chem.* **2018**, *56* (2), 197–202.

(105) Siriwardane, R. V.; Stevens, R. W. Novel regenerable magnesium hydroxide sorbents for CO_2 capture at warm gas temperatures. *Ind. Eng. Chem. Res.* **2009**, *48* (4), 2135–2141.

(106) Hwang, B. W.; Lim, J. H.; Chae, H. J.; Ryu, H. J.; Lee, D.; Lee, J. B.; Kim, H.; Lee, S. C.; Kim, J. C. CO_2 capture and regeneration properties of MgO-based sorbents promoted with alkali metal nitrates at high pressure for the sorption enhanced water gas shift process. *Process Saf. Environ. Prot.* **2018**, *116*, 219–227.

(107) Jin, S.; Ko, K. J.; Lee, C. H. Direct formation of hierarchically porous MgO-based sorbent bead for enhanced CO_2 capture at intermediate temperatures. *Chem. Eng. J.* **2019**, *371*, 64–77.

(108) *Summary of input on oil and gas extraction wastewater management practices under the clean water act*; EPA-821-S19-001; U.S. Environmental Protection Agency: Washington, DC, 2020; https://www.epa.gov/sites/production/files/2020-05/documents/oil-gas-final-report-2020.pdf.

(109) Seifritz, W. CO_2 disposal by means of silicates. *Nature* **1990***, 345*, 486–490.

(110) Kump, L. R.; Brantley, S. L.; Arthur, M. A. Chemical weathering, atmospheric CO_2 and climate. *Annu. Rev. Earth Planet. Sci.* **2000**, *28*, 611–667.

(111) Wilson, S. A.; Harrison, A. L.; Dipple, G. M.; Power, I. M.; Barker, S. L. L.; Ulrich Mayer, K.; Fallon, S. J.; Raudsepp, M.; Southam, G. Offsetting of CO_2 emissions by air capture in mine tailings at the Mount Keith Nickel Mine, Western Australia: rates, controls, and prospects for carbon neutral mining. *Int. J. Greenh. Gas Control* **2014**, *25*, 121–140. https://doi.org/10.1016/j.ijggc.2014.04.002.

(112) Snæbjörnsdóttir, S. Ó., Gislason, S. R., Galeczka, I. M. & Oelkers, E. H. Reaction path modelling of in-situ mineralisation of CO_2 at the CarbFix site at Hellisheidi, SW-Iceland. *Geochim. Cosmochim. Acta* **220**, 348–366 (2018).

(113) Kelemen, P. B. & Matter, J. M. In situ carbonation of peridotite for CO_2 storage. *Proc. Natl Acad. Sci. USA* **105**, 17295–17300 (2008).

(114) Goldberg, D. et al. Geological storage of CO2 in sub-seafloor basalt: the CarbonSAFE pre-feasibility study offshore Washington State and British Columbia. *Energy Procedia* **146**, 158–165 (2018).

(115) McGrail, B. P. et al. Wallula Basalt Pilot demonstration project: post-injection results and conclusions. *Energy Procedia* **114**, 5783–5790 (2017).

(116) *Rock Solid: Harnessing Mineralization for Large-Scale Carbon Management*; Energy Future Initiative: Washington, DC, 2020; https://www.ourenergypolicy.org/resources/rock-solid-harnessing-mineralization-for-large-scale-carbon-management/.

(117) Pogge von Strandmann, P. A. E.; Burton, K. W.; Snæbjörnsdóttir, S. O.; Sigfússon, B.; Aradóttir, E. S.; Gunnarsson, I.; Alfredsson, H. A.; Mesfin, K. G.; Oelkers, E. H.; Gislason, S. R. Rapid CO_2 mineralisation into calcite at the carbfix storage site quantified using calcium isotopes. *Nat. Commun.* **2019**, *10* (1), 1–7. https://doi.org/10.1038/s41467-019-10003-8.

(118) Gíslason, S. R.; Aradottir, E. S.; Sigfusson, B.; Gunnarsson, I.; Alfredsson, H. A.; Wolff-boenisch, D.; Mesfin, K.; Dideriksen, K.; Broecker, W. S. Carbon dioxide emissions. **2016**, *352* (6291), 10–13.

(119) Gunnarsson, I.; Aradóttir, E. S.; Oelkers, E. H.; Clark, D. E.; Arnarson, M. Þ.; Sigfússon, B.; Snæbjörnsdóttir, S.; Matter, J. M.; Stute, M.; Júlíusson, B. M.; Gíslason, S. R. The rapid and cost-effective capture and subsurface mineral storage of carbon and sulfur at the CarbFix2 Site. *Int. J. Greenh. Gas Control* **2018**, *79* (August), 117–126. https://doi.org/10.1016/j.ijggc.2018.08.014.

(120) Gíslason, S. R.; Sigurdardóttir, H.; Aradóttir, E. S.; Oelkers, E. H. A brief history of CarbFix: challenges and victories of the project's pilot phase. *Energy Procedia* **2018**, *146*, 103–114. https://doi.org/10.1016/j.egypro.2018.07.014.

(121) Snæbjörnsdóttir, S.; Oelkers, E. H.; Mesfin, K.; Aradóttir, E. S.; Dideriksen, K.; Gunnarsson, I.; Gunnlaugsson, E.; Matter, J. M.; Stute, M.; Gislason, S. R. The chemistry and saturation states of subsurface fluids during the i*n situ* mineralisation of CO_2 and H_2S at

the CarbFix site in SW-Iceland. *Int. J. Greenh. Gas Control* **2017**, *58*, 87–102. https://doi.org/10.1016/j.ijggc.2017.01.007.

(122) Xue, Z.; Mito, S.; Kitamura, K.; Matsuoka, T. Case study: trapping mechanisms at the pilot-scale CO_2 injection site, Nagaoka, Japan. *Energy Procedia* **2009**, *1* (1), 2057–2062. https://doi.org/10.1016/j.egypro.2009.01.268.

(123) McGrail, B. P.; Spane, F. A.; Sullivan, E. C.; Bacon, D. H.; Hund, G. The Wallula basalt sequestration pilot project. *Energy Procedia* **2011**, *4*, 5653–5660. https://doi.org/10.1016/j.egypro.2011.02.557.

(124) McGrail, B. P.; Schaef, H. T.; Spane, F. A.; Horner, J. A.; Owen, A. T.; Cliff, J. B.; Qafoku, O.; Thompson, C. J.; Sullivan, E. C. Wallula basalt pilot demonstration project: post-injection results and conclusions. *Energy Procedia* **2017**, *114* (November 2016), 5783–5790. https://doi.org/10.1016/j.egypro.2017.03.1716.

(125) White, S. K.; Spane, F. A.; Schaef, H. T.; Miller, Q. R. S.; White, M. D.; Horner, J. A.; McGrail, B. P. Quantification of CO_2 mineralization at the Wallula Basalt pilot project. *Environ. Sci. Technol.* **2020**, *54* (22), 14609–14616. https://doi.org/10.1021/acs.est.0c05142.

(126) Mervine, E. M.; Wilson, S. A.; Power, I. M.; Dipple, G. M.; Turvey, C. C.; Hamilton, J. L.; Vanderzee, S.; Raudsepp, M.; Southam, C.; Matter, J. M.; Kelemen, P. B.; Stiefenhofer, J.; Miya, Z.; Southam, G. Potential for offsetting diamond mine carbon emissions through mineral carbonation of processed kimberlite: an assessment of De Beers mine sites in South Africa and Canada. *Mineral. Petrol.* **2018**, *112*, 755–765. https://doi.org/10.1007/s00710-018-0589-4.

(127) Service, R. F. The carbon vault. *Science.* **2020**, *369* (6508), 1156–1159. https://doi.org/10.1126/SCIENCE.369.6508.1156.

(128) Paulo, C., Power, I.M., Stubbs, A.R., Wang, B., Zeyen, N., and Wilson, S.A. Evaluating feedstocks for carbon dioxide removal by enhanced rock weathering and CO_2 mineralization. *Appl. Geochem.* **2021**, in press. https://www.doi.org/10.1016/j.apgeochem.2021.104955

(129) Stubbs, A.R., Paulo, C., Power, I.M., Wang, B., Zeyen, N., and Wilson, S.A. (2021) Direct measurement of CO_2 drawdown in mine residues: implications for enhanced rock weathering as a negative emission technology. International Journal of Greenhouse Gas Control, in review as of 18 July 2021.

(130) Project Vesta website: https://www.projectvesta.org/

(131) Heirloom website: https://www.heirloomcarbon.com/

(132) 44.01 website: https://4401.earth/

(133) Zhu, B.; Wilson, S.A.; Zeyen, N.; Raudsepp, M.J.; Wang, B.; Rostron, B.J.; Snihur, K.N.; von Guten, K.; Harrison, A.L.; Alessi, D.S. Hydraulic fracturing flowback and produced water as a feedstock for carbon dioxide removal or emissions reduction via mineral carbonation. *In preparation*.

(134) Ho, H.-J.; Iizuka, A.; Shibata, E. Carbon capture and utilization technology without carbon dioxide purification and pressurization: a review on its necessity and available technologies. *Ind. Eng. Chem. Res.* **2019**, *58*, 8941−8954.

(135) McQueen, N.; Gomes, K. V.; McCormick, C.; Blumanthal, K.; Pisciotta, M.; Wilcox, J. A Review of Direct Air Capture (DAC): Scaling up Commercial Technologies and Innovating for the Future. *Prog. Energy* **2021**, *3* (3), 032001.

(136) Ho, H. J.; Iizuka, A.; Shibata, E.; Tomita, H.; Takano, K.; Endo, T. CO2 utilization via direct aqueous carbonation of synthesized concrete fines under atmospheric pressure. ACS Omega 2020, 5, 15877–15890. https://doi.org/10.1021/acsomega.0c00985.

(137) Jo, H. Y.; Kim, J. H.; Lee, Y. J.; Lee, M.; Choh, S. J. Evaluation of factors affecting mineral carbonation of CO2 using coal fly ash in aqueous solutions under ambient conditions. Chem. Eng. J. 2012, 183, 77–87. https://doi.org/10.1016/j.cej.2011.12.023.

(138) Beinlich, A.; Austrheim, H. In Situ sequestration of atmospheric CO_2 at low temperature and surface cracking of serpentinized peridotite in mine shafts. *Chem. Geol.* **2012**, *332–333*, 32–44. https://doi.org/10.1016/j.chemgeo.2012.09.015.

(139) Oskierski, H. C.; Dlugogorski, B. Z.; Jacobsen, G. Sequestration of atmospheric CO_2 in chrysotile mine tailings of the Woodsreef asbestos Mine, Australia: quantitative mineralogy, isotopic fingerprinting and carbonation rates. *Chem. Geol.* **2013**, *358*, 156–169. https://doi.org/10.1016/j.chemgeo.2013.09.001.

(140) Botha, A.; Strydom, C. A. Preparation of a magnesium hydroxy carbonate from magnesium hydroxide. *Hydrometallurgy* **2001**, *62*, 175–183.

(141) Xiong, Y.; Lord, A. S. Experimental investigations of the reaction path in the MgO-CO_2-H_2O system in solutions with various ionic strengths, and their applications to nuclear waste isolation. *Appl. Geochem.* **2008**, *23*, 1634–1659.

(142) Pronost, J.; Beaudoin, G.; Tremblay, J.; Larachi, F.; Duchesne, J.; Hébert, R.; Constantin, M. Carbon sequestration kinetic and storage capacity of ultramafic mining waste. *Environ. Sci. Technol.* **2011**, *45*, 9413–9420. https://doi.org/10.1021/es203063a.

(143) Zeyen, N.; Benzerara, K.; Li, J.; Groleau, A.; Balan, E.; Robert, J. L.; Estève, I.; Tavera, R.; Moreira, D.; López-García, P. Formation of low-T hydrated silicates in modern microbialites from Mexico and implications for microbial fossilization. *Front. Earth Sci.* **2015**, *3*, 1–23. https://doi.org/10.3389/feart.2015.00064.

(144) Tosca, N. J.; Macdonald, F. A.; Strauss, J. V.; Johnston, D. T.; Knoll, A. H. Sedimentary talc in neoproterozoic carbonate successions. *Earth Planet. Sci. Lett.* **2011**, *306*, 11–22. https://doi.org/10.1016/j.epsl.2011.03.041.

(145) Tosca, N. J.; Masterson, A. L. Chemical controls on incipient Mg-silicate crystallization at 25°C: implications for early and late diagenesis. *Clay Miner.* **2014**, *49*, 165–194. https://doi.org/10.1180/claymin.2014.049.2.03.

(146) Oelkers, E. H.; Butcher, R.; Pogge von Strandmann, P. A. E.; Schuessler, J. A.; von Blanckenburg, F.; Snæbjörnsdóttir, S.; Mesfin, K.; Aradóttir, E. S.; Gunnarsson, I.; Sigfússon, B.; Gunnlaugsson, E.; Matter, J. M.; Stute, M.; Gislason, S. R. Using stable Mg isotope signatures to assess the fate of magnesium during the in situ mineralisation of CO_2 and H_2S at the CarbFix site in SW-Iceland. *Geochim. Cosmochim. Acta* **2019**, *245*, 542–555. https://doi.org/10.1016/j.gca.2018.11.011.

(147) Clark, I. D.; Fontes, J. C.; Fritz, P. Stable isotope disequilibria in travertine from high pH waters: laboratory investigations and field observations from Oman. *Geochim. Cosmochim. Acta* **1992**, *56*, 2041–2050. https://doi.org/10.1016/0016-7037(92)90328-G.

(148) Sade, Z.; Yam, R.; Shemesh, A.; Halevy, I. Kinetic Fractionation of carbon and oxygen isotopes during $BaCO_3$ precipitation. *Geochim. Cosmochim. Acta* **2020**, *280*, 395–422.

(149) Yan, H.; Liu, Z.; Sun, H. Large Degrees of Carbon Isotope Disequilibrium during precipitation-associated degassing of CO_2 in a mountain stream. *Geochim. Cosmochim. Acta* **2020**, *273*, 244–256. https://doi.org/10.1016/j.gca.2020.01.012.

(150) Deines, P.; Langmuir, D.; Harmon, R. S. Stable carbon isotope ratios and the existence of a gas phase in the evolution of carbonate ground waters. *Geochim. Cosmochim. Acta* **1974**, *38*, 1147–1164.

(151) Turner, J. V. Kinetic fractionation of carbon-13 during calcium carbonate precipitation. *Geochim. Cosmochim. Acta* **1982**, *46*, 1183–1191. https://doi.org/10.1016/0016-7037(82)90004-7.

(152) Deirmendjian, L.; Abril, G. Carbon dioxide degassing at the groundwater-stream-atmosphere interface: isotopic equilibration and hydrological mass balance in a sandy watershed. *J. Hydrol.* **2018**, *558*, 129–143. https://doi.org/10.1016/j.jhydrol.2018.01.003.

(153) Polsenaere, P.; Abril, G. Modelling CO_2 degassing from small acidic rivers using water pCO_2, DIC and $\delta^{13}C$-DIC data. *Geochim. Cosmochim. Acta* **2012**, *91*, 220–239. https://doi.org/10.1016/j.gca.2012.05.030.

(154) Johnson, M. S.; Lehmann, J.; Riha, S. J.; Krusche, A. V.; Richey, J. E.; Ometto, J. P. H. B.; Couto, E. G. CO_2 efflux from amazonian headwater streams represents a significant fate for deep soil respiration. *Geophys. Res. Lett.* **2008**, *35*, 1–5. https://doi.org/10.1029/2008GL034619.

(155) Dawson, J. J. C.; Hope, D.; Cresser, M. S.; Billett, M. F. Downstream changes in free carbon dioxide in an upland catchment from northeastern Scotland. *J. Environ. Qual.* **1995**, *24*, 699–706. https://doi.org/10.2134/jeq1995.00472425002400040022x.

(156) Davidson, E. A.; Figueiredo, R. O.; Markewitz, D.; Aufdenkampe, A. K. Dissolved CO_2 in small catchment streams of eastern Amazonia: a minor pathway of terrestrial carbon loss. *J. Geophys. Res. Biogeosciences* **2010**, *115*, 1–6. https://doi.org/10.1029/2009JG001202.

(157) Mook, W. G.; Bommerson, J. C.; Staverman, W. H. Carbon isotope fractionation between dissolved bicarbonate and gaseous carbon dioxide. *Earth Planet. Sci. Lett.* **1974**, *22*, 169–176.

(158) Assima, G. P.; Larachi, F.; Beaudoin, G.; Molson, J. CO_2 sequestration in chrysotile mining residues—implication of watering and passivation under environmental conditions. *Ind. Eng. Chem. Res.* **2012**, *51*(26), 8726–8734.

(159) Hamilton, J. L., Wilson, S. A., Morgan, B., Harrison, A. L., Turvey, C. C., Paterson, D. J., Dipple, G. M., and Southam, G. Accelerating mineral carbonation in ultramafic mine tailings via direct CO_2 reaction and heap leaching with potential for base metal enrichment and recovery. *Econ. Geol.* **2020**, *115*, 303–232.

(160) Bang, J. H.; Jang, Y. N.; Kim, W.; Song, K. S.; Jeon, C. W.; Chae, S. C.; Lee, S. W.; Park, S. J.; Lee, M. G. Precipitation of calcium carbonate by carbon dioxide microbubbles. *Chem. Eng. J.* **2011**, *174*, 413–420. https://doi.org/10.1016/j.cej.2011.09.021.

(161) Kelemen, P. B.; McQueen, N.; Wilcox, J.; Renforth, P.; Dipple, G.; Vankeuren, A. P. Engineered Carbon Mineralization in Ultramafic Rocks for CO_2 Removal from Air: Review and New Insights. *Chem. Geol.* **2020**, *550*, 119628. https://doi.org/10.1016/j.chemgeo.2020.119628.

(162) Zhang, N.; Santos, R. M.; Šiller, L. CO_2 Mineralisation of Brines with Regenerative Hydrotalcites in a Cyclical Process. *Chem. Eng. J.* **2021**, *404*, 126450.

APPENDIX A

Supplementary Information for CHAPTER 2:

Hydraulic fracturing flowback and produced water as a feedstock for carbon dioxide removal or emissions reduction via mineral carbonation

A1 Materials

FPW1a and FPW1b were collected December 19, 2016, 324 h after well simulation. FPW2 was collected December 6, 2016, 16 h after well stimulation. FPW1a and FPW1b are subsamples of FPW1 (a 32 L drum of stratified brine) that were collected separately to assess heterogeneity within the sample. The proportion of injected water, chemical additives, and formation water in the flowback fluids at different stage are reviewed in Stringfellow et al. (2014)[1] and He et al. (2017)[2]. Flowback samples (FPW1a, FPW1b, and FPW2) were stored in polypropylene buckets, and the samples were stratified into organics on the top layer, red suspended solids in the intermediate layer, and aqueous components on the bottom layer. FPW samples were collected from the bottom layer with Stripette. As we only interested in utilizing the dissolved inorganic components of the brines in this study, samples were placed to stagnation prior to sampling. FPW1a and FPW1b were collected for separate batch, and the heterogeneity of them will be discussed.

TABLE A-1. Information of the brine samples in this study.

Sample ID	Formation	Collection time (after well simulation)	Total dissolved solid (ppm)	Specific gravity	Total organic carbon (ppm)	Titration pH
FPW 1a	Duvernay Formation, Alberta	324 h	188,000*	1.13	143.8	pH 8.5-12 (n=8, in increments of 0.5)
FPW 1b						pH 8.5-12 (n=8, in increments of 0.5)
FPW 2		16 h	153,000*	1.10	506.0	pH 8.5-12 (n=8, in increments of 0.5)
PW	Red River Formation, Saskatchewan	N/A	299,523º	1.19	N/A	pH 8.5-12 (n=8, in increments of 0.5)

º Data from Rostron et al. (2002)[3]. Detailed sample information can refer to Sample U of A 01- 159B in this paper.
* Analyzed through evaporation method.

A2 Methods

A2.1 Titration Experiment Procedures

Experiments were conducted in series: samples of FPW1a and PW were titrated in one batch and samples of FPW1b and FPW2 were treated in a second batch of experiments. The samples of FPW2 and FPW1b are duplicated at each pH endpoint while FPW1a and PW did not due to the limited supplies of PW. FPW1a and FPW1b were collected at different batch from same drum and have slightly variations in solution chemistry. Each titration was ended when the measured pH reached a value within 0.03 units of the targeted value. Immediately following titration, samples were stirred at 50 rpm and allowed to react for 24 h at 18 ± 2 °C at atmospheric pCO_2, which was 405 (±82) – 470 (±84) ppm in our laboratory over the course of these experiments. Containers were sealed with pierced Parafilm to minimize evaporation while maintaining contact with atmosphere. Stirring was stopped after 24 h and precipitates and supernatants were separated through centrifugation at 7500 rpm for 5 minutes. Prior to centrifugation, samples were weighed before

and after reaction to monitor mass changes due to addition of NaOH, evaporative loss of H_2O, and gain of CO_2. A total of 46 samples were titrated and reacted (Table A-1). Among those samples, precipitates were observed in 34 samples and 33 samples were of sufficiently large mass to be recoverable (Table A-6). The control samples are the original FPW1a, FPW1b, FPW2, and PW that were stirred concurrently with the experimental samples at the same experimental conditions.

Precipitates were washed with ultrapure Milli-Q water (>18.2 MΩ) three times and centrifuged at 7500 rpm for 5 minutes after each rinse and separation. They were then dried in desiccator containing Drierite for 1 week and weighed. Supernatant samples were filtered with 0.22 μm syringe filters and stored in 50 mL polypropylene Falcon tubes at 4 °C prior to analyses. The electrical conductivity (EC) and pH of the initial brines and brines after reaction were measured with a Thermo Scientific Orion Star A215 pH/Conductivity Meter. Both the auto-titrator and pH probe were calibrated with pH 4, 7, and 10 standard solutions, and the conductivity probe was calibrated with 12.88 μS/cm and 1413 μS/cm EC standard solutions. Calibrations were done daily. Relative humidity (RH) fluctuated between 8.0%–17.0% during the experiments; RH values were recorded using a NIST-traceable hygrometer.

A2.2 Scanning Electron Microscopy

An aliquot of titration precipitates was mounted in stub using carbon tape and coated with gold (Au) or carbon (C). Scanning Electron Microscope (SEM) images and Energy-dispersive X-ray spectra of samples are obtained using Zeiss Sigma 300 VP Field Emission Scanning Electron Microscope, equipped with a Bruker energy dispersive X-ray spectroscopy (EDS) system, in the Department of Earth and Atmospheric Sciences Scanning Electron Microscope Laboratory at the

University of Alberta. For SEM images and major element analysis, the operation voltage is 10 kV. For transitional metal analysis, the EDS spectra were obtained with an operation voltage of 15 kV and a measurement time of 5 minutes.

A2.3 Powder X-Ray Diffraction

Powder X-ray diffraction (XRD) patterns of the precipitates and red suspended solid samples are obtained in the X-ray Diffraction Laboratory at the department of Earth and Atmospheric Sciences of the University of Alberta. An aliquot of the precipitates was air-dried at room temperature and hand-ground using an agate mortar and pestle. Samples were front-loaded into zero background plates. Patterns were collected using a Rigaku Ultima IV q–q powder X-ray diffractometer equipped with a D/Tex Ultra detector and a cobalt source that was operated at 38 kV and 38 mA. XRD patterns were collected from 5–80°2q using a step size of 0.02° 2q at a rate of 1.2°2q/minute. Mineral phase identification was conducted using the DIFFRAC.EVA XRD phase analysis software (Bruker) with reference to the International Center for Diffraction Data Powder Diffraction File 4+ database (ICDD PDF4+). Rietveld refinement[4–6] with XRD data were used to determine mineral abundances with TOPAS 5 (Bruker). Fundamental parameters peak fitting[7] was used for all phases. Anisotropic peak broadening of brucite nanoparticles was fitted using the Stephens' model[8]. The phases abundance is semi-quantitative analysis based on the Rietveld refinement of the XRD patterns [4-6], in which R_{wp} is a measure of the quality of the modelled fit to observed XRD patterns. The precipitates at pH 9.5 from FPW1a were only analyzed with SEM and the precipitates at 9.5 from FPW2 were only analyzed with XRD.

A2.4 Inductively Coupled Plasma Mass Spectrometry

The concentration of ions in the brines and precipitates were analyzed with an Agilent 8800 Triple Quadrupole ICP-MS/MS. The brines samples were diluted approximately 910 times for Na and 83 times for other elements using 18 MΩ MilliQ water and then acidified using 12 mL trace metal grade nitric acid per 10 mL sample. The tune mode, scan type and units of the analytes for the brine samples during the ICP-MS analysis are listed in Table A-2. External standard solutions and a blank were matrix match with the brines by adding 100,000 ppm NaCl solutions. The external standards were analyzed every 10 samples at the start, middle, and the end of each run.

The precipitates from titration experiments were reacted with 2.5 mL 37% HCl for 8 hours at room temperature (18 ± 2°C) and then placed in a water-bath at 75 °C for 1h. The remaining samples were then dissolved in aqua regia by adding 0.83 ml of 67% (w/w) trace metal grade HNO_3 and then were heat-activated in water bath at 60°C for 1 hour. The resulting solutions were heated for another 8 hours until approximately 2 mL of solution was left. Prior to the analysis, the samples were diluted to 50 mL with a solution of 2% HCl and 0.5% HNO_3. The analytes, tune mode, scan type and the internal standard of the ICP-MS run for the precipitates are listed in Table A-3. Samples were aspirated with a micromist nebulizer and nickel/copper cones. To account for the instrumental drift, internal standard solutions (Table A-2, A-3) with the concentration of 1 ppm were added to each sample utilizing an inline addition system. The external standards were analyzed every 10 samples at the start, middle, and the end of each run. The analytical errors are given as one standard deviation, calculated from three replicated measurements during ICP-MS analyses. Values are reported as three significant figures.

TABLE A-2. Tune mode, scan type, and internal standard (ISTD) of the analytes in the ICP-MS analysis of the brine samples.

Analyte	Q1	Q2	Tune Mode	Scan Type	ISTD
Li	7	7	No Gas	MS/MS	45 Sc
B	11	11	No Gas	MS/MS	45 Sc
Na	23	23	He	MS/MS	115 In
Mg	24	24	He	MS/MS	45 Sc
Al	27	27	He	MS/MS	45 Sc
Si	28	28	H_2	MS/MS	45 Sc
K	39	39	He	MS/MS	45 Sc
S	32	48	O_2	MS/MS	74 Ge
Cl	35	37	H_2	MS/MS	115 In
Ca	40	40	H_2	MS/MS	45 Sc
Mn	55	55	He	MS/MS	74 Ge
Fe	56	56	He	MS/MS	74 Ge
Co	59	59	He	MS/MS	74 Ge
Ni	60	60	He	MS/MS	74 Ge
Cu	63	63	He	MS/MS	74 Ge
Zn	66	66	He	MS/MS	74 Ge
Br	79	79	He	MS/MS	74 Ge
Sr	88	88	He	MS/MS	74 Ge
Ba	137	137	He	MS/MS	115 In
Pb	208	208	No Gas	MS/MS	209 Bi

TABLE A-3. Tune mode, scan type, and internal standard (ISTD) of the analytes in the ICP-MS analysis of the precipitates.

Analytes	Q1	Q2	Tune Mode	Scan Type	ISTD
Li	7	7	No Gas	MS/MS	45 Sc
B	11	11	No Gas	MS/MS	45 Sc
Mg	24	24	He	MS/MS	45 Sc
Al	27	27	He	MS/MS	45 Sc
Si	28	28	H_2	MS/MS	45 → 45 Sc
P	31	47	O_2	MS/MS	74 Ge
S	32	48	O_2	MS/MS	74 → 88 Ge
Mn	55	55	He	MS/MS	74 Ge
Fe	56	56	H_2	MS/MS	74 → 74 Ge
Co	59	59	He	MS/MS	74 Ge
Ni	60	60	He	MS/MS	74 Ge
Cu	63	63	He	MS/MS	74 Ge
Zn	66	66	H_2	MS/MS	74 Ge
Sr	88	88	He	MS/MS	74 Ge
Cd	111	111	He	MS/MS	115 In
Pb	208	208	No Gas	MS/MS	209 Bi

A2.5 Other Solution Chemistry Analyses

The chloride (Cl^-) concentration in the brines was analyzed with a Dionex DX-6 Ion Chromatography (IC) at the University of Alberta BASL Laboratory. The method was based on EPA method 300.1[9]. The total dissolved solid (TDS) of FPW1a, FPW1b, and FPW2 were analyzed through evaporation method. The relative density of the brine samples and 1M NaOH solution were calculated from the eq (1):

$$RD = m_s/m_{MilliQ} \quad (1)$$

where RD = relative density, m_s = mass of 10 mL sample and m_{MilliQ} = mass of 10 mL MilliQ water. The mass of the 10 mL samples was obtained through pipetting 1000 ul of each solution for

10 times. Prior to analyses, the samples were filtered with 0.22 μm syringe filters. Results of the above analyses are listed in Table A-1.

A2.6 Geochemical Modelling of Titration Experiments

The titration experiments of the brines were modelled with USGS PHREEQC version 3[10]. The models we developed aim to predict the saturation state of minerals in the studied brines at various pH conditions. The modelling with PHREEQC applied phreeqc.dat, which using ion-dissociation method for the calculation of ion activity. Although the pitzer.dat[11] has activity models that target high ionic strength solutions, the modelling of the saline solutions using pitzer.dat do not yield lower uncertainties than using phreeqc.dat.[12] In addition, the more complete thermodynamic database, including aqueous complexes and mineral precipitates, in phreeqc.dat gives more accurate calculations of solution chemistry than pitzer.dat. The geochemical modelling calculates the saturation index (SI) of Ca-carbonates (aragonite, calcite, disordered dolomite), Ca-hydroxides (portlandite), hydrated Mg-carbonates (dypingite, nesquehonite, and hydromagnesite), Mg-carbonate (magnesite) and Mg-hydroxides (brucite). It also calculates the SI of kerolite and manganite, which are observed in the precipitates of the titration experiments. Some thermodynamic data are not included in the phreeqc.dat and were added from wateq4f.dat in the PHREEQC package and other sources (Table A-4). For comparison, modelling was also performed with pitzer.dat, which shows that the pH at which SI = 0 for the above phases are almost identical to the pH (less than 0.25 unit difference) calculated using phreeqc.dat.

TABLE A-4. Solubility product for disordered dolomite, hydromagnesite, kerolite, and dypingite in addition to the pitzer.dat database in this study.

Mineral phase	Equation	T(°C)	log K_{sp}	Source
Brucite	$Mg(OH)_2 + 2H^+ = Mg^{2+} + 2H_2O$		16.84	wateq4f.dat
Disordered dolomite	$CaMg(CO_3)_2 = Ca^{2+} + Mg^{2+} + 2CO_3^{2-}$		-17.09	wateq4f.dat
Dypingite	$Mg_5(CO_3)_4(OH)_2 \cdot 5H_2O = 5Mg^{2+} + 4CO_3^{2-} + 2OH^- + 5H_2O$	25	−34.94 ± 0.58	Harrison et al. (2019)[13]
Hydromagnesite	$Mg_5(CO_3)_4(OH)_2 \cdot 4H_2O + 2H^+ = 5Mg^{2+} + 4CO_3^{2-} + 6H_2O$		−8.762	wateq4f.dat
Kerolite	$Mg_3Si_4O_{10}(OH)_2 \cdot H_2O + 6H^+ = 3Mg^{2+} + 4SiO_2\,(aq) + 5H_20$	25	25.79 ± 0.24	Stoessell (1988)[14]
Magnesite	$MgCO_3 = Mg^{2+} + CO_3^{2-}$		−8.029	wateq4f.dat
Nesquehonite	$MgCO_3 \cdot 3H_2O = Mg^{2+} + CO_3^{2-} + 3H_2O$		−5.621	wateq4f.dat

A3 Results

Water chemistry of brines in titration experiments are summarized in Table A-5 and A-6 and Figure A-1. Characterization of the precipitates yielded from titration experiments involves phase identification (Figure A-2, A-3, A-6), estimation of the phase abundance (Table A-7), crystal morphology (Figure A-4, A-5, A-7–A-9), elemental composition (Figure A-5, A-7–A-9, Table A-8), yield of Ca and Mg in precipitates (Figure A-11). Modelling titration experiment of FPW1a with its original water chemistry (Figure A-10) successfully predict the observed precipitated phases. Table A-9 and A-10 summarize the annual FPW production by countries and estimated annual CO_2 capture by countries, respectively.

The average value of the TDS in FPW1a and FPW1b, which are subsamples of FPW1, are 188,000 ppm. The TDS of FPW2 and PW are 153,000 ppm and 299,523 ppm, respectively. Table A-5 shows the concentrations of 20 analytes. Na, K, and Cl comprise ~95% of the total ions. The concentration of Al in all brine samples are below the detection limit. Elevated concentrations (> ppb–ppm level) of Cu, Fe, Mn, Ni, Pb, and Zn in some FPW and PW samples may be potentially toxic to the aquatic life and soil organisms,[15] but may offer opportunities for the critical metal recovery. The concentrations of the transition metals, Mn, Pb, and Zn, in untreated FPW1a are 4.37 ± 0.07 ppm, 0.107 ± 0.001 ppm, and 0.734 ± 0.031 ppm, respectively. The Mn and Pb concentrations in untreated FPW1b are 4.37 ± 0.10 ppm and 0.191 ± 0.001 ppm, respectively, and the Zn concentration is below the detection limit. The Mn concentration of untreated FPW2 is 1.68 ± 0.05 ppm while the concentrations of Pb and Zn are below the detection limits. Mn, Pb and Zn are present at abundances of 0.195 ± 0.008, 0.0816 ± 0.0006 and 1.05 ± 0.06 ppm, respectively, in the untreated PW. The concentrations of Cu, Fe, and Ni are either below or close to the detection limits.

The EC values of all FPW and PW samples decreased as the pH endpoint values of titration increased with the onset of mineral precipitation (Figure A-1).

TABLE A-5. Ion concentrations (ppm) in the original brines determined using ICP-MS and IC analyses. Analytical uncertainties are given (in brackets). ICPMS and IC are reported as 3 significant figures.

		FPW1a	FPW1b	FPW2	PW
Major	Na	65800 (1500)	48000 (1000)	39500 (400)	91900 (2500)
	Ca	11000 (100)	10800 (290)	8180 (40)	17300 (310)
	Cl	139000*	108000 (4500)	93600 (2500)	194000*
Minor	Br	284 (5)	254 (6)	208 (8)	497(17)
	K	1940 (30)	1860 (50)	1630 (62)	4170 (70)
	Mg	793 (46)	841 (15)	699 (26)	1920 (110)
	Sr	1050 (30)	952 (16)	759 (20)	595 (11)
Trace	Al	<0.0429	4.70 (0.43)	4.71 (0.13)	<0.0384
	B	92.1 (1.8)	80.3 (1.3)	76.1 (0.1)	111 (2)
	Ba	3.20 (0.20)	3.11 (0.11)	3.37 (0.12)	14.9 (0.5)
	Cu	<0.488	<0.275	<0.266	0.0435 (0.0012)
	Fe	0.264 (0.008)	1.74 (0.02)	2.07 (0.06)	0.100 (0.002)
	Li	48.4 (1.0)	32.4 (0.3)	27.3 (0.3)	59.0 (0.6)
	Mn	4.37 (0.07)	4.37 (0.10)	1.68 (0.05)	0.195 (0.008)
	Ni	<0.572	<0.275	<0.266	<0.512
	P	<0.0458	BDL	BDL	<0.0411
	Pb	0.107 (0.001)	0.191 (0.001)	<0.178	0.0816 (0.0006)
	S	87.3 (2.7)	76.9 (2.4)	88.5 (0.3)	85.8 (6.9)
	Si	9.20 (1.10)	225 (6)	190 (3)	3.80 (0.10)
	Zn	0.734 (0.031)	<1.56	<1.51	1.05 (0.06)

*Concentration measured with IC.
†BDL: below sample-specific detection limit.

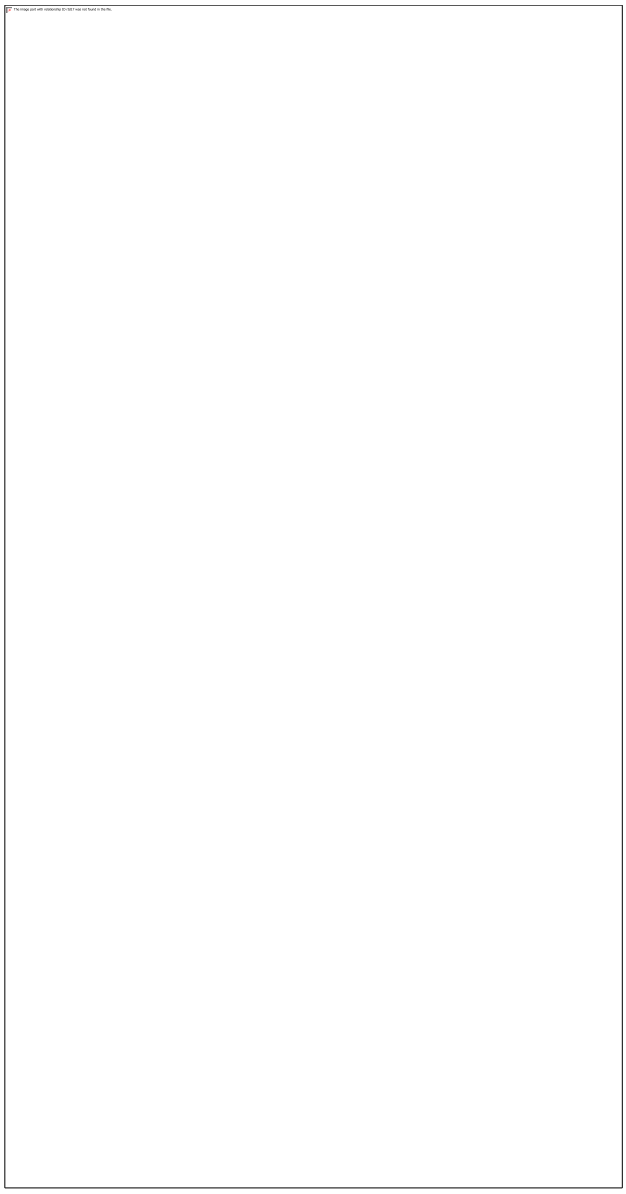

FIGURE A-1. (A) Electrical conductivity, (B) pH after reaction with atmospheric CO_2, and (C) dissolved inorganic carbon plotted versus pH endpoint of titration experiments. Values measured in the untreated brines appear in grey-shaded fields. Generally, precipitates (Ppt.) were observed (shaded in blue) between pH 9.0 and 9.5; calcite (Cal) or aragonite (Arg), brucite (Brc), and Mg-silicate (M-Slc) were identified (shaded in red) in the precipitates between pH ~9.5 and ~10.0. Portlandite (Por) was identified (dark blue dashed line) in the precipitates at pH ~12.0 for FPW1a and PW but was not observed for FPW1b or FPW2.

TABLE A-6. Mg concentrations (ppm) based on ICP-MS and sample-specific detection limits. Column 4 indicates the maximum percentage of total Mg left in solution at 11.5–12.0 (FPW1a), 12.0 (FPW1b), 12.0 (FPW2) and 11.0–12.0 (PW).

Sample	Mg Conc. (ppm)	Detection limit (ppm)	Detection limit/ Mg conc. in original brine
FPW1a pH 11.5	30.4	85.7	10.8%
FPW1a pH 12.0	28.8	87.4	11.0%
FPW1b pH 12.0-1	37.7	89.8	10.7%
FPW1b pH 12.0-2	30.8	88.3	10.5%
FPW2 pH 12.0-1	48.9	84.5	12.1%
FPW2 pH 12.0-2	49.5	85.3	12.2%
PW pH 11.0	62.5	86.9	4.5%
PW pH 11.5	30.2	87.2	4.5%
PW pH 12.0	29.7	90.0	4.7%

The yield, mineralogy, and phase abundance of precipitates from titration experiments are summarized in Table A-7. Calcite is the most abundant phase at pH 10.0 (85.6 wt%), and brucite (74.1–83.1 wt%) is most abundant phase at pH 10.5–11.5 in the precipitates from FPW1a. Portlandite (28.3 wt%) precipitated and calcite (43.5 wt%) became the most abundant phase in FPW1a at pH 12.0. Calcite is the most abundant phase at pH 10.0 and brucite (72.9–80.4 wt%) is the most abundant phase between pH 10.5–12.0 in the precipitates from FPW1b. Overall, hydroxide phases (brucite and portlandite) were the dominant phases in precipitates at pH > 10.5 (FPW1a, FPW1b and FPW2) and pH > 9.5 (PW). Carbonate phases (aragonite and calcite) were present at their highest abundances at pH 9.5–10.0 (FPW1a), 10.0 (FPW1b), 9.5–10.0 (FPW2), when precipitation had just begun. Calcite is the most abundant phase in the precipitates at pH 10.0 whereas brucite was the most abundant phase at pH 10.5–12.0 (54.9–77.6 wt%) in the precipitates from FPW2, except for one duplicate experiment at pH 10.5 which contained 38.9 wt% brucite. Brucite (47.8–97.0 wt%) was the most abundant phase at pH 9.5–12.0 in the precipitates

from PW. Aragonite had its highest abundance at pH 9.5 (29.5 wt%) and became a minor phase at pH 10.0–12.0 (0.3–7.3 wt%). The abundance of calcite (0.1–28.1 wt%) increased as a function of pH in the precipitates from pH 9.5–12.0 in PW. Portlandite (16.8 wt%) precipitated from PW at pH 12.0.

FIGURE A-2. XRD patterns for precipitates from (A) FPW1a and (B) PW. a: aragonite ($CaCO_3$); b: brucite [$Mg(OH)_2$]; c: calcite ($CaCO_3$); and p: portlandite [$Ca(OH)_2$]. The most intense and diagnostic peaks of each phase are labelled at either the pH where they first appeared or when their wt% >10%.

FIGURE A-3. XRD patterns for precipitates from duplicate experiments using (A) FPW2 and (B) FPW1b. Patterns for duplicate experiments are displayed using the same colour. a: aragonite ($CaCO_3$); b: brucite [$Mg(OH)_2$]; c: calcite ($CaCO_3$); and p: portlandite [$Ca(OH)_2$]. The most intense and diagnostic peaks of each phase are labelled at either the pH where they first appeared or when their wt% >10%.

TABLE A-7. Yield of precipitates, mineralogy, and phase abundance following titration experiments.

Sample	pH	Yield (g/L)	Aragonite (wt%)	Brucite (wt%)	Calcite (wt%)	Portlandite (wt%)	Total (wt%)	*R_{wp} (%)
FPW1a	9.5	n/a†			M			
FPW1a	10.0	0.9		14.4	85.6		100.0	4.3
FPW1a	10.5	2.2		81.6	18.4		100.0	4.1
FPW1a	11.0	2.3		83.1	16.9		100.0	4.2
FPW1a	11.5	3.1		74.1	25.9		100.0	5.3
FPW1a	12.0	7.7		28.2	43.5	28.3	100.0	4.7
FPW1b-1	10.0	n/a†			M			
FPW1b-2	10.0	n/a†			M			
FPW1b-1	10.5	2.3		73.6	26.4		100.0	7.7
FPW1b-2	10.5	2.2		79.8	20.2		100.0	5.6
FPW1b-1	11.0	2.9		76.8	23.2		100.0	4.9
FPW1b-2	11.0	2.8		72.9	27.1		100.0	10.0
FPW1b-1	11.5	3.0		79.7	20.4		100.0	5.5
FPW1b-2	11.5	2.9		78.5	21.5		100.0	5.6
FPW1b-1	12.0	3.4		76.1	23.9		100.0	8.6
FPW1b-2	12.0	3.6		80.3	19.7		100.0	5.1
FPW2-1	9.5‡	n/a†			M			
FPW2-1	10.0	0.2†			M			
FPW2-2	10.0	0.3†			M			
FPW2-1	10.5	0.3		54.9	45.1		100.0	7.3
FPW2-2	10.5	0.6		38.9	61.1		100.0	7.9
FPW2-1	11.0	1.3		77.6	22.4		100.0	6.0
FPW2-2	11.0	1.7		66.0	33.1		100.0	5.4
FPW2-1	11.5	2.3		69.7	30.3		100.0	5.2
FPW2-2	11.5	1.9		67.9	32.1		100.0	5.3
FPW2-1	12.0	2.8		62.2	37.8		100.0	4.8
FPW2-2	12.0	2.5		65.2	34.8		100.0	4.7
PW	9.5	0.5	29.5	70.4	0.1		100.0	3.3
PW	10.0	4.0	3.1	96.7	0.2		100.0	7.6
PW	10.5	4.5	0.6	97.0	2.4		100.0	8.2
PW	11.0	5.2	0.3	96.1	3.6		100.0	6.9
PW	11.5	5.6	0.3	88.9	9.5	1.3	100.0	8.2
PW	12.0	11.3	7.3	47.8	28.1	16.8	100.0	5.0

*R_{wp} is the weighted pattern residual, a function of the least-squares residual.
†Precipitate samples were too small to conduct XRD and, in cases where no value for yield is reported, too small to weigh without substantial sample loss.
‡A poorly crystalline to amorphous Mg-silicate phase was observed in this sample using SEM.

EDX spectra (Figures A-5B, A-7C and A-8C) show incorporation of S and Sr into calcite. The S is likely present in the form of carbonate associated sulfate (CAS) where SO_4^{2-} tetrahedra experience limited substitution for triangular carbonate groups (CO_3^{2-}) in the calcite structure[16–17]. The observed Sr^{2+} is likely housed within Ca^{2+} sites in calcite as we did not observe precipitation of strontianite[18–19].

Acicular crystals of aragonite were observed in precipitates that formed from PW at pH 9.5. Brucite occurs as hexagonal plates, or spheroidal aggregates of plates, on the order of several 100s of nm in size at pH 10.0–12.0 (FPW1a), 10.5–12.0 (FPW1b and FPW2), and 9.5–12.0 (PW). Brucite becomes more abundant in precipitates from FPW1a, FPW1b, FPW2 and PW with increasing pH (Table A-7, Figure A-4). It was challenging to identify and image portlandite within aggregates of brucite, which have similar morphologies, and calcite, which has a similar EDX spectrum. Halite (NaCl), an artifact of the drying process, is occasionally observed as an evaporative coating on precipitate grains.

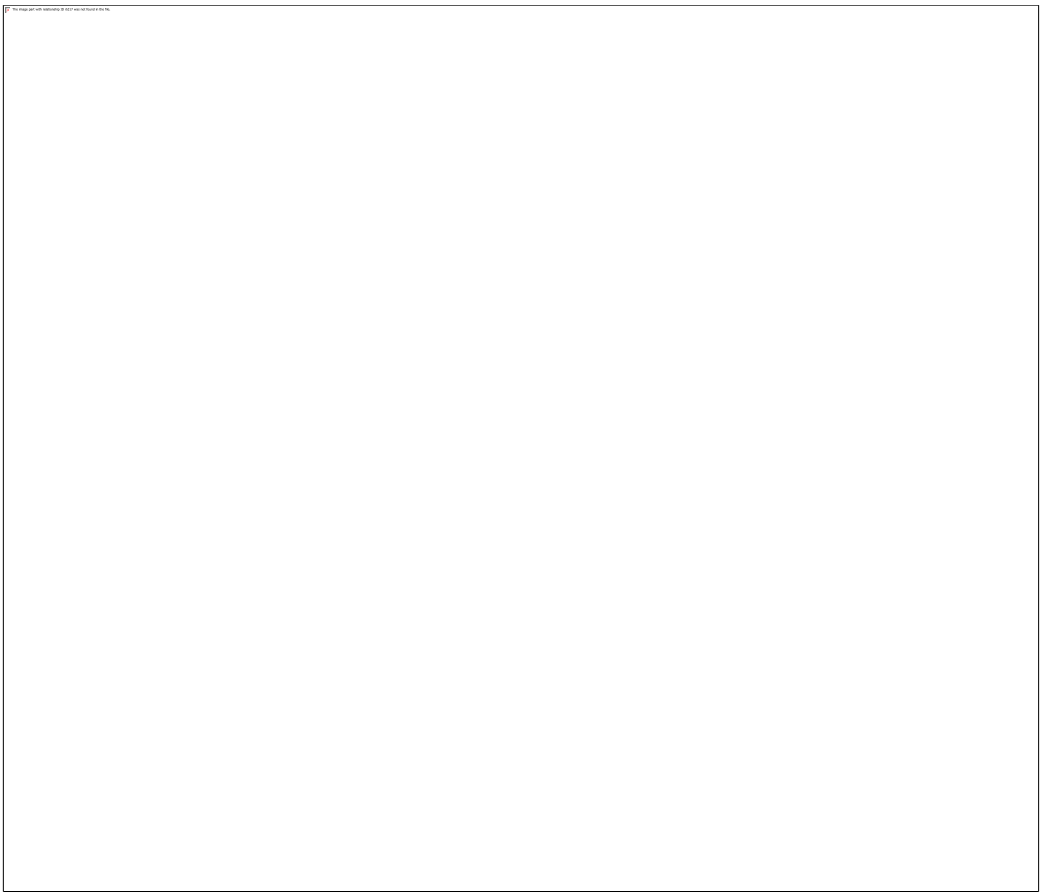

FIGURE A-4. Secondary electron SEM images of the precipitates from FPW1a at (A) pH 9.5, (B) pH 10.0, (C) pH 10.5 and (D) pH 12.0.

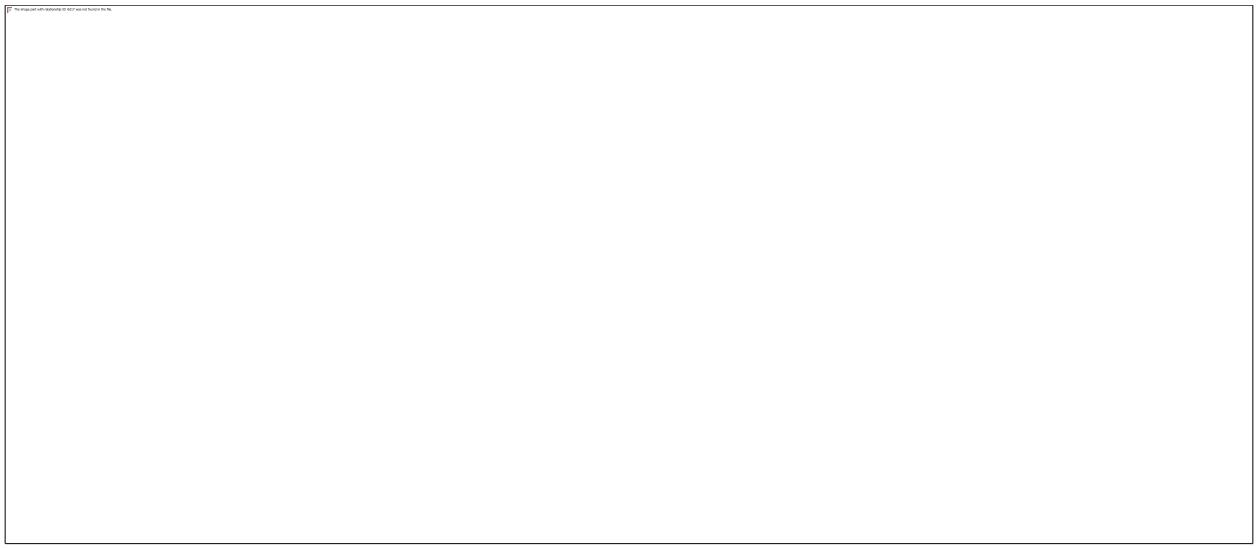

FIGURE A-5. Secondary electron SEM image (A) and EDX spectra (B and C) of the precipitates in FPW1a at pH 9.5. B: EDX spectra S- and Sr-rich calcite and trace amount of brucite. C: EDX spectra of a mixture of brucite, a Mg-silicate and trace amount of Mn-, Fe-, and Zn- phase(s). Sample is coated with carbon.

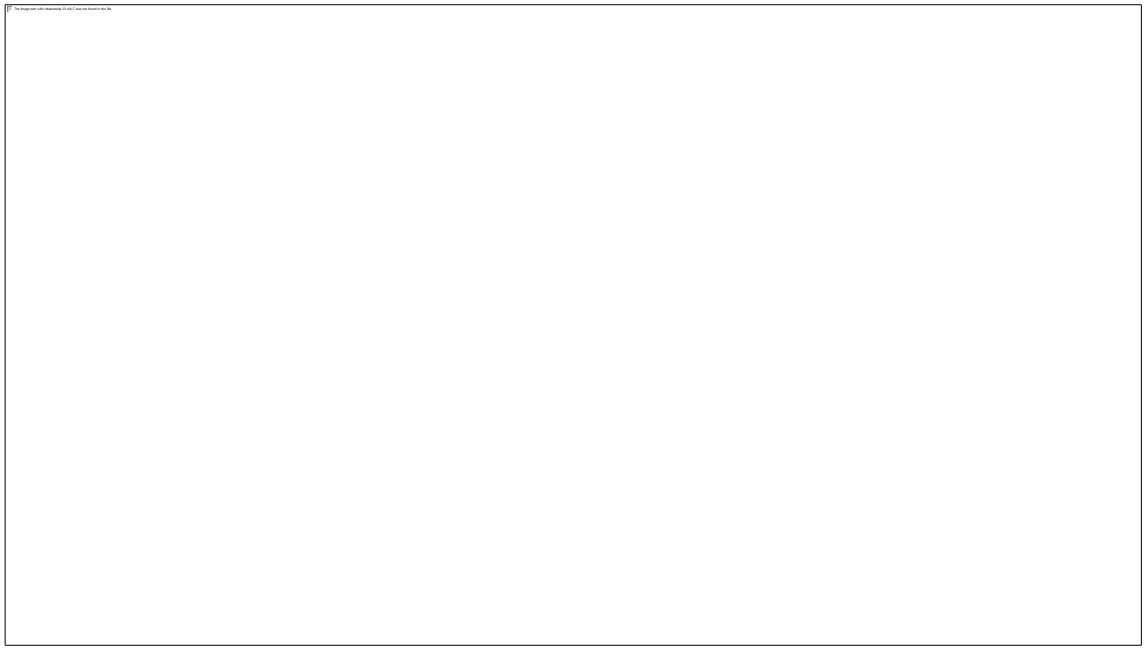

FIGURE A-6. XRD pattern of the precipitate at pH 9.5 from FPW2.

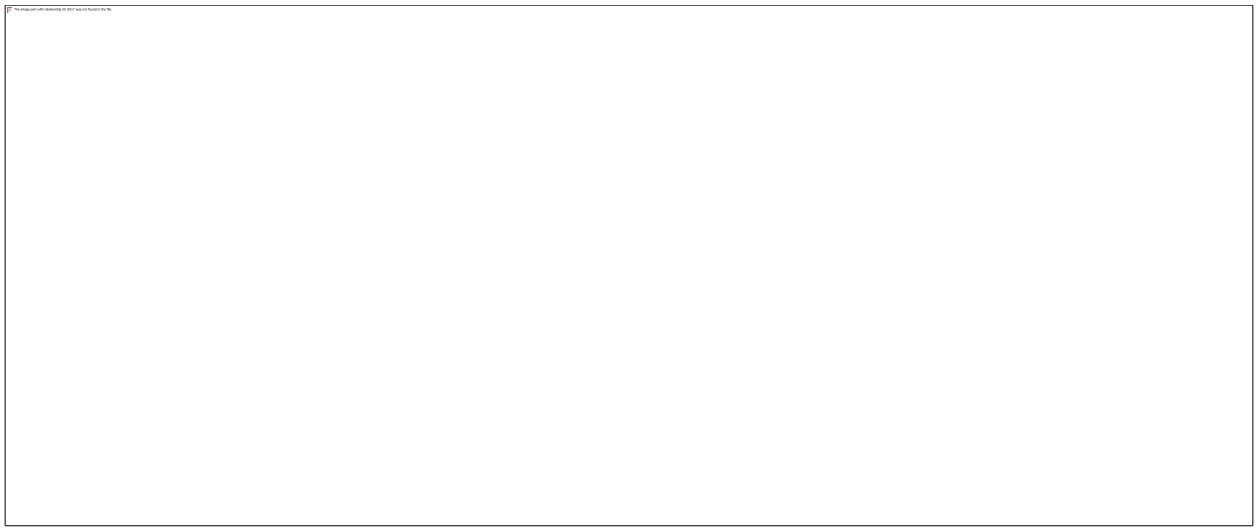

FIGURE A-7. Representative secondary electron SEM image (A) illustrates the phase distribution and morphology of the precipitates from FPW1b at pH 10.0–12.0. B: EDX spectra of a mixture of brucite, Mg-silicate, and trace amount of halite; C: EDX spectra S- and Sr-rich calcite.

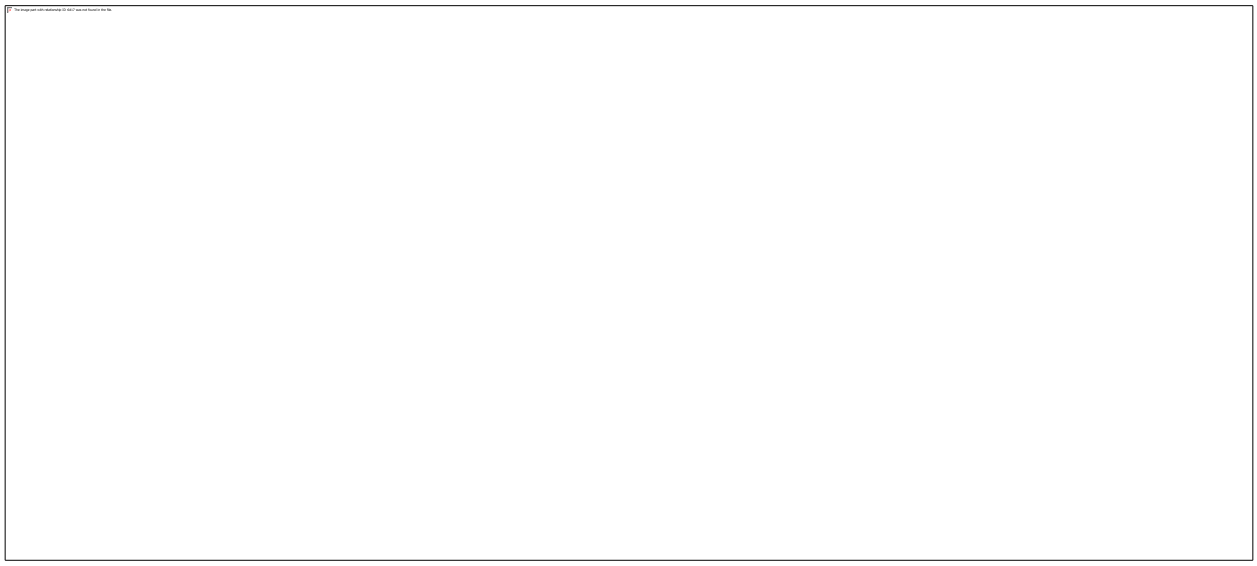

FIGURE A-8. Representative secondary electron SEM image (A) illustrates the phase distribution and morphology of the precipitates from FPW2 at pH 10.0–12.0. B: EDX spectra of a mixture of brucite, Mg-silicate, and trace amount of calcite and a Mn-rich phase; C: EDX spectra S- and Sr-rich calcite and trace amount of a Mg-silicate.

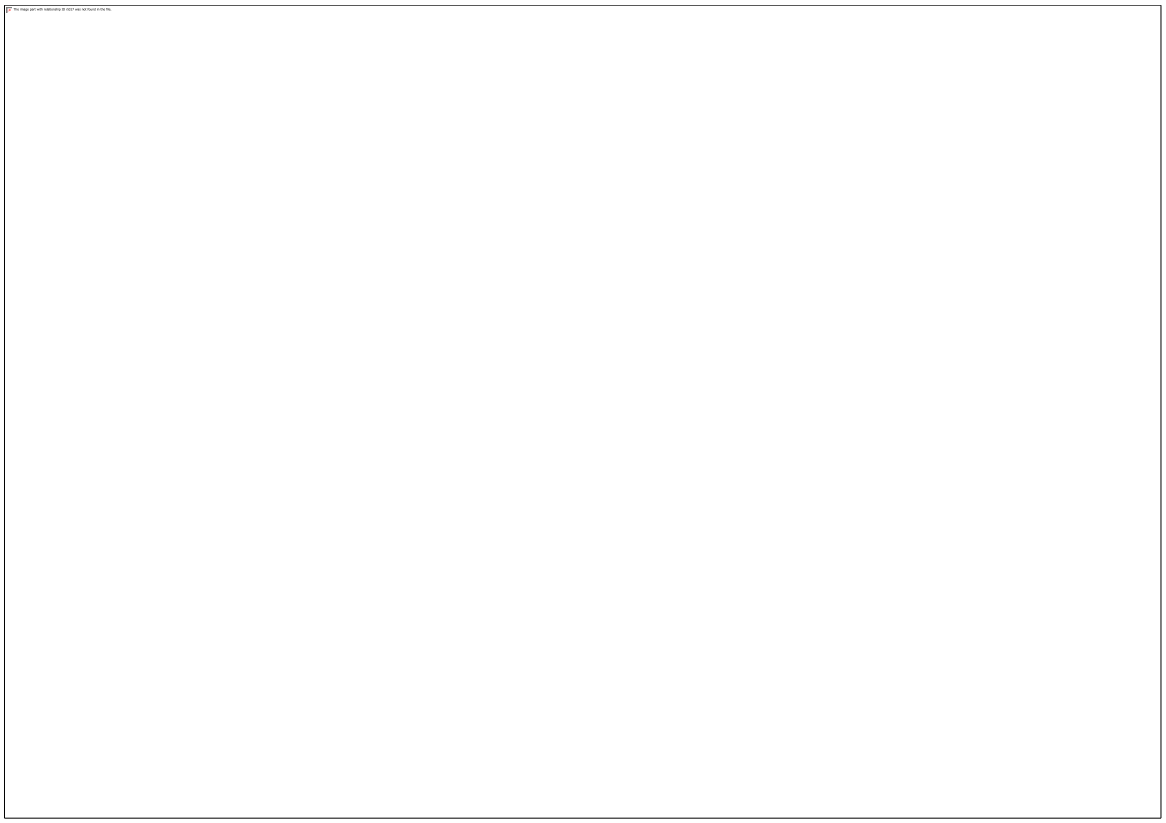

FIGURE A-9. Secondary electron SEM images of the precipitates from PW at pH 9.5 (A) pH 10.5 (B) and pH 12.0 (C). D: EDX spectrum of the precipitates at pH 12.0. The samples are coated with gold (which labelled in blue on the EDX spectrum). The phase abundance illustrated by the images cannot represents the trend as a function of pH in the precipitates from PW. Image (B) can represent the phase distribution and morphology in the precipitates at pH 10.5–11.5.

The modelling (Figure A-10) predicts that aragonite/calcite reach saturation at pH ~7.5, whereas the total precipitate yield become measurable (≥ 0.5g/L) at pH 9.0, when the prediction from PHREEQC indicates that the SI of aragonite/calcite reach maximum (SI = 1.9). The lag between the pH value when SI = 0 from prediction and the pH value of observed mineral precipitation can be attributable to one or more factors below: (1) mass of precipitates is smaller than the detection limit of scale; (2) activation barriers at low SI prohibit calcite nucleation and crystal growth; and (3) overestimation of SI due to the limitation of applying phreeqc.dat to model solution with high ionic strength. The modelling predicts brucite and portlandite respectively become saturation at pH ~9.5 and ~12.0, which generally matches (pH difference < 1.0 unit) the observation that brucite and portlandite precipitated at pH 10.0 and 12.0.

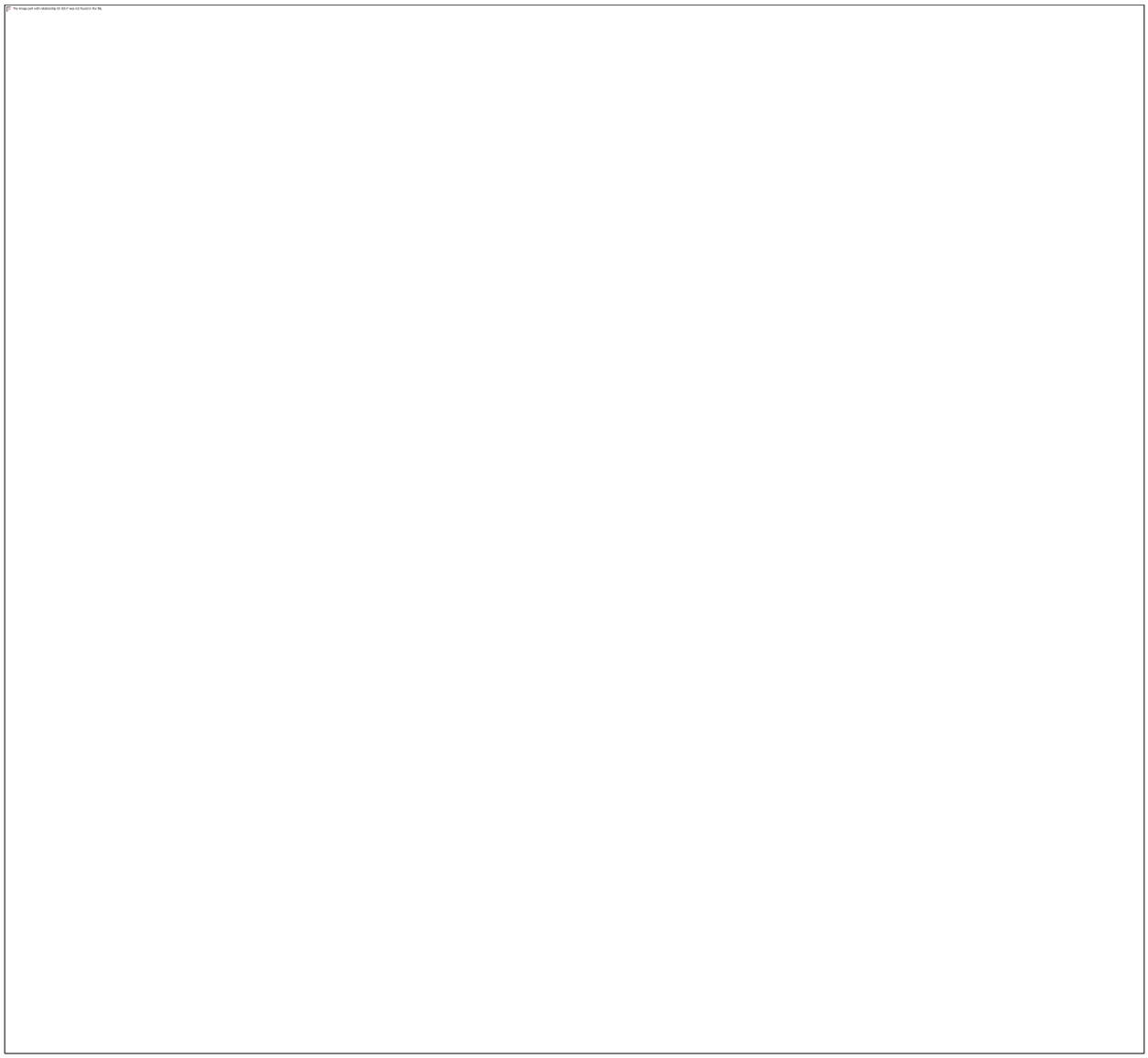

FIGURE A-10. The saturation index (SI) of mineral phases, calculated by PHREEQC phreeqc.dat, when titrating original FPW1a (applying solution chemistry in Table A-5) to pH 5.0 to 13.0. The modelling results predict that aragonite ($CaCO_3$), brucite [$Mg(OH)_2$], calcite ($CaCO_3$), disordered dolomite [$CaMg(CO_3)_2$], kerolite [$Mg_3Si_4O_{10}(OH)_2 \cdot H_2O$], portlandite [$Ca(OH)_2$], manganite (MnOOH), magnesite ($MgCO_3$), nesquehonite ($MgCO_3 \cdot 3H_2O$), hydromagnesite [$Mg_5(CO_3)_4(OH)_2 \cdot 4H_2O$], and dypingite [$Mg_5(CO_3)_4(OH)_2 \cdot 5H_2O$]. Solid plots represent phases precipitated, and dashed plots represent phases did not precipitate. In the titration experiment of

FPW1a, brucite, calcite, Mg-silicates, and portlandite were observed to precipitate at the pH 10.0 (vertical dashed red), 9.0 (vertical dashed yellow), 9.5 (vertical dashed grey), and 12.0 (vertical dashed dark blue), respectively. Precipitates were observed to form at pH 9.0 (vertical dashed light blue).

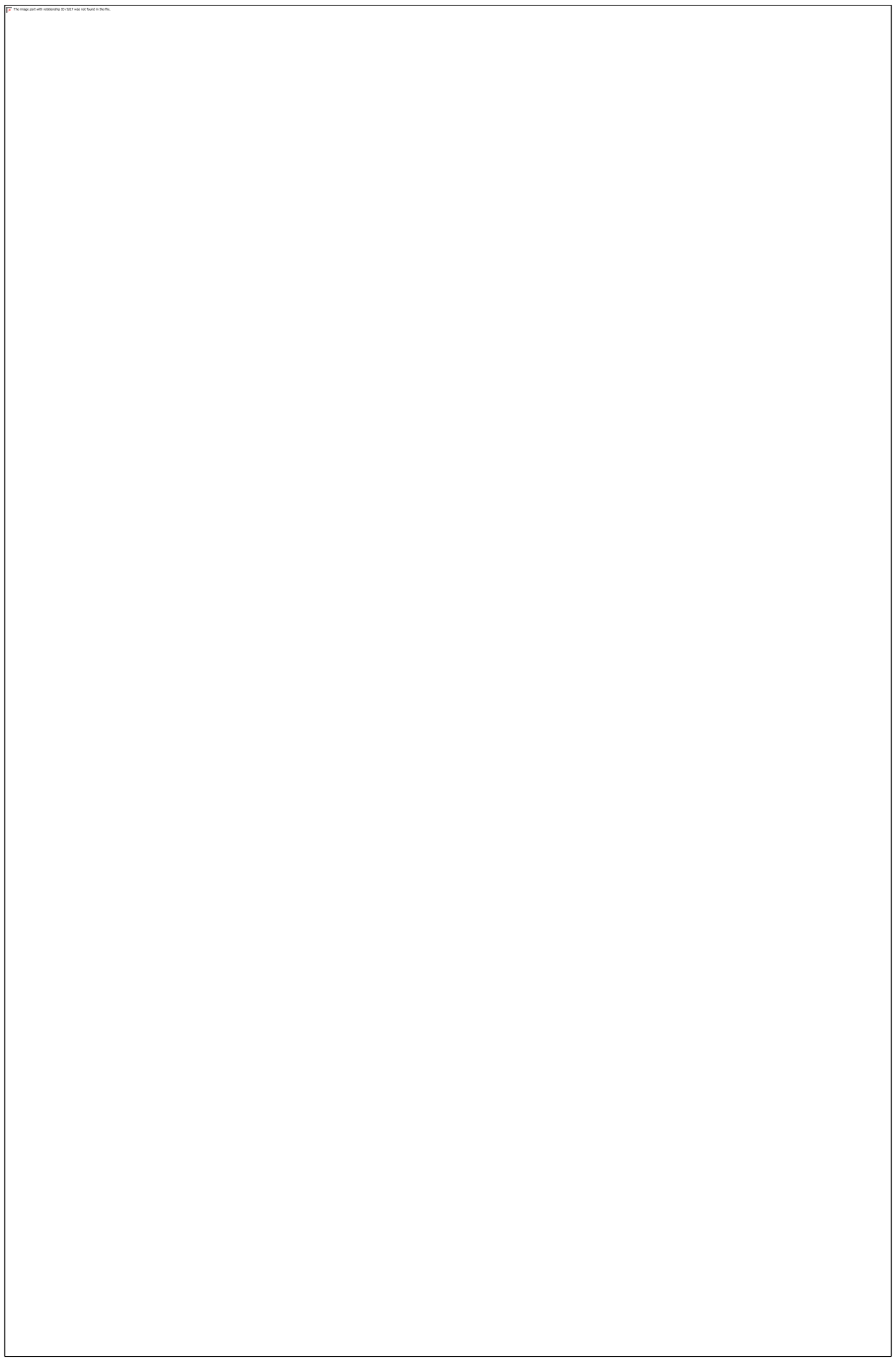

FIGURE A-11. Yield of (A) Ca and (B) Mg in precipitates from the titration experiments. Yield was calculated from the mass of precipitate and stoichiometric calculations using Rietveld refinement results. Generally, precipitates (Ppt.) were observed (shaded in blue) between pH 9.0 and 9.5; calcite (Cal) or aragonite (Arg), brucite (Brc), and Mg-silicate (M-Slc) were identified

(shaded in red) in the precipitates between pH ~9.5 and ~10.0. Portlandite (Por) was identified (dark blue dashed line) in the precipitates at pH ~12.0 for FPW1a and PW but was not observed for FPW1b or FPW2

We digested 14 precipitate samples, 3 precipitates from each of FPW1a and PW and 4 from each of FPW1b and FPW2, for ICP-MS analysis to investigate the immobilization of Al, B, Ba, Co, Cu, Fe, Li, Mn, Ni, P, Pb, S, Si, Sr, and Zn by precipitates (Table A-8) as well as assess the reliability of our XRD results. Figure A-12 shows that Ca (R^2 = 0.84) and Mg (R^2 = 0.95) concentrations calculated using stoichiometry and Rietveld refinement results have a strong positive linear correlation with concentrations measured directly using ICP-MS. Our results indicate that the use of the Rietveld method tends to overestimate the yield of Ca (by 30,100 ppm) and Mg (by 30,700 ppm), which might be due in part to the presence of the poorly crystalline to amorphous Mg-silicate phase.

Our ICP-MS results (Table A-8) show high Si concentrations (>1,000 ppm) in the precipitates. PHREEQC modelling (Figure A-10) indicates kerolite [$Mg_3Si_4O_{10}(OH)_2 \cdot H_2O$], a hydrated talc-like 2:1 phyllosilicate mineral reaches supersaturation when pH > 7.0 in FPW1a. EDX spectra commonly show the presence of Si in association with Mg in the precipitates (Figure A-5, A-7, A-8) and a trioctahedral 2:1 phyllosilicate phase is detectable in the pH 9.5 precipitates from FPW2 (Figure A-6), confirming it to be a poorly-crystalline, Mg-rich clay mineral such as stevensite. Zeyen et al. (2015)[20] reported precipitation of a kerolite/stevensite-like phase in alkaline crater lakes in Mexico where modelling indicated kerolite was supersaturated. Tosca et al. (2011)[21] synthesized a poorly crystalline Mg-silicate phase at 25 °C from Mg^{2+} and SiO_2(aq)-rich solutions at pH > 8.7. Thus, it is not unexpected that a kerolite/stevensite-like phase precipitated in our

experiments given the relatively high concentrations of Si (100s of ppm) in some brines (Table A-5).

The precipitates remove transition metals and other elements from brines. ICP-MS analysis of the precipitates (Tables A-8) shows that B and S concentrations in the precipitates are on average of 1,500 ppm and 406 ppm, respectively. Limited substitution of borate and sulfate anions for carbonate groups in Ca-carbonate minerals was observed at alkaline pH.[16–17,22–23] The Ca concentration in the precipitates is on average 95,300 ppm, and B and S together can only consume up to 0.02 wt% of Ca that captures CO_2 in the precipitates from mineral carbonation. The P concentrations in the untreated brines and precipitates are all below the detection limit of our analyses. Most of the anions that form minerals with Ca and Mg are present at comparatively much lower abundance, indicating that the influence of B, P, S and Si species on CO_2 capture potential of most FPW and PW should be negligible.

The transition metals, Fe, Mn, and Zn, are sometimes associated with aggregates of brucite and the kerolite/stevensite-like phase (Figure A-5C, A-7B and A-8B). The Na and Zn peaks in EDX spectra overlap with one another; however, because Na is always present in halite in these precipitate samples, the absence of a Cl peak (or a low intensity Cl peak) can be used to positively identify Zn (e.g., Figure A-5C). ICP-MS has a lower detection limit than EDX, giving more detailed information about transition metal incorporation into precipitates. ICP-MS results show that Pb (0–17.9 ppm) and the first-row transition metals Co (0–6.00 ppm), Fe (0–2,050 ppm), Mn (62.2–2,820 ppm), Ni (0–49.5 ppm) and Zn (28.0–253 ppm) become concentrated in the precipitates (Table A-8). The concentration of Cu in the untreated brines (Table A-5) and precipitates (Table A-8) is below the detection limit, except in the precipitates produced at pH 12.0 from FPW1a (19.4 ppm). According to the Goldschmidt's rules, Mg in brucite can be replaced by

Co, Cu, Fe, Mn, Ni, and larger cations such as Sr and Zn can substitute for Ca in calcite and aragonite. Our PHREEQC results (Figure A-11) suggest that the manganite (MnOOH) is supersaturated at pH > 9 for FPW1a, hence Mn and other first row transition metals might also precipitate as (oxy)hydroxide phases when the pH of brines is elevated. The Fe in the precipitates is likely associated with Fe-(oxy)hydroxides, which were observed to form from the same brine samples in a previous study[24]. Fe-(oxy)hydroxides are well known to sequester a wide variety of trace metals via both adsorption and absorption.[25–26] Other possible trapping mechanisms might be through sorption of Co, Cu, Mn, Ni, Pb, and Zn onto the surface of brucite[27–28] or substitution of Co, Fe, Mn, and Zn for Ca in calcite[29]. It is known that transition metals are retained by hydrated Mg-carbonate minerals, such as nesquehonite and hydromagnesite, during carbonation of transition-metal-bearing brucite,[30–31] as such we can expect these elements to remain immobilized during further carbonation of brine precipitates. Further work would be needed to pinpoint which phases host trace metals, and by what mechanisms, in order to design and optimize solutions for metal removal or metal recovery.

TABLE A-8. The concentration (ppm) of trace elements in the precipitates with ICP-MS analysis. Error is reported as 1 standard deviation (in brackets). Values are reported as 3 significant figures.

Sample	pH	Al	B	Ba	Co	Cu	Fe	Li	Mn	Ni	P	Pb	S	Si	Sr	Zn
FPW1a	10.5	192 (1)	670 (11)	BDL	BDL	BDL	460 (4)	BDL	1760 (30)	7.54 (0.3)	BDL	11.3 (0.2)	168 (10)	3940 (10)	325 (10)	130 (4)
FPW1a	11.5	93.4 (0.4)	1720 (8)	16.5 (3.4)	BDL	BDL	316 (5)	BDL	2510 (10)	BDL	BDL	12.9 (0.0)	761 (26)	5320 (20)	1150 (20)	153 (4)
FPW1a	12	BDL	230 (6)	2.29 (1.13)	BDL	19.4 (0.3)	152 (2)	BDL	541 (4)	BDL	BDL	3.48 (0.11)	97.6 (7.9)	1580 (50)	708 (13)	28.0 (2.6)
FPW1b	10.5	BDL	2640 (20)	8.31 (3.24)	2.73 (0.30)	BDL	358 (10)	BDL	180 (3)	6.14 (0.21)	BDL	17.9 (0.1)	549 (20)	3670 (100)	802 (16)	225 (2)
FPW1b	11	BDL	2170 (20)	9.13 (2.04)	3.25 (0.59)	BDL	422 (4)	BDL	164 (7)	5.82 (0.64)	BDL	13.1 (0.4)	800 (14)	3870 (100)	868 (8)	158 (5)
FPW1b	11.5	BDL	1900 (20)	7.62 (1.54)	2.08 (0.36)	BDL	233 (5)	BDL	62 (1)	4.77 (0.36)	BDL	11.8 (0.1)	592 (34)	2910 (40)	941 (12)	138 (3)
FPW1b	12	BDL	943 (12)	BDL	2.16 (0.08)	BDL	214 (4)	BDL	4310 (20)	6.44 (0.25)	BDL	9.61 (0.21)	288 (15)	2340 (20)	482 (13)	113 (4)
FPW2	10.5	5450 (20)	3210 (30)	22.1 (1.1)	6.00 (0.15)	BDL	2050 (20)	BDL	1940 (10)	49.5 (4.9)	BDL	BDL	576 (24)	825 (190)	1050 (10)	253 (14)
FPW2	11	BDL	2390 (20)	16.0 (3.1)	2.32 (0.47)	BDL	1370 (5)	BDL	1530 (20)	6.21 (1.01)	BDL	1.63 (0.11)	678 (4)	3910 (30)	1120 (20)	107 (0)
FPW2	11.5	BDL	1700 (20)	13.8 (5.2)	2.32 (0.20)	BDL	485 (14)	BDL	1260 (5)	11.9 (0.8)	BDL	BDL	678 (14)	3500 (30)	1130 (20)	89.3 (6.8)
FPW2	12	55.9 (0.9)	854 (7)	8.14 (2.46)	1.35 (0.07)	BDL	382 (11)	BDL	2820 (20)	11.3 (0.8)	BDL	BDL	340 (15)	2410 (80)	792 (13)	84.0 (0.5)
PW	10.5	BDL	1730 (50)	13.9 (1.4)	BDL	BDL	BDL	BDL	1950 (20)	BDL	BDL	3.66 (0.10)	BDL	1330 (30)	412 (10)	116 (3)
PW	11.5	30.1 (0.7)	664 (9)	BDL	BDL	BDL	BDL	BDL	1710 (30)	3.00 (0.51)	BDL	2.62 (0.08)	98.4 (2.6)	1000 (50)	42.0 (0.7)	92.4 (3.1)
PW	12	28.5 (1.6)	187 (8)	2.57 (0.40)	BDL	BDL	BDL	BDL	1430 (10)	BDL	BDL	BDL	55.2 (3.7)	902 (34)	183 (7)	50.2 (1.6)

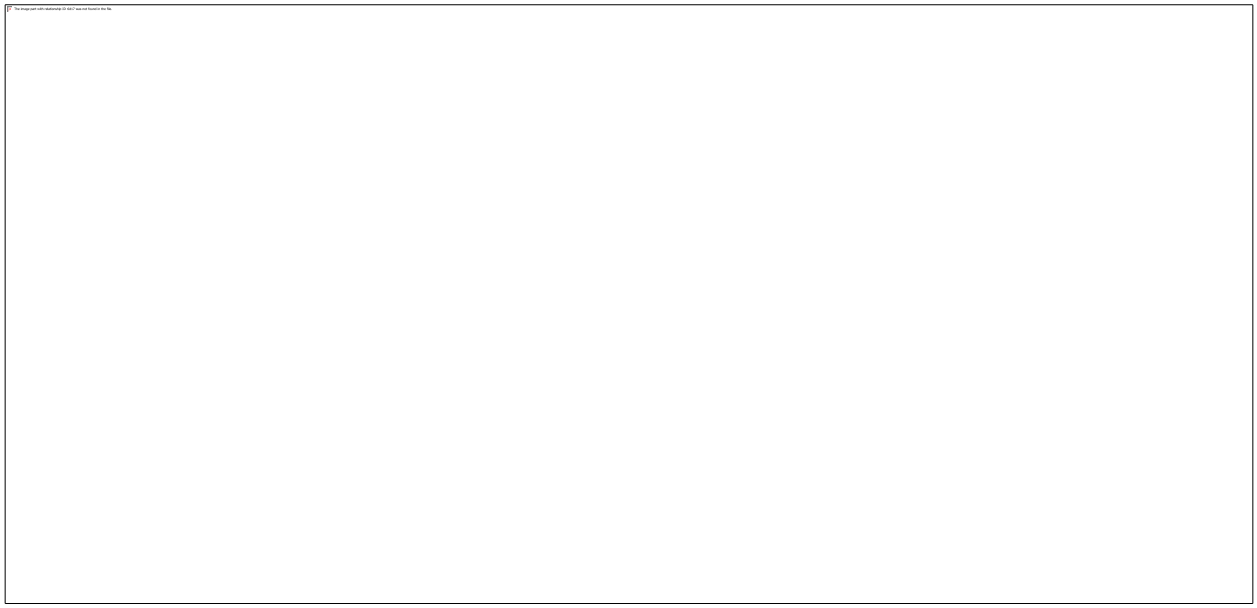

FIGURE A-12. Comparison of the yield of Ca and Mg as calculated using Rietveld refinement results versus results of direct measurement using ICP-MS analysis. The solid red lines plot y = x. The dashed blue lines are the lines of best fit to the data.

The estimation of CO_2 capture by annual FPW production in different countries are based on the annual FPW productions in the studies summarized in Table A-9. Table A-10 displays the calculation of CO_2 capture capacity by mass with the historical FPW production in Canada, China and the US at different titration pH (10.5–12.0) of the brines according to the experimental data in this study.

TABLE A-9. Estimates for FPW production in Canada, China and the USA.

Country	Year	Total FPW production (L)	Source	Formation(s)
Canada	2020	6.68×10^{10}	Zolfaghari et al., in preperation[32]	Western Canadian Sedimentary Basin
China	2014–2015	2.16×10^{9}	Zhong et al., (2021)[33]	Sichuan Basin
USA	2019	3.56×10^{11}	Zolfaghari et al., in preperation[32]	Appalachian, Anadarko, Denver, Fort Worth, Permian, Powder River, San Joaquin, Texas-Gulf, and Williston Basins

TABLE A-10. Calculation for the estimation of CO_2 capture capacity by mass with the historical FPW production in Canada, China and the US.

	Adjust solution pH and react at ambient condition for 1 day			If all the hydroxides from adjusting solution pH is carbonated			If all the Ca and Mg removed in solutions are carbonated		
pH	**Canada (kton)**	**US (kton)**	**China (kton)**	**Canada (kton)**	**US (kton)**	**China (kton)**	**Canada (kton)**	**US (kton)**	**China (kton)**
10.5	4.70	52.7	0.319	59.3	665	4.03	117	1310	7.94
11.0	6.01	67.3	0.408	71.5	802	4.86	132	1480	8.99
11.5	9.16	103	0.622	99.7	1120	6.77	196	2200	13.3
12.0	31.7	355	2.25	123	1380	8.36	252	2830	17.1

A4 Future Direction

FPW disposal and storage commonly occurs adjacent oil and gas production fields, as such mineral carbonation via CDR coupled to Ca/Mg looping could be done on site or in wastewater disposal plants (Figure 3-3). Further research needs to be conducted to maximize the efficiency of mineral carbonation using FPW. Firstly, the effect of increased pCO_2 needs to be examined as means to overcome the slow uptake of atmospheric CO_2 into solution. Alternatively, other alkaline industrial waste materials (e.g. hydrotalcite supergroup minerals from mine wastes[34]) could be explored to deliver atmospheric CO_2 and alkalinity into solution during anion exchange and partial dissolution in FPW. The use of mineral wastes such as these might reduce the cost of reagents, particularly NaOH, for mineral carbonation. Secondly, a comprehensive database, including the annual production volume and water chemistry of hydraulic fracturing flowback and produced waters by formation and country needs to be developed for a more accurate estimation of carbon capture potential. Finally, LCA/TEA is needed to assess the viability of this process for implementation as a CDR method for the oil and gas sector that both capitalizes on existing industry knowledge in CCS while valorizing abundant FPW as a resource.

A5 References

(1) Stringfellow, W. T.; Domen, J. K.; Camarillo, M. K.; Sandelin, W. L. Borglin, S. Physical, chemical, and biological characteristics of compounds used in hydraulic fracturing. J. *Hazard. Mater.* **2014**, *275*, 37–54.

(2) He, Y.; Sun, C.; Zhang, Y.; Folkerts, E.J.; Martin, J. W.; Goss, G. G. Developmental toxicity of the organic fraction from hydraulic fracturing flowback and produced waters to early life stages of zebrafish (Danio rerio). *Environ. Sci. Technol.* **2018**, *52*, 820–3830.

(3) Rostron, B. J.; Kelley, L. I.; Kreis, L. K.; Holmden, C. *Economic potential of formation brines: Interim results from the Saskatchewan brine sampling program*; Summary of investigations for Saskatchewan Geological Survey: 2002.

(4) Bish, D. L; Howard, S. A. Quantitative phase analysis using the Rietveld method. *J. Appl. Crystallogr.* **1988**, *21*, 86–91.

(5) Hill, R. J.; Howard, C. J. Quantitative phase analysis from neutron powder diffraction data using the Rietveld method. *J. Appl. Crystallogr.* **1987**, *20*, 467–474.

(6) Rietveld, H. M. A profile refinement method for nuclear and magnetic structures. *J. Appl. Crystallogr.* **1969**, *2*, 65–71.

(7) Cheary, R. W.; Coelho, A. A. A fundamental parameters approach to X-ray line-profile fitting. *J. Appl. Crystallogr.* **1992**, *25*, 109-121.

(8) Stephens, P.W. Phenomenological model of anisotropic peak broadening in powder diffraction. *J. Appl. Crystallogr*. **1999**, *32*, 281- 289.

(9) *Method 300.1: Determination of inorganic anions in drinking water by Ion Chromatography;* O1A0007929; U.S. Environmental Protection Agency, Environmental Monitoring and Support Laboratory: Cincinnati, OH, 1997; https://www.epa.gov/sites/production/files/2015-06/documents/epa-300.1.pdf

(10) Parkhurst, D. L.; Appelo, C. A. J. *Description of input and examples for PHREEQC Version 3—A computer program for speciation, batch-reaction, one-dimensional transport, and inverse geochemical calculations*; U.S. Geological Survey: Denver, Colorado, 2013.

(11) Pitzer, K. S. Thermodynamics of electrolytes. I. theoretical basis and general equations. *J. Phys. Chem.* **1973**, *77* (2), 268–277.

(12) Haase, C.; Dethlefsen, F.; Ebert, M.; Dahmke, A. Uncertainty in geochemical modelling of CO_2 and calcite dissolution in NaCl solutions due to different modelling codes and thermodynamic databases. *Appl. Geochemistry* **2013**, *33*, 306–317.

(13) Harrison, A. L.; Mavromatis, V.; Oelkers, E. H.; Bénézeth, P. Solubility of the hydrated Mg-carbonates nesquehonite and dypingite from 5 to 35 °C: implications for CO_2 storage and the relative stability of Mg-carbonates. Chem. Geol. **2019**, *504*, 123–135.

(14) Stoessell, R. K. 25°C and 1 atm dissolution experiments of sepiolite and kerolite. *Geochim. Cosmochim. Acta* **1988**, *52* (2), 365–374.

(15) Canadian Council of Ministers of the Environment: https://ccme.ca/en/current-activities/canadian-environmental-quality-guidelines.

(16) Kampschulte, A.; Strauss, H. The sulfur isotopic evolution of phanerozoic seawater based on the analysis of structurally substituted sulfate in carbonates. *Chem. Geol.* **2004**, *204* (3–4), 255–286.

(17) Pingitore, N. E.; Meitzner, G.; Love, K. M. Identification of sulfate in natural carbonates by X-Ray absorption spectroscopy. *Geochim. Cosmochim. Acta* **1995**, *59* (12), 2477–2483.

(18) Pingitore, N. E.; Lytle, F. W.; Davies, B. M.; Eastman, M. P.; Eller, P. G.; Larson, E. M. Mode of incorporation of Sr^{2+} in calcite: Determination by X-ray absorption spectroscopy. *Geochim. Cosmochim. Acta* **1992**, *56* (4), 1531–1538.

(19) Parkman, R. H.; Charnock, J. M.; Livens, F. R.; Vaughan, D. J. A study of the interaction of strontium ions in aqueous solution with the surfaces of calcite and kaolinite. *Geochim. Cosmochim. Acta* **1998**, *62* (9), 1481–1492.

(20) Zeyen, N.; Benzerara, K.; Li, J.; Groleau, A.; Balan, E.; Robert, J. L.; Estève, I.; Tavera, R.; Moreira, D.; López-García, P. Formation of low-T hydrated silicates in modern microbialites from mexico and implications for microbial fossilization. *Front. Earth Sci.* **2015**, *3*, 1–23.

(21) Tosca, N. J.; Macdonald, F. A.; Strauss, J. V.; Johnston, D. T.; Knoll, A. H. Sedimentary talc in Neoproterozoic carbonate successions. *Earth Planet. Sci. Lett.* **2011**, *306* (1–2), 11–22.

(22) Mavromatis, V.; Montouillout, V.; Noireaux, J.; Gaillardet, J.; Schott, J. Characterization of boron incorporation and speciation in calcite and aragonite from co-precipitation experiments under controlled pH, temperature and precipitation rate. *Geochim. Cosmochim. Acta* 2**015**, *150*, 299–313.

(23) Kobayashi, K.; Hashimoto, Y.; Wang, S. L. Boron incorporation into precipitated calcium carbonates affected by aqueous pH and boron concentration. *J. Hazard. Mater.* **2020**, *383*, 121183.

(24) Flynn, S.L.; von Gunten, K.; Warchola, T.; Snihur, K.; Forbes, T. Z.; Goss, G. G.; Gingras, M. K.; Konhauser K. O.; Alessi, D. S. Characterization and implications of solids associated with hydraulic fracturing flowback and produced water from the Duvernay Formation, Alberta, Canada. *Environ. Sci.: Processes Impacts* **2019**, *21*, 242–255.

(25) Manceau, A.; Schlegel, M. L.; Musso, M.; Sole, V. A.; Gauthier, C.; Petit, P. E.; Trolard, F. Crystal chemistry of trace elements in natural and synthetic goethite. *Geochim. Cosmochim. Acta* **2000**, *64* (21), 3643–3661.

(26) Trolard, F.; Bourrie, G.; Jeanroy, E.; Herbillon, A. J.; Martin, H. Trace metals in natural iron oxides from laterites: A study using selective kinetic extraction. *Geochim. Cosmochim. Acta* **1995**, *59* (7), 1285–1297

(27) Hövelmann, J.; Putnis, C. V.; Benning, L. G. Metal sequestration through coupled dissolution– precipitation at the brucite–water interface. Minerals 2018, 8, 346

(28) Hamilton, J. L., Wilson, S. A., Morgan, B., Harrison, A. L., Turvey, C. C., Paterson, D. J., Dipple, G. M., and Southam, G. Accelerating mineral carbonation in ultramafic mine tailings via direct CO2 reaction and heap leaching with potential for base metal enrichment and recovery. Econ. Geol. 2020, 115, 303–232.

(29) Reeder R. J.; Lamble G. M.; Northrrup P. A. XAFS study of the coordination and local relaxation around Co2+, Zn2+, Pb2+, and Ba2+ trace elements in calcite. Am. Mineral. 1999, 84, 1049–1060.

(30) Hamilton J. L.; Wilson S. A.; Morgan B.; Turvey C. C.; Paterson D. J.; MacRae C.; McCutcheon J.; Southam G. Nesquehonite sequesters transition metals and CO2 during accelerated carbon mineralisation. Int. J. Greenhouse Gas Control 2016, 55, 73–81

(31) Hamilton, J. L.; Wilson, S. A.; Morgan, B.; Turvey, C. C.; Paterson, D. J.; Jowitt, S. M.; McCutcheon, J.; Southam, G. Fate of transition metals during passive carbonation of ultramafic mine tailings via air capture with potential for metal resource recovery. Int. J. Greenhouse Gas Control 2018, 71, 155–167.

(32) Zolfaghari, A. University of Alberta, Edmonton. Personal communication, June 2021.

(33) Zhong, C., Zolfaghari, A., Hou, D., Goss, G. G., Lanoil, B. D., Gehman, J., Tsang, D. C. W., He, Y., Alessi, D. S. Comparison of the hydraulic fracturing water cycle in China and

North America: A critical review. *Environ. Sci. Technol.* **2021** In press. DOI: 10.1021/acs.est.0c06119

(34) Turvey, C. C.; Wilson, S. A.; Hamilton, J. L.; Tait, A. W.; McCutcheon, J.; Beinlich, A.; Fallon, S. J.; Dipple, G. M.; Southam, G. Hydrotalcites and hydrated Mg-carbonates as carbon sinks in serpentinite mineral wastes from the Woodsreef Chrysotile Mine, New South Wales, Australia: controls on carbonate mineralogy and efficiency of CO_2 air capture in mine tailings. *Int. J. Greenh. Gas Control* **2018,** *79*, 38–60.

APPENDIX B

Supporting Information for CHAPTER 3:

Accelerating mineral carbonation with hydraulic fracturing flowback and produced water using high pCO2 gas

B1 Methods

Duplicate carbonation Experiments CA and CB supplied a 10% CO_2/90% N_2 gas mix to pH-modified FPW at a constant flow rate of 250 mL/min for 27.5 hours under ambient laboratory conditions. A combination of X-ray diffraction (XRD), scanning electron microscopy (SEM), inductively coupled plasma mass spectrometry (ICP-MS), alkalinity, dissolved inorganic carbon, and stable carbon and oxygen isotope analyses were performed to characterize the precipitate and solution samples collected at each sampling point during the experiments.

B1.1 Experimental Apparatus

A schematic depiction of the experimental setup used in Experiments CA and CB is shown in Figure B-1.

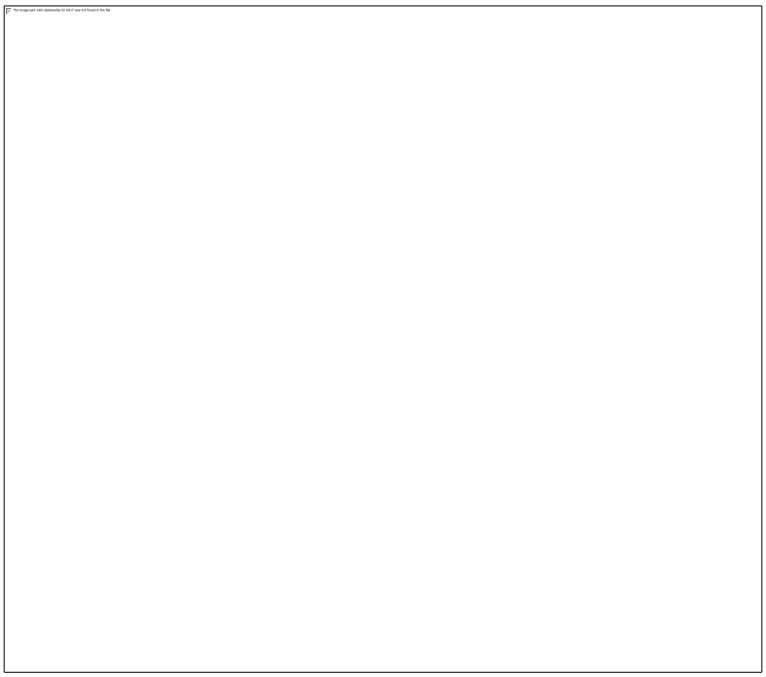

Figure B-1. Schematic diagram of carbonation experiments.

B1.2 Inductively Coupled Plasma Mass Spectrometry

The concentrations of ions in the brines and precipitates were analyzed with an Agilent 8800 Triple Quadrupole ICP-MS/MS. Brine samples were diluted approximately 910 times for Na and 83 times for other elements using > 18.2 MΩ·cm MilliQ water and then acidified using 12 µL trace metal grade nitric acid per 10 mL of diluted sample. The tune mode and scan type during the ICP-MS analysis, as well as the units of the analytes, are listed in TABLE B-1. External standard solutions and a blank were matrix matched with the brines by adding 2,000 ppm NaCl to these standards. External standards were analyzed every 10 samples at the start, middle, and end of each run.

Precipitates were reacted with 2.5 mL of 37% HCl for 8 hours at room temperature (18 °C) and then reacted for a further 1 h in a water bath at 75 °C. Any remaining solids were then dissolved in aqua regia by adding 0.83 mL of Fisher Scientific® 67% (w/w) HNO_3 (TraceMetal^{TM} Grade) and were then heat-activated in a water bath at 60°C for 1 hour. The resultant solutions were heated for another 8 hours until approximately 2 mL of solution was left. Prior to analysis, the remaining solutions were diluted to 50 mL with a solution of 2% HCl and 0.5% HNO_3. The analytes, tune mode, scan type and the internal standards used during ICP-MS analysis of precipitates are listed in TABLE B-2. Samples were aspirated with a micromist nebulizer and nickel/copper cones. Internal standard solutions (TABLES B-1 and B-2) were used to account for instrumental drift: 1 ppm of ^{45}Sc, ^{74}Ge, ^{115}In or ^{209}Bi were added to each sample utilizing an inline addition system.

Table B-1. Analytes, tune mode, scan type, and internal standards (ISTD) used in ICP-MS analysis of brine samples.

Analyte	Q1	Q2	Tune Mode	Scan Type	ISTD
Li	7	7	No Gas	MS/MS	45 Sc
B	11	11	No Gas	MS/MS	45 Sc
Na	23	23	He	MS/MS	115 In
Mg	24	24	He	MS/MS	45 Sc
Al	27	27	He	MS/MS	45 Sc
Si	28	28	H_2	MS/MS	45 Sc
K	39	39	He	MS/MS	45 Sc
P	31	47	O_2	MS/MS	74 Ge
S	32	48	O_2	MS/MS	74 Ge
Ca	40	40	H_2	MS/MS	45 Sc
Ti	47	47	He	MS/MS	74 Ge
Cr	52	52	He	MS/MS	74 Ge
Mn	55	55	He	MS/MS	74 Ge
Fe	56	56	He	MS/MS	74 Ge
Co	59	59	He	MS/MS	74 Ge
Ni	60	60	He	MS/MS	74 Ge
Cu	63	63	He	MS/MS	74 Ge
Zn	66	66	He	MS/MS	74 Ge
Br	79	79	He	MS/MS	74 Ge
Sr	88	88	He	MS/MS	74 Ge
As	75	91	O_2	MS/MS	74 Ge
Ba	137	137	He	MS/MS	115 In
Pb	208	208	No Gas	MS/MS	209 Bi

Table B-2. Analytes, tune mode, scan type, and internal standards (ISTD) used in ICP-MS analysis of precipitate samples.

Analyte	Q1	Q2	Tune Mode	Scan Type	ISTD
Li	7	7	No Gas	MS/MS	45 Sc
B	11	11	No Gas	MS/MS	45 Sc
Mg	24	24	He	MS/MS	45 Sc
Si	28	28	H_2	MS/MS	45 → 45 Sc
S	32	48	O_2	MS/MS	74 → 88 Ge
Mn	55	55	He	MS/MS	74 Ge
Fe	56	56	H_2	MS/MS	74 → 74 Ge
Co	59	59	He	MS/MS	74 Ge
Ni	60	60	He	MS/MS	74 Ge
Zn	66	66	He	MS/MS	74 Ge
Sr	88	88	He	MS/MS	74 Ge
Pb	208	208	No Gas	MS/MS	209 Bi

B1.3 Powder X-Ray Diffraction

Forty-six precipitate samples were ground by hand under anhydrous ethanol using an agate mortar and pestle. Each sample was mounted as an ethanol slurry onto a zero-background quartz plate. Once samples had air-dried, powder X-ray diffraction (XRD) patterns were collected using a Bruker D8 Advance θ–θ powder X-ray diffractometer equipped with a LYNXEYE XE-T 1D Position Sensitive Detector in the Environmental Economic Geology Laboratory, University of Alberta. Data acquisition was done using a Co X-ray tube that was operated at 35 kV and 40 mA. All patterns were collected over a 2θ range of 3–80° using a step size of 0.02° 2θ and a dwell time of 1–4 second/step. Longer acquisition times were generally used for smaller samples.

Mineral phase identification was conducted using the DIFFRAC.EVA XRD phase analysis software (Bruker) with reference to the International Center for Diffraction Data Powder Diffraction File 4+ database (ICDD PDF4+). Rietveld refinements[1–3] employing XRD data were

done with TOPAS 5 (Bruker) to determine relative mineral abundances, to estimate crystallite size and strain, and to refine the unit cell parameters for each phase. The goniometer zero error for the diffractometer was determined via refinement using an XRD pattern of NIST SRM 660b LaB_6, which has a very precisely known unit cell parameter. By holding the calibrated zero error fixed during refinements of unknown samples, we were able to determine unit cell parameters and peak positions for constituent minerals accurately and precisely.

Minimum and maximum values were used to constrain unit cell parameters and crystallite size and strain to physically meaningful values within the framework of the Double-Voight approach[4]. The method of Stephens[5] was used to model anisotropic peak broadening for calcite (hexagonal/rhombohedral). Because XRD data were collected from thin slurries, rather than 'infinitely thick' powder mounts, our quantitative phase analysis (QPA) results should be considered 'semi-quantitative'. The accuracy of Rietveld QPA results in this system was assessed using ICP-MS results for Ca and Mg concentrations in precipitates (Zhu et al., in preparation; Chapter 2)[5], and the estimated elemental concentrations obtained using XRD results compare favourably with measured values from ICP-MS ($R^2 = 0.84$ for Ca and $R^2 = 0.95$ for Mg).

B1.4 Scanning Electron Microscopy

Aliquots of selected precipitate samples were mounted on aluminum (Al) stubs using carbon tape and coated with gold (Au) or carbon (C). Scanning Electron Microscope (SEM) images and Energy-Dispersive X-ray Spectra (EDS) of samples were obtained using a Zeiss Sigma 300 Variable Pressure Field Emission Scanning Electron Microscope, equipped with a Bruker energy dispersive X-ray spectroscopy (EDS) system, in the Scanning Electron Microscope Laboratory at

the Department of Earth and Atmospheric Sciences, University of Alberta. An operating voltage of 10 kV was used to obtain SEM images and EDS data for major elements (e.g., C, Mg, Ca). EDS data were obtained using an operating voltage of 15 kV and a measurement time of 5 minutes for trace transition metals.

B1.5 Alkalinity and Dissolved Inorganic Carbon

The alkalinity of solutions was measured immediately after the collection of each sample using the spectroscopic method of Sarazin et al.[6]. Absorbance of samples was measured with a Hach UV-VIS spectrophotometer and a calibration curve produced via dilution of a 0.01 M $NaHCO_3$ solution. Dissolved inorganic carbon (DIC) concentrations were determined using a CO_2 coulometer (CM5017, UIC Inc, USA) in the School of the Environment, Trent University. This instrument measures the absolute mass of inorganic carbon in a sample. A 1 mL aliquot of each sample was loaded into a 25 mL glass flask and acidified with 2 N H_2SO_4 (10 mL) at 50 °C and the evolved CO_2 gas was directed to a colorimetric cell. A pre-scrubber solution (KOH 45 v/v%) was used to remove any CO_2 present in the carrier gas (100 mL/min) and a post scrubber ($AgNO_3$ 3 v/v%) was used to remove H_2S, SO_x, and/or halogens from the gas stream, which can form as a result of the sample acidification. The colorimetric cell was partially filled by an aqueous solution containing monoethanolamine, a colorimetric indicator, and two electrodes (platinum and silver). As CO_2 reacted with monoethanolamine to form a titratable acid (hydroxyethylcarbamic acid), electrochemically generated OH^- in the platinum electrode neutralized the solution until it returned to its original color or original percent transmittance. The color change of the solution was measured as a percent transmittance (%T) using a photodetector and was proportional to the concentration of hydroxyethylcarbamic acid formed and, therefore, equivalent to the amount of

inorganic carbon injected into the cell. The analytical errors of DIC measurements were determined by least squares regression. The regression statistics (TABLE B-3) and ANOVA table (TABLE B-4) of the least squares regression from 12 calibration points are listed below.

Table B-3. Regression statistics for the least squares fit to the calibration curve for DIC analyses.

Regression coefficient R	0.99727662
R Square	0.994560657
Adjusted R Square	0.994016722
Standard Error	1.654899921
Observations	12
Intercept	-0.48875
Intercept Standard Error	1.013415096
Gradient	0.917286434
Gradient Standard Error	0.021451742

Table B-4. ANOVA table for the least squares fit to the calibration curve for DIC analyses.

	df	SS	MS	F	Significance F
Regression	1	5007.584429	5007.58443	1828.457245	1.17441E-12
Residual	10	27.3869375	2.73869375		
Total	11	5034.971367			

B1.6 Stable Carbon and Oxygen Isotope Analyses

The $\delta^{13}C$ values of dissolved inorganic carbon (DIC) in brines, the $\delta^{18}O$ values of water in brines and the $\delta^{13}C$ and $\delta^{18}O$ values of precipitated carbonate minerals were analyzed at Ruhr-Universität Bochum.

The $\delta^{13}C$ values of DIC were determined from CO_2 released by reacting samples with 85% phosphoric acid in He-flushed glass vials at room temperature for 24 hours. Aliquots of carbonate samples (90–110 μg) were dried in an oven at 105 °C to remove moisture for at least 24h and then reacted with phosphoric acid at 70 °C. Before reaction with phosphoric acid, both water samples

and solid carbonate samples were placed in GC Pal autosampler (CTC Analytics) and each sample vial was pre-flushed with He to remove air. The stable carbon and oxygen isotopic compositions of evolved CO_2 gas were measured with a ThermoFisher Scientific MAT253 mass spectrometer equipped with a ConFloIV and a GasBenchII. Certified standards, IAEA-603 and NBS18, were used for two-point calibration. $\delta^{13}C$ values are reported using the delta (δ) notation in permil (‰) relative to Vienna Pee Dee Belemnite (VPDB).

$\delta^{18}O$ values of water were obtained from brine samples that were stored with zero headspace in 1.5-mL septum vials. These samples were stored in a refrigerator at 5 °C until analysis. Water samples were placed in ThermoFisher Scientific AS3000 autosampler and analysed with a CF-IRMS253plus equipped with a ConFloIV and a TC/EA by converting H_2O into H_2 and CO gases. The temperature of the TC/EA reactor and GC column were maintained at 1400 °C and 90 °C, respectively. Standardization of two in-house reference solutions was accomplished using VSMOW2, SLAP2 and GRESP reference solutions (IAEA). The 1σ reproducibility of in-house (internal) water standards is: $\delta^{2}H$: ± 1.1‰ and $\delta^{18}O$: ± 0.17‰ (n =31). $\delta^{18}O$ values are reported using the delta (δ) notation in permil (‰) relative to Vienna Standard Mean Ocean Water (VSMOW).

B1.7 Geochemical Modelling

Saturation indices for relevant minerals were modelled using aqueous geochemistry data and USGS PHREEQC version 3 (Parkhurst and Appelo[7]). The phreeqc.dat database, which uses the ion-dissociation method for the calculation of ion activity, was used for this purpose. Although the pitzer.dat database uses an activity model targeting high ionic strength solutions, the modelling of

saline solutions using pitzer.dat does not yield lower uncertainties than using phreeqc.dat.[8] Previous studies of high ionic strength solutions have found that the abundant thermodynamic data of elements and aqueous complexes afforded by phreeqc.dat gives similar results for the calculation of aqueous complexes as pitzer.dat (Zhu et al, in preparation; Chapter 2)[5]. Here we consider the saturation indices (SI) of hydrated Mg-carbonates {dypingite [$Mg_5(CO_3)_4(OH)_2 \cdot \sim 5H_2O$]; hydromagnesite [$Mg_5(CO_3)_4(OH)_2 \cdot 4H_2O$] and nesquehonite ($MgCO_3 \cdot 3H_2O$)}, magnesite ($MgCO_3$), calcite ($CaCO_3$), strontianite ($SrCO_3$), and kerolite [$Mg_3Si_4O_{10}(OH)_2 \cdot H_2O$] (TABLE B-5).

Table B-5. Solubility products for nesquehonite, dypingite, hydromagnesite and kerolite used in addition to the solubility data already available in the phreeqc.dat database.

Mineral phase	Equation	T (°C)	log K_{sp}	Source
Nesquehonite	$MgCO_3 \cdot 3H_2O = Mg^{2+} + CO_3^{2-} + 3H_2O$		–5.621	wateq4f.dat
Dypingite	$Mg_5(CO_3)_4(OH)_2 \cdot 5H_2O = 5Mg^{2+} + 4CO_3^{2-} + 2OH^- + 5H_2O$	25	−34.94 ± 0.58	Harrison et al. (2019)[9]
Hydromagnesite	$Mg_5(CO_3)_4(OH)_2 \cdot 4H_2O + 2H^+ = 5Mg^{2+} + 4CO_3^{2-} + 6H_2O$		–8.762	wateq4f.dat
Kerolite	$Mg_3Si_4O_{10}(OH)_2 \cdot H_2O + 6H^+ = 3Mg^{2+} + 4SiO_2\,(aq) + 5H_20$	25	25.79 ± 0.24	Stoessell (1988)[10]

B2 Results

Elemental concentrations of aqueous species in the original brine samples are given in (Table B-6). Conductivity (Figure B-2A), bicarbonate alkalinity (Figure B-2B), dissolved inorganic carbon (DIC), carbon isotope composition of DIC, oxygen isotope composition of brines, mass change, pH, temperature, and relative humidity values during the carbonation experiments are reported in Tables B-7 and B-8. Concentration of Ca, Mg, and Si of brine samples during the experiments are

reported Figure B-3. Characterization of precipitates included phase identification (Figures B-4–B-6) and quantification of mineral abundances using XRD (Table B-9 and B-10). Geochemical modelling was used to calculate the SI of carbonate minerals when elevate brine pH prior to injection of CO_2 gas is displayed in Figure B-7. Mass change as a function of time and total yield of precipitates are displayed in Figure B-8.

Table B-6. The concentration (conc.) of elements in the original FPW in Experiments CA and CB based on ICP-MS analysis. Detection limit (DL) is reported when measurements are below the detection limit (BDL). All values are reported to 3 significant figures.

	Experiment CA			Experiment CB		
Element	**Conc. (ppm)**	**Error† (ppm)**	**DL (ppm)**	**Conc. (ppm)**	**Error† (ppm)**	**DL (ppm)**
Na	56900*	1960		56900*	1950	
Ca	10200	100		9930	170	
Cl	124000*			124000*		
Br	243	7		230	5	
K	1850	0		1790	40	
Mg	791	25		780	28	
Sr	934	25		927	24	
Al	BDL		2.71	BDL		2.70
As	BDL		1.25	BDL		1.24
B	70.9	0.2		68.4	1.4	
Ba	3.82	0.07		3.79	0.17	
Cr	BDL		0.704	BDL		0.699
Co	0.0539	0.0075		0.0522	0.0220	
Cu	BDL		0.883	BDL		0.876
Fe	BDL		3.52	BDL		3.50
Li	35.1	0.2		35.2	0.5	
Mn	3.54	0.12		3.46	0.15	
Ni	BDL		2.92	BDL		2.90
P	BDL		6.55	BDL		6.50
Pb	0.0879	0.00		0.0879	0.0005	
S	59.7	0.4		56.2	1.4	
Si	12.6	0.4		11.5	0.4	
Ti	0.340	0.589		BDL		0.325
Zn	1.98	0.08		2.26	0.09	

*Na and Cl concentrations are only used for the estimation of ionic strength in PHREEQC modelling, and the results are from Zhu et al. (in preparation)[5].
†Error is reported as 1 standard deviation. Detection limit (DL) is sample specific.

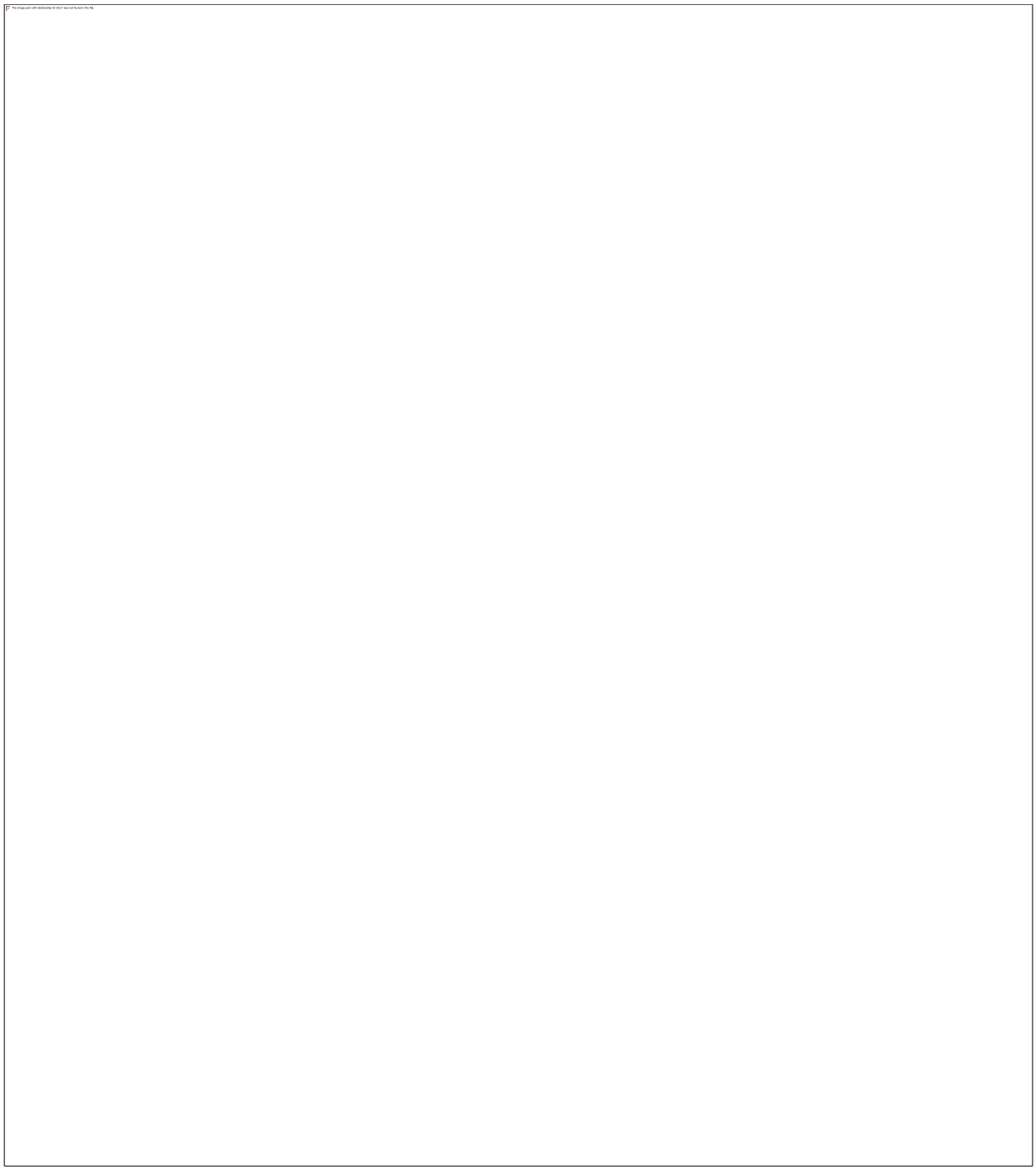

Figure B-2. Values for (A) conductivity (mS/cm) and (B) HCO_3^- alkalinity in mg C/L) during the carbonation experiment

Table B-7. Results of mass change (Δm), pH, temperature, relative humidity (RH) and stable isotope analysis for Experiment CA. Mass change (Δm) during experiments is calculated following the equation $\Delta m_n = m_{f(n-1)} - m_{i(n)}$, where n represents n^{th} sampling. Analytical errors for stable isotope data are reported as 2σ (in brackets).

Sample ID	Time (min)	m_i (g)	m_f (g)	Δm (g)	pH	T (°C)	RH (%)	DIC (mg C/L)	$\delta^{13}C_{VPDB}$ DIC (‰)	$\delta^{13}C_{VPDB}$ calcite (‰)	$\delta^{18}O_{VSMOW}$ calcite (‰)	$\delta^{18}O_{VSMW}$ brine (‰)
CA10-original	-	-	-	-	6.0	-	-	1.8	-	-	-	1.5(0.2)
CA10t0	0	2852.1	2839.5	-	10.4	17.5	16.0	1.3	-	-	-	-0.3(0.2)
CA10t5	5	2838.8	2803.2	0.7*	10.1	17.4	16.0	-	-	-	-	-0.5(0.2)
CA10t10	10	2804.6	2790.8	-1.4	9.7	17.4	16.0	0.7	-	-	-	-
CA10t15	15	2791.5	2786	-0.7	9.8	17.4	16.0	-	-	-	-	-0.3(0.2)
CA10t20	20	2786.2	2775.6	-0.2	9.4	17.4	16.0	0.4	-	-	-	-
CA10t25	25	2775.9	2768.1	-0.3	8.8	17.4	16.0	0	-	-	-	-
CA10t30	30	2768	2774.8	0.1	7.9	17.6	16.0	-	-	-39.7(0.04)	11.1(0.04)	-0.2(0.2)
CA10t40	40	2772.4	2766.9	2.4	6.7	17.5	16.0	36.9	-	-	-	-
CA10t50	50	2764.8	2759.6	2.1	6.4	17.5	16.0	-	-36.3(0.04)	-36.5(0.04)	12.6(0.08)	-0.2(0.2)
CA10t60	60	2757.2	2748.1	2.4	6.4	17.6	16.0	-	-32.2(0.02)	-36.3(0.02)	13.1(0.1)	-0.4(0.2)
CA10t90	90	2745.4	2735.9	2.7	6.4	17.6	16.0	50.9	-	-	-	-
CA10t120	120	2734.7	2748.3	1.2	6.3	17.4	16.0	50.1	-	-	-	-
CA10t150	150	2743.5	2756.2	4.8	6.3	17.3	16.0	-	-21.0(0.08)	-34.1(0.02)	15.6(0.08)	-0.7(0.2)
CA10t180	180	2745.7	2731.4	10.5	6.3	17.3	16.0	50.1	-	-	-	-
CA10t210	210	2706.3	2718.3	25.1	6.4	17.4	16.0	-	-24.4(0.04)	-33.4(0.04)	16.4(0.06)	-0.7(0.2)
CA10t240	240	2710.3	2688	8.0	6.3	17.4	16.0	63.9	-	-	-	-
CA10t270	270	2686.2	2697.2	1.8	6.4	17.5	16.0	-	-21.6(0.04)	-32.8(0.06)	16.8(0.08)	-0.6(0.2)
CA10t330	330	2686	2639.5	11.2	6.8	17.7	16.0	38.9	-	-	-	-
CA10t480	480	2636.1	2597.7	3.4	6.3	17.7	16.0	-	-21.9(0.1)	-32.1(0.04)	17.7(0.08)	-0.6(0.2)
CA10t22h	1320	2591.3	2600	6.4	6.3	16.5	16.0	18.0	-	-	-	-
CA10t27h	1620	2593.3	2587.4	6.7	6.7	16.8	16.0	-	-	-31.6(0.04)	18.0(0.06)	-0.6(0.2)
CA10t27.5h	1650	2587.4	-	0.0	64	17.1	16.0	29.8	-23.9(0.06)	-31.6(0.08)	18.0(0.04)	-0.8(0.2)

*e.g. Mass change between t = 0–5 minutes is calculated as $\Delta m_{t5} = \Delta m_{ft0} - \Delta m_{it5}$.

Table B-8. Results of mass change (Δm), pH, temperature, relative humidity (RH) and stable isotope analysis for Experiment CB. Mass change (Δm) during experiments is calculated following the equation $\Delta m_n = m_{f(n-1)} - m_{i(n)}$, where n represents n^{th} sampling. Analytical errors for stable isotope data are reported as 2σ (in brackets).

Sample ID	Time (min)	m_i (g)	m_f (g)	Δm (g)	pH	T (°C)	RH (%)	DIC (mg C/L)	$\delta^{13}C_{VPDB}$ DIC (‰)	$\delta^{13}C_{VPDB}$ calcite (‰)	$\delta^{18}O_{VSMOW}$ calcite (‰)	$\delta^{18}O_{VSMOW}$ brine (‰)
CB10-original	-	-	-	-	5.7	-	-	0.6	-	-	-	0.7(0.2)
CB10t0	0	2964.2	2939.0	-	10.4	18.5	22.3	1.0	-	-	-	-0.5(0.2)
CB10t5	5	2933.0	2840.5	6.0*	10.0	18.7	22.1	-	-	-	-	-0.6(0.2)
CB10t10	10	2843.5	2826.6	-3.0	9.9	18.7	22.1	1.5	-	-	-	-
CB10t15	15	2829.8	2816.3	-3.2	9.7	18.7	22.2	-	-	-46.6 (0.04)	12.6(0.04)	-0.6(0.2)
CB10t20	20	2819.8	2808.0	-3.5	9.2	18.7	22.2	0.9	-	-	-	-
CB10t25	25	2810.5	2799.4	-2.5	8.7	18.7	22.3	1.3	-	-	-	-
CB10t30	30	2800.9	2793.4	-1.5	8.2	18.7	22.2	-	-	-38.9(0.04)	9.9(0.06)	-0.8(0.2)
CB10t40	40	2794.7	2789.7	-1.3	6.7	18.7	22.2	35.8	-	-	-	-
CB10t50	50	2790.4	2780.6	-0.7	6.5	18.7	22.2	-	-36.2(0.02)	-37.8(0.04)	12.9(0.04)	-0.7(0.2)
CB10t60	60	2780.5	2765.2	0.1	6.4	18.6	22.5	-	-32.2(0.04)	-37.3(0.02)	14.2(0.06)	-0.8(0.2)
CB10t90	90	2764.6	2759.7	0.6	6.3	18.6	22.8	69.1	-	-	-	-
CB10t120	120	2758.7	2753.7	1.0	6.4	18.3	22.4	62.1	-	-	-	-
CB10t150	150	2752.8	2731.3	0.9	6.4	18.5	22.6	-	-25.2(0.04)	-32.6(0.04)	17.1(0.06)	-0.8(0.2)
CB10t180	180	2732.9	2721.1	-1.6	6.3	18.5	22.9	68.5	-	-	-	-
CB10t210	210	2721.6	2712.8	-0.5	6.3	18.5	22.7	-	-25.7(0.02)	-32.6(0.02)	17.1(0.06)	-0.9(0.2)
CB10t240	240	2714.1	2707.3	-1.3	6.3	18.8	23.3	62.5	-	-	-	-
CB10t270	270	2707.0	2707.0	0.3	6.3	18.8	23.5	-	-24.3(0.02)	-33.5(0.06)	18.0(0.06)	-0.9(0.2)
CB10t330	330	2704.1	2678.9	2.9	6.3	18.3	23.7	60.0	-	-	-	-
CB10t480	480	2678.6	2673.4	0.3	6.3	18.1	26.2	-	-24.4(0.02)	-33.5(0.02)	17.7(0.08)	-0.9(0.2)
CB10t22h	1320	2661.6	2645.5	11.8	6.1	17.8	27.9	53.8	-	-	-	-
CB10t27h	1620	2643.0	2627.2	2.5	6.2	18.3	21.2	-	-24.2(0.06)	-33.2(0.04)	18.0(0.06)	-1.0(0.2)
CB10t27.5h	1650	2628.2	-	-1.0	6.1	18.4	21.0	53.3	-23.9(0.04)	-33.5(0.06)	18.1(0.08)	-1.1(0.2)

*e.g. Mass change between t = 0–5 minutes is calculated as $\Delta m_{t5} = \Delta m_{ft0} - \Delta m_{it5}$.

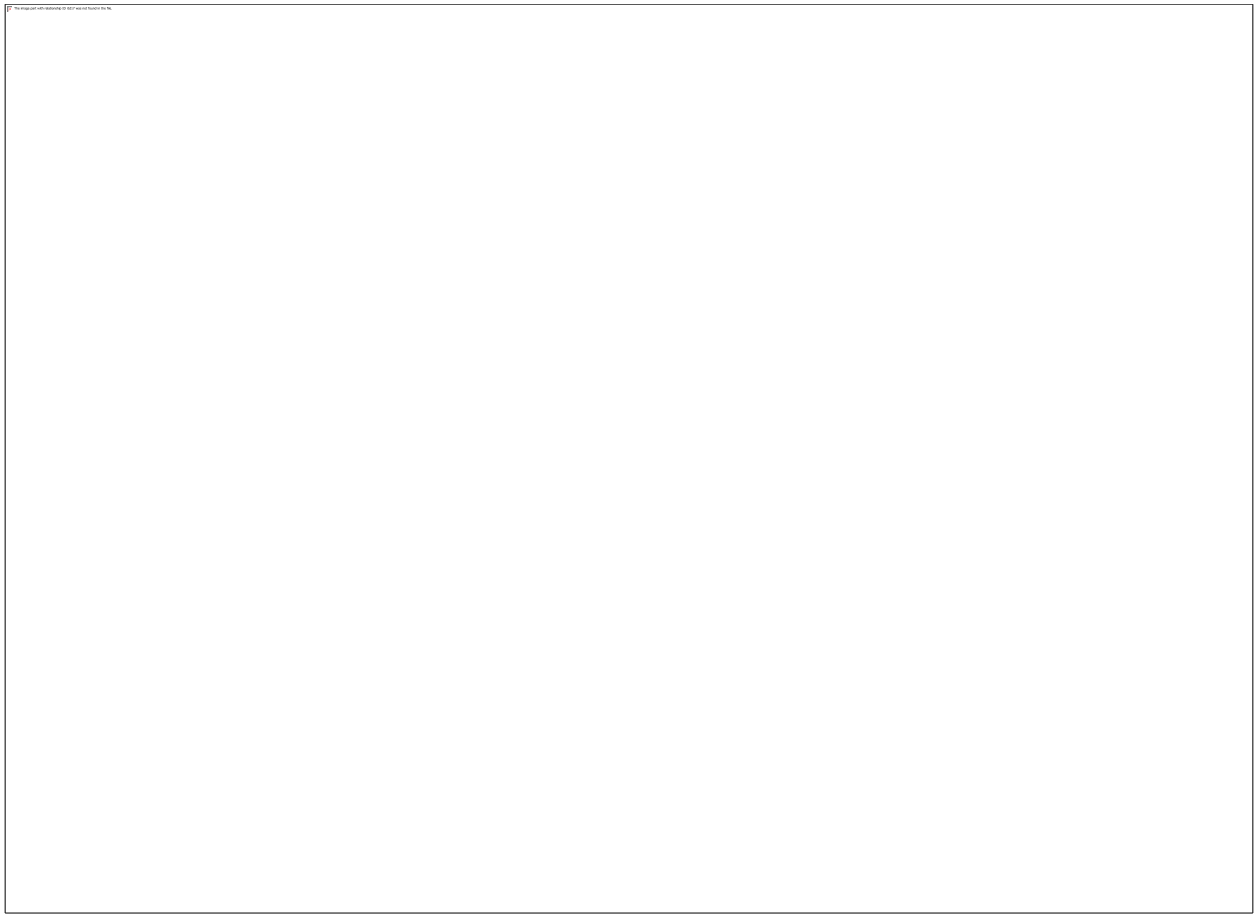

Figure B-3. Ca, Mg, and Si concentrations as a function of time. Analytical errors are smaller than the symbols.

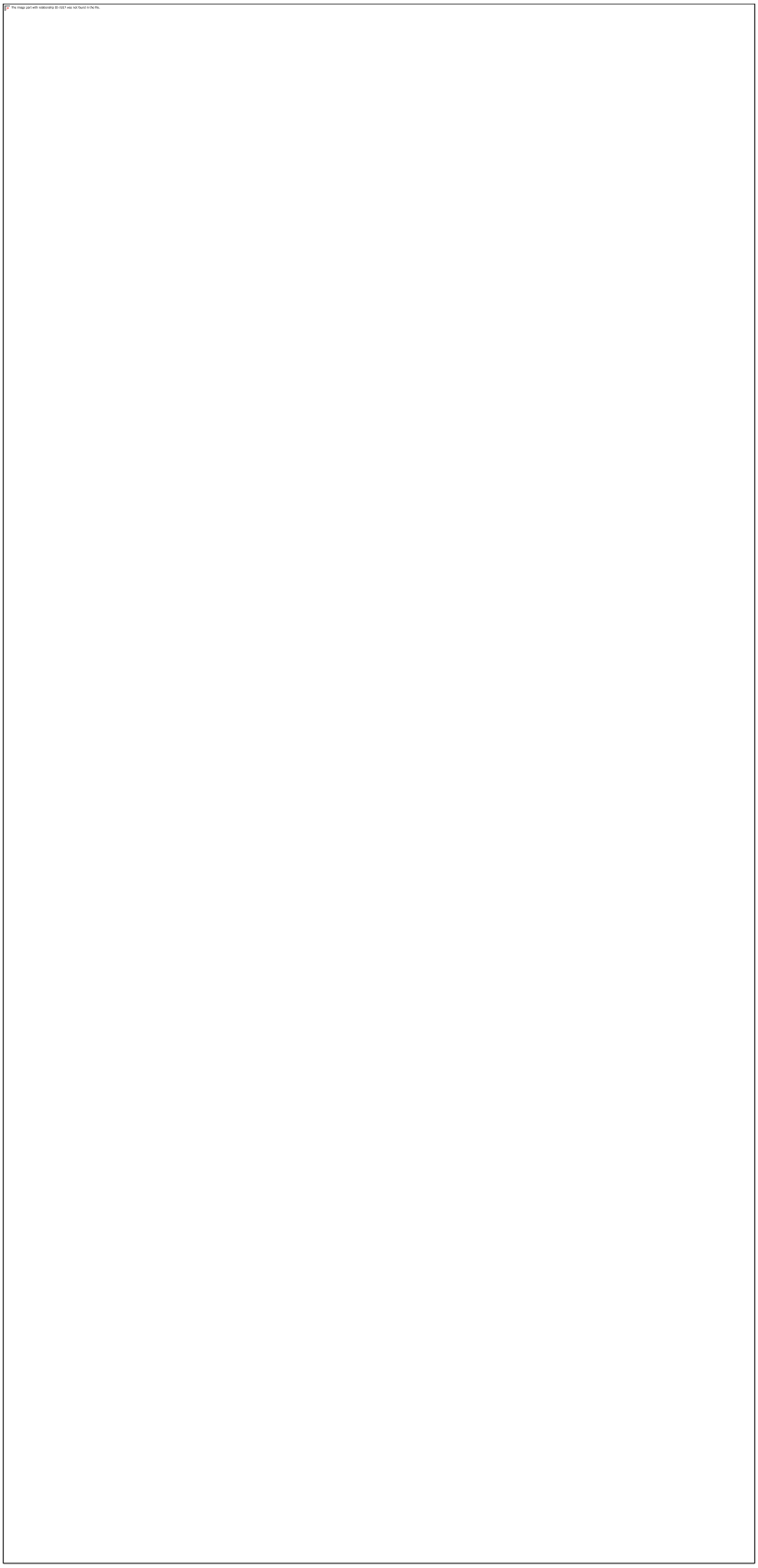

Figure B-4. A: XRD patterns and mineralogy of the precipitates from Experiment CA from t = 0–30 min. At t = 0 min, the only crystalline phase in precipitates is brucite (denoted B). Both brucite

and calcite (denoted C) precipitated from the Experiment CA from *t* = 5–30 min. **B:** XRD patterns and mineralogy of the precipitates from Experiment CA from *t* = 40–180 min **C**: XRD patterns and mineralogy of the precipitates from Experiment CA from *t* = 210 min – 27.5 h. All the precipitates between *t* = 40 min – 27.5 h contains calcite (C) as crystalline phase. Evaporative halite (denoted H) was detected in the precipitates at *t* = 22 h. Figures at the top (**D** and **E**) illustrate the brucite peak at d = 4.766 Å in the XRD patterns of the precipitates at *t* = 25 min and *t* = 30 min.

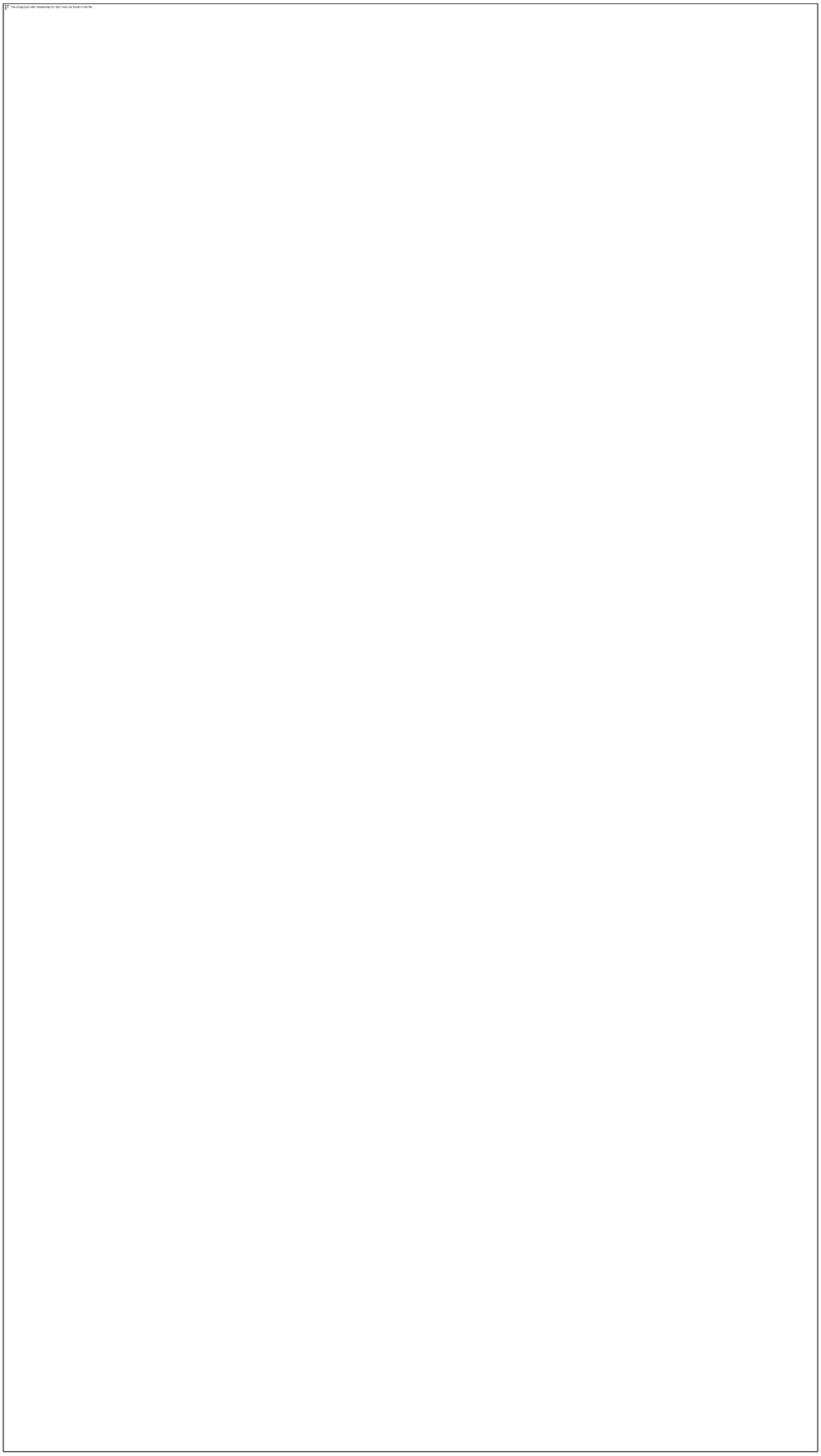

Figure B-5. A: XRD patterns and mineralogy of the precipitates from Experiment CB from t = 0–30 min. At t = 0 min, the only crystalline phase in precipitates is brucite (denoted B). Both brucite

and calcite (denoted C) precipitated from the Experiment CB from t = 5–30 min. **B:** XRD patterns and mineralogy of the precipitates from Experiment CB from t = 40–180 min **C**: XRD patterns and mineralogy of the precipitates from Experiment CB from t = 210 min–27.5 h. All the precipitates between t = 40 min – 27.5 h contains calcite (C) as crystalline phase.

Tables B-9 and B-10 provide a summary of the total yield of precipitate, in units of g/L of FPW, and the weight % (wt%) abundances of brucite and calcite in precipitates as a function of time. In some cases, a minor amount of halite was detected from XRD patterns. In these cases (CA10t20, CA10t25), the amount of halite was normalized out so that $m_{brucite} + m_{calcite} = 100$ wt% in the table below.

Table B-9. Total yield, mineralogy and phase abundance (wt%) of the precipitates from Experiment CA.

Sample ID	Time (min)	Total Yield (g/L)	Brucite (wt%)	Calcite (wt%)	Total (wt%)	R_{wp}* (wt%)
CA10-original			no precipitate			
CA10t0	0	1.68	100.0		100.0	
CA10t5	5	0.55	91.4	8.6	100.0	12.7
CA10t10	10	0.24	57.2	42.8	100.0	11.6
CA10t15	15	1.20	38.9	61.1	100.0	10.5
CA10t20	20	2.38	3.0	97.0	100.0	14.4
CA10t25	25	2.41	3.4	96.6	100.0	26.8
CA10t30	30	2.75	9.3	90.7	100.0	11.8
CA10t40	40	3.24		100.0	100.0	
CA10t50	50	2.85		100.0	100.0	
CA10t60	60	2.52		100.0	100.0	
CA10t90	90	2.24		100.0	100.0	
CA10t120	120	2.03		100.0	100.0	
CA10t150	150	1.90		100.0	100.0	
CA10t180	180	2.56		100.0	100.0	
CA10t210	210	2.44		100.0	100.0	
CA10t240	240	3.03		100.0	100.0	
CA10t270	270	2.97		100.0	100.0	
CA10t330	330	3.16		100.0	100.0	
CA10t480	480	1.77		100.0	100.0	
CA10t22h	1320	2.77		100.0	100.0	
CA10t27h	1620	2.69		100.0	100.0	
CA10t27.5h	1650	3.27		100.0	100.0	

*R_{wp} is the weighted pattern residual, a measure of the quality of the least-squares residual.

Table B-10. Total yield, mineralogy and phase abundance (wt%) of the precipitates from Experiment CB.

Sample ID	Time (min)	Total Yield (g/L)	Brucite (wt%)	Calcite (wt%)	Total (wt%)	R_{wp}* (%)
CB10-original			no precipitate			
CB10t0	0	1.77	100.0		100.0	
CB10t5	5	1.81	92.9	7.1	100.0	14.8
CB10t10	10	2.70	74.7	25.3	100.0	12.8
CB10t15	15	2.28	18.0	82.0	100.0	11.2
CB10t20	20	2.76	7.7	92.3	100.0	16.9
CB10t25	25	3.80	5.2	94.8	100.0	15.2
CB10t30	30	3.66	1.1	98.9	100.0	17.6
CB10t40‡	40	3.43		100.0	100.0	–‡
CB10t50	50	2.69		100.0	100.0	–
CB10t60	60	2.51		100.0	100.0	–
CB10t90	90	2.35		100.0	100.0	–
CB10t120	120	2.79		100.0	100.0	–
CB10t150	150	2.70		100.0	100.0	–
CB10t180	180	2.74		100.0	100.0	–
CB10t210	210	2.82		100.0	100.0	–
CB10t240†	240	1.92		–†	–†	–
CB10t270	270	2.66		100.0	100.0	–
CB10t330	330	3.44		100.0	100.0	–
CB10t480	480	2.82		100.0	100.0	–
CB10t22h	1320	3.37		100.0	100.0	–
CB10t27h	1620	3.14		100.0	100.0	–
CB10t27.5h	1650	2.95		100.0	100.0	–

*R_{wp} is the weighted pattern residual, a function of the least-squares residual.
† Sample was lost prior to XRD analysis
‡ Rietveld refinement with XRD data was not necessary after 40 minutes because samples were monomineralic.

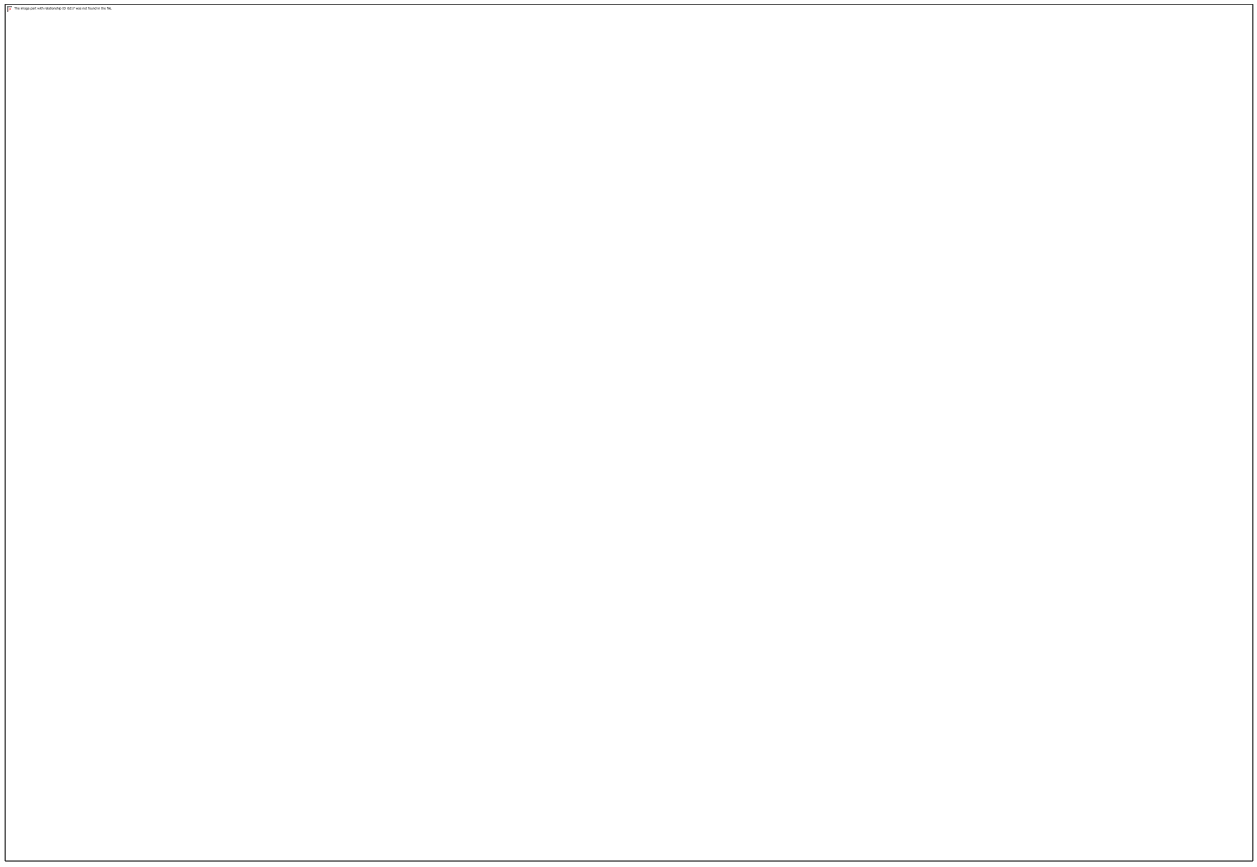

Figure B-6. SEM SE image (A) and EDX spectrum (B) of brucite from Experiment CA at t = 0 min. SEM image (C) and EDX spectrum (D) of calcite precipitate from Experiment CA at t = 240 min. Precipitates from CB have similar morphology and compositions.

A PHREEQC modelling (Figure B-7) was performed to calculate the SI of hydrated Mg-carbonates in solution at t = 90 min for Experiment CA and CB if solution pH were adjusted to more alkaline level. The solution at t = 90 min was chosen for the modelling as the Ca and Mg concentration and pH were plateaued, the mineralogy of precipitates was consistent with respect to experiment time, and the DIC concentration was at its maximum value. The goal of this PHREEQC modelling was to test if the saturation of dypingite, hydromagnesite, and nesquehonite, magnesite can be reached through addition of 1M NaOH during the carbonation experiments. To maintain the supersaturation state of hydromagnesite, dypnigite, and magnesite, the pH of solution

at 90 min in both carbonation experiments is needed to be elevated to ~10.0, ~11.0, and ~7.5, respectively. Dypingite cannot reach saturation by only elevating the pH of solution at 90 min.

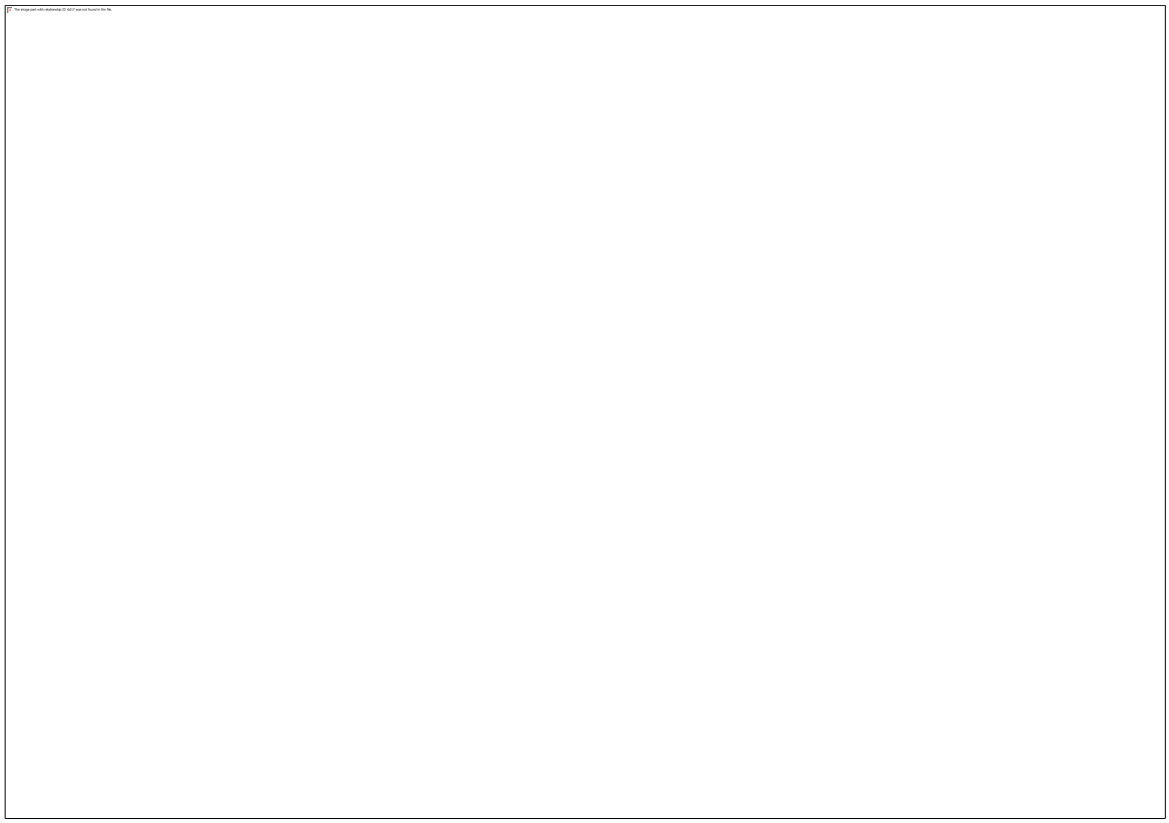

Figure B-7. Saturation indices (modelled using PHREEQC) of Mg-carbonate minerals in solution at t = 90 min for Experiment CA and CB if solution pH were adjusted to greater values.

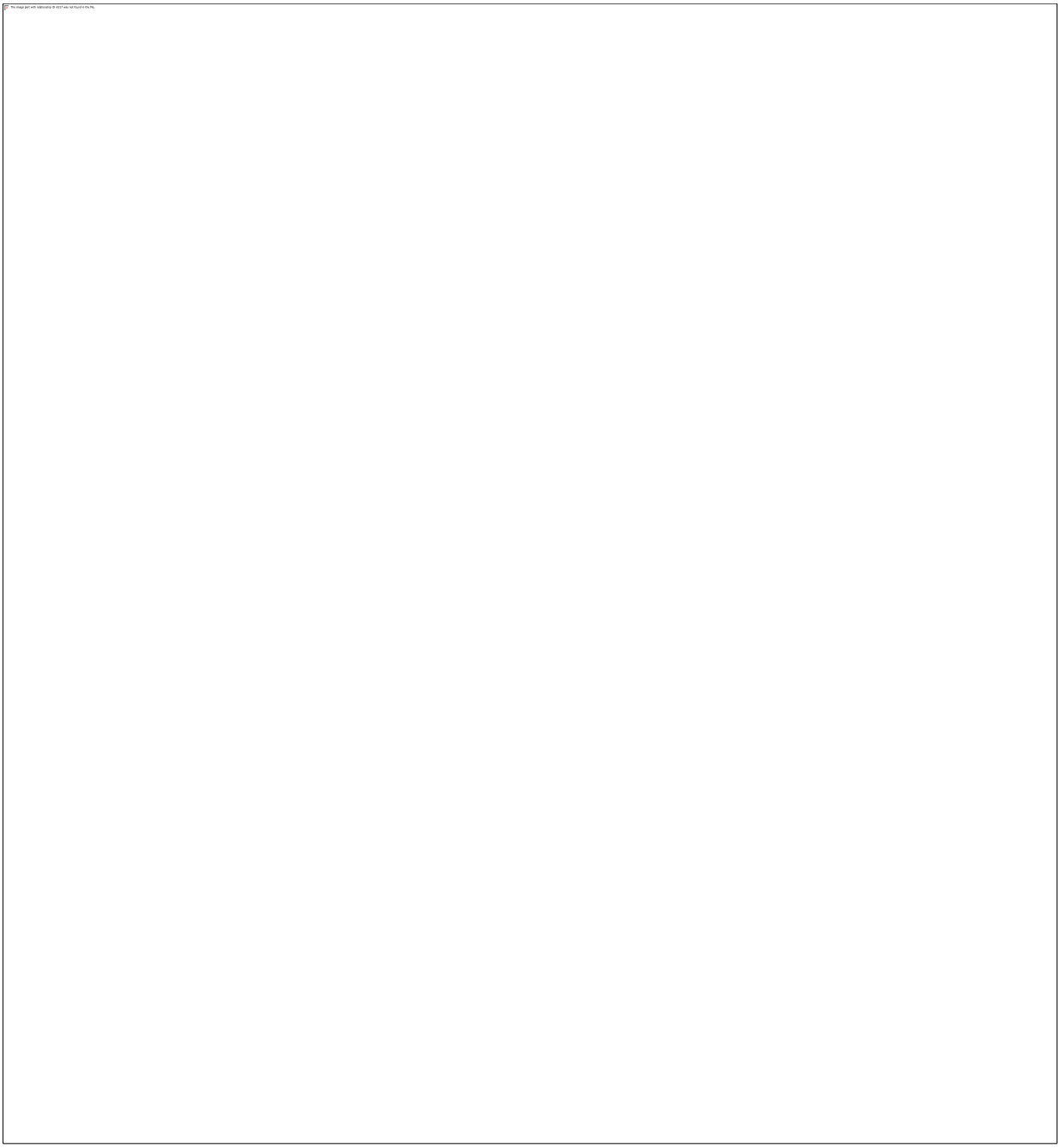

Figure B-8. Evaporative water loss (A) and the total yield of precipitates (B) during the carbonation experiments. The negative evaporative loss in A represents the mass gain due to conversion of gas to mineral precipitates.

B3 References

(1) Bish, D. L; Howard, S. A. Quantitative phase analysis using the Rietveld method. *J. Appl. Crystallogr.* **1988**, *21*, 86–91.

(2) Hill, R. J.; Howard, C. J. Quantitative phase analysis from neutron powder diffraction data using the Rietveld method. *J. Appl. Crystallogr.* **1987**, *20*, 467–474.

(3) Rietveld, H. M. A profile refinement method for nuclear and magnetic structures. *J. Appl. Crystallogr.* **1969**, *2*, 65–71.

(4) Balzar, D.; Audebrand, N.; Daymond, M. R.; Fitch, A.; Hewat, A.; Langford, J. I.; Le Bail, A.; Louër, D.; Masson, O.; McCowan, C. N.; Popa, N. C.; Stephens, P. W.; Toby, B. H. Size-Strain Line-Broadening Analysis of the Ceria Round-Robin Sample. *J. Appl. Crystallogr.* **2004**, 37, 911–924. https://doi.org/10.1107/S0021889804022551.

(5) Zhu, B,; Wilson, S.A.; Zeyen, N.; Raudsepp M.J.; Wang, B.; Rostron, B.J.; Snihur, K.N.; von Guten, K.; Harrison, A.L.; Alessi, D.S.; Hydraulic fracturing flowback and produced water as a feedstock for carbon dioxide removal or emission reduction via mineral carbonation. (In preparation)

(6) Stephens, P.W. Phenomenological model of anisotropic peak broadening in powder diffraction. *J. Appl. Crystallogr*. **1999**, *32*, 281- 289.

(7) Sarazin, G.; Michard, G.; Prevot, F. A rapid and accurate spectroscopic method for alkalinity measurements in sea water samples. *Water Res.* **1999**, *33*, 290–294.

(8) Parkhurst, D. L.; Appelo, C. A. J. *Description of input and examples for PHREEQC Version 3—A computer program for speciation, batch-reaction, one-dimensional transport, and inverse geochemical calculations*; U.S. Geological Survey: Denver, Colorado, 2013.

(9) Haase, C.; Dethlefsen, F.; Ebert, M.; Dahmke, A. Uncertainty in geochemical modelling of CO_2 and calcite dissolution in NaCl solutions due to different modelling codes and thermodynamic databases. *Appl. Geochemistry* **2013**, *33*, 306–317.

(10) Harrison, A. L.; Mavromatis, V.; Oelkers, E. H.; Bénézeth, P. Solubility of the hydrated Mg-carbonates nesquehonite and dypingite from 5 to 35 °C: implications for CO_2 storage and the relative stability of Mg-carbonates. *Chem. Geol*. **2019**, *504*, 123–135

(11) Stoessell, R. K. 25°C and 1 atm dissolution experiments of sepiolite and kerolite. *Geochim. Cosmochim. Acta* **1988**, *52*, 365–374.

APPENDIX C

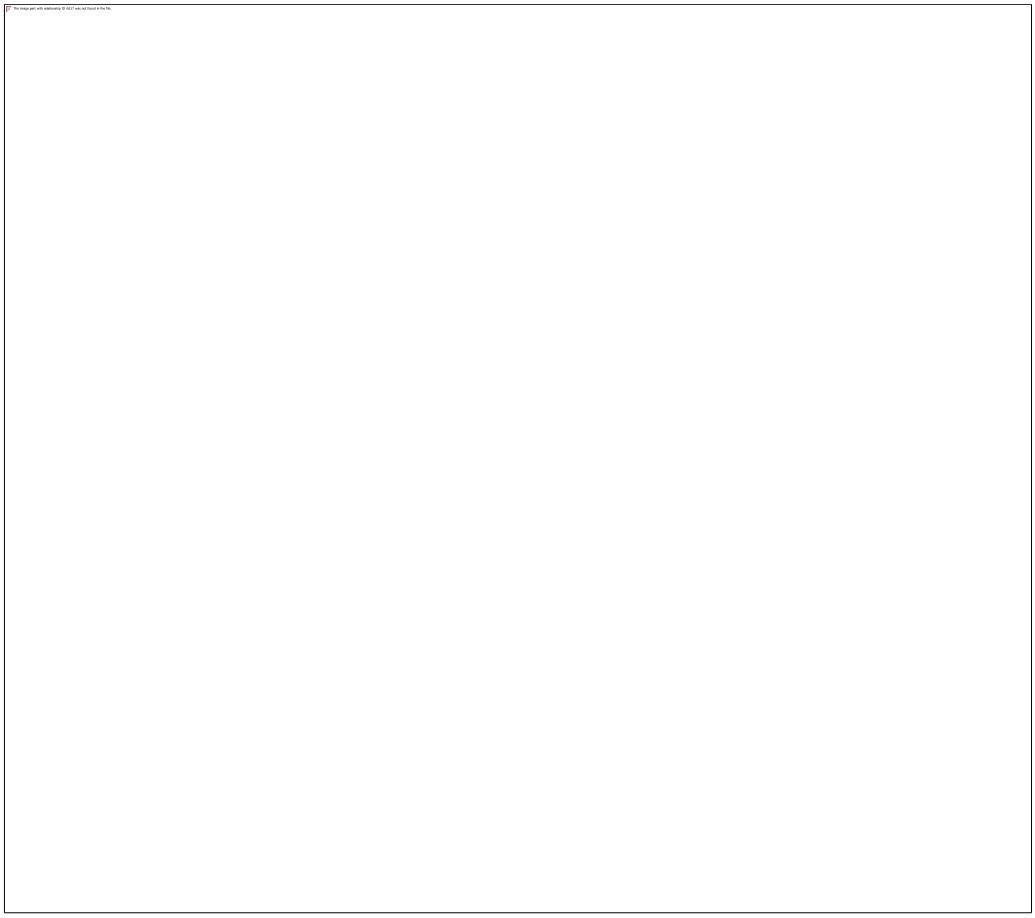

FIGURE C-1. Sensitivity analysis of saturation index in FPW1a samples at pH 10 using phreeqc.dat. The plot shows the change in saturation index of minerals with respect to NaCl concentration. The concentration of other elements in the analysis remans consistent with the original FPW1a. The sensitivity analysis using PHREEQC shows that the salt concentration in aqueous solution affect the saturation state of mineral phases. The saturation index of Mg- and Ca-hydroxides and carbonates, and hydrated Mg- carbonates increase in saltier solutions. The saturation index of Mn- hydroxides (manganite) has a slight decrease as the solution is saltier. The phenomenon of becoming supersaturation in salty solution is refer to as “salt-out” effect, which is due to the increasing of cation activities (Zermeno-Motante et al., 2016).

Transition metals detected in both solutions are Co (0.05 ± 0.01 ppm), Mn (3.5 ± 0.1 ppm), Pb (0.09 ± 0.0006 ppm in CA and 0.08 ± 0.006 ppm in CB), and Zn (2.0 ± 0.1 in CA and 2.3 ± 0.1 in CB). Ti concentration is closed to the detection limit in CA (0.3 ± 0.6 ppm) and is below detection limit (< 0.03 ppm) in CB. Anionic elements in the solutions are Br (242.6 ± 7.1 ppm in CA and 229.8 ± 5.2 ppm in CB), S (59.7 ± 0.4 ppm in CA and 56.2 ± 1.4 ppm in CB), and Si (12.6 ± 0.4 ppm in CA and 11.5 ± 0.4 ppm in CB). The concentrations of S in the solutions after titration were 53.3 ± 4.4 ppm and 48.8 ± 1.5 ppm in CA and CB, respectively. It decreased dramatically from *t* = 0–60 min and the trend of decreased slowed down from *t* = 60–180 min. The value of S concentration stabilized at 35.1 ± 1.8 ppm when time reaches 180 min in Experiment CA and at 32.5 ±1.6 ppm when the experiment reaches 150 min.

The concentration of Mn, Zn, and Pb in FPW decreased immediately after adding 1M NaOH to the solutions and as both carbonation experiments progressed, compared to the value in original FPW. The concentrations of Mn were equal to or below detection limit (0.5 ppm) from *t* = 0–1650 min in CA and from *t* = 0–480 min in CB. From *t* = 1320–1650 in CB, the concentrations of Mn in solutions ranged from 0.6–0.7 ppm, which is slightly above the detection limit. The concentrations of Zn during both CA and CB were below detection limit, which ranges from 1.5–1.6 ppm, and those of Pb during both experiments were below 0.05 ppm. The concentrations of other elements can refer to Table C-1,C-2.

Five samples of precipitates (Table C-3), including the precipitates formed from CA at *t* = 0 min, 50 min, 150 min, 330 min, and 1650 min and from CB at t = 1650 min, were digested and analyzed with ICP-MS for the concentration of trace elements. Unfortunately, the precipitates from CB at *t* = 0, 50, 150 and 330 min were lost during sample preparation, therefore it is not possible to compare the composition of trace elements in the precipitates from the duplicated experiments. The results from the ICP-MS indicates metal cations such as Mn (8,790 ± 90 ppm), Fe (900 ± 39

ppm), Cu (81.0 ± 8.9 ppm), Zn (2,010 ± 90 ppm), Sr (164 ± 3 ppm), Ba (13.4 ± 4.6 ppm) and Pb (67.5 ± 0.2 ppm) were trapped in the precipitates at t = 0 min, when the pH value of solutions was at 10.4. After supplying CO_2 and as the pH decreased during experiments, the concentrations of Li (150–159 ppm), Sr (19,600–24,300 ppm), Ba (178–272 ppm) increased in the precipitates from CA at t = 0, 50, 150, and 1650 min. In comparison, the concentrations of Mn (2,180–2,260 ppm), Fe (201–283 ppm), Cu (5.6–17.5 ppm), Zn (458–664 ppm), Pb (23.2–28.6 ppm) decreased in the precipitates from CA at t = 0, 50, 150, and 1650 min. The concentrations of Li (152 ± 5 ppm), Mn (24,700 ± 100 ppm), Fe (290 ± 12 ppm), Zn (659 ± 24 ppm), Sr (25,800 ± 500 ppm), Ba (264 ± 7 ppm) and Pb (27.0 ± 0.4 ppm) the precipitates from CB at t = 1650 min are consistent with the precipitates in general from CA at t = 1650 min. In addition, Ti, Cr, Co, As, Cd, and Ni are not detected in the precipitates from both experiments, which is consistent with the results that those elements are not detectable in the original FPW.

Table C-1. Concentrations (conc.) of elements in FPW as a function of time in Experiment CA based on ICP-MS analysis. Errors are reported as 1σ. Detection limit (DL) is sample-specific. BDL: below detection limit.

T (min)	Li			B			Mg			Al			Si			K		
	Conc. (ppm)	Error (ppm)	DL (ppm)	Conc. (ppm)	Error (ppm)	DL (ppm)	Conc. (ppm)	Error (ppm)	DL (ppm)	Conc. (ppm)	Error (ppm)	DL (ppm)	Conc. (ppm)	Error (ppm)	DL (ppm)	Conc. (ppm)	Error (ppm)	DL (ppm)
0	31.0	0.4	18.8	53.8	0.2	9.7	210.2	6.1	82.2	BDL		2.7	BDL		5.6	1643.7	62.0	84.8
5	33.6	0.3	18.6	57.9	0.5	9.6	331.4	15.5	81.5	BDL		2.7	BDL		5.5	1606.3	56.3	84.1
10	31.3	0.3	18.7	53.7	0.2	9.7	511.9	17.0	81.9	BDL		2.7	BDL		5.5	1616.6	64.3	84.5
15	28.6	0.5	18.5	48.9	0.3	9.6	522.8	23.0	81.1	BDL		2.7	BDL		5.5	1514.3	63.0	83.7
20	31.8	0.3	18.5	53.0	1.3	9.5	620.2	21.5	80.9	BDL		2.7	BDL		5.5	1629.3	70.8	83.5
25	37.4	0.8	18.8	61.7	1.3	9.7	662.3	21.6	82.2	BDL		2.7	BDL		5.6	1704.2	52.9	84.8
30	32.3	0.2	18.6	57.7	0.5	9.6	677.7	20.1	81.7	BDL		2.7	7.8	0.2	5.5	1694.3	58.2	84.3
40	31.1	0.2	18.8	58.8	0.8	9.7	720.4	17.4	82.4	BDL		2.7	8.9	0.5	5.6	1620.0	59.9	85.0
50	32.4	0.2	18.7	60.8	0.1	9.7	741.4	21.5	82.1	BDL		2.7	9.6	0.5	5.5	1696.9	52.7	84.8
60	30.4	0.4	18.6	57.4	0.5	9.6	690.8	25.8	81.5	BDL		2.7	8.3	0.5	5.5	1569.6	50.2	84.1
90	30.8	0.2	18.6	61.5	0.7	9.6	737.0	34.3	81.4	BDL		2.7	11.9	0.6	5.5	1658.5	66.3	84.0
120	27.3	0.3	18.6	51.7	0.6	9.6	720.3	26.0	81.3	BDL		2.7	9.3	0.2	5.5	1640.8	65.9	84.0
150	30.1	0.4	18.7	57.3	0.8	9.7	704.6	22.0	81.9	BDL		2.7	9.5	0.4	5.5	1598.7	58.4	84.5
180	29.9	0.4	18.7	57.0	1.0	9.7	708.2	25.1	82.0	BDL		2.7	8.7	0.5	5.5	1596.3	45.5	84.7
210	28.9	0.2	18.6	54.9	0.3	9.6	680.9	20.0	81.6	BDL		2.7	8.3	0.4	5.5	1562.4	49.7	84.2
240	29.7	0.2	18.8	56.5	0.5	9.7	702.5	26.2	82.4	BDL		2.7	10.8	0.2	5.6	1583.8	47.1	85.0
270	28.6	0.3	18.8	56.1	0.7	9.7	700.6	22.8	82.5	BDL		2.7	9.0	0.4	5.6	1599.7	59.0	85.1
330	30.8	0.6	19.2	59.2	1.1	9.9	712.9	21.9	84.0	BDL		2.8	9.2	0.8	5.7	1642.2	52.9	86.7
480	32.4	0.5	18.6	63.0	1.2	9.6	709.0	23.4	81.5	BDL		2.7	9.5	0.6	5.5	1607.3	42.1	84.1
1320	34.8	0.3	18.9	66.0	1.0	9.7	741.5	28.8	82.7	BDL		2.7	11.3	0.6	5.6	1704.2	58.1	85.3
1620	31.2	0.3	18.8	60.3	0.4	9.7	733.5	26.0	82.3	BDL		2.7	10.1	0.5	5.6	1690.3	55.7	85.0
1650	31.3	0.1	18.7	60.3	0.3	9.6	725.1	21.8	81.7	BDL		2.7	10.9	0.0	5.5	1648.9	59.6	84.3

Table C-1 (Continued). Concentrations (conc.) of elements in FPW as a function of time in Experiment CA based on ICP-MS analysis. Errors are reported as 1σ. Detection limit (DL) is sample-specific. BDL: below detection limit.

T (min)	P			S			Ca			Ti			Cr			Mn		
	Conc. (ppm)	Error (ppm)	DL (ppm)	Conc. (ppm)	Error (ppm)	DL (ppm)	Conc. (ppm)	Error (ppm)	DL (ppm)	Conc. (ppm)	Error (ppm)	DL (ppm)	Conc. (ppm)	Error (ppm)	DL (ppm)	Conc. (ppm)	Error (ppm)	DL (ppm)
0	BDL		6.6	53.3	4.0	25.2	9360.7	160.2	85.6	BDL		0.3	BDL		0.7	BDL		0.5
5	BDL		6.5	49.9	1.2	24.9	9036.8	91.6	84.8	BDL		0.3	BDL		0.7	BDL		0.5
10	BDL		6.5	48.9	1.8	25.1	8628.9	69.5	85.3	BDL		0.3	BDL		0.7	BDL		0.5
15	BDL		6.5	46.2	0.7	24.8	7670.9	107.1	84.4	BDL		0.3	BDL		0.7	BDL		0.5
20	BDL		6.5	49.4	1.2	24.8	8245.7	76.7	84.3	BDL		0.3	BDL		0.7	BDL		0.5
25	BDL		6.6	48.3	1.1	25.2	8323.4	103.4	85.6	BDL		0.3	BDL		0.7	BDL		0.5
30	BDL		6.5	48.5	1.3	25.0	8251.4	109.1	85.0	0.4	0.6	0.3	BDL		0.7	BDL		0.5
40	BDL		6.6	41.0	1.3	25.2	7798.9	186.2	85.8	0.4	0.6	0.3	BDL		0.7	BDL		0.5
50	BDL		6.6	40.2	1.7	25.1	7984.0	11.8	85.5	0.4	0.3	0.3	BDL		0.7	BDL		0.5
60	BDL		6.5	36.8	1.4	25.0	7630.0	137.4	84.9	BDL		0.3	BDL		0.7	BDL		0.5
90	BDL		6.5	40.2	1.8	24.9	7964.0	177.3	84.8	BDL		0.3	BDL		0.7	BDL		0.5
120	BDL		6.5	39.0	0.9	24.9	7814.8	15.1	84.7	0.3	0.6	0.3	BDL		0.7	BDL		0.5
150	BDL		6.5	37.7	1.0	25.1	7624.5	152.6	85.3	0.4	0.6	0.3	BDL		0.7	BDL		0.5
180	BDL		6.6	33.5	0.7	25.1	7642.9	101.9	85.4	0.4	0.6	0.3	BDL		0.7	BDL		0.5
210	BDL		6.5	35.6	1.3	25.0	7368.7	92.0	85.0	BDL		0.3	BDL		0.7	BDL		0.5
240	BDL		6.6	36.0	0.3	25.2	8213.2	138.8	85.8	0.3	0.6	0.3	BDL		0.7	BDL		0.5
270	BDL		6.6	37.1	1.4	25.2	7538.0	81.1	85.9	0.3	0.6	0.3	BDL		0.7	BDL		0.5
330	BDL		6.7	34.6	0.2	25.7	7746.1	111.6	87.5	BDL		0.3	BDL		0.7	BDL		0.5
480	BDL		6.5	33.1	2.4	24.9	7759.3	167.2	84.8	0.3	0.6	0.3	BDL		0.7	BDL		0.5
1320	BDL		6.6	36.3	1.3	25.3	8058.7	87.7	86.1	0.5	0.8	0.3	BDL		0.7	BDL		0.5
1620	BDL		6.6	35.2	2.0	25.2	7944.5	76.2	85.7	BDL		0.3	BDL		0.7	0.5	0.0	0.5
1650	BDL		6.5	34.3	0.7	25.0	8031.2	165.6	85.1	0.4	0.6	0.3	BDL		0.7	0.5	0.0	0.5

Table C-1 (Continued). Concentrations (conc.) of elements in FPW as a function of time in Experiment CA based on ICP-MS analysis. Errors are reported as 1σ. Detection limit (DL) is sample-specific. BDL: below detection limit.

T (min)	Fe			Co			Ni			Cu			Zn			Br		
	Conc. (ppm)	Error (ppm)	DL (ppm)	Conc. (ppm)	Error (ppm)	DL (ppm)	Conc. (ppm)	Error (ppm)	DL (ppm)	Conc. (ppm)	Error (ppm)	DL (ppm)	Conc. (ppm)	Error (ppm)	DL (ppm)	Conc. (ppm)	Error (ppm)	DL (ppm)
0	BDL		3.5	0.05	0.02	0.06	BDL		2.9	BDL		0.9	BDL		1.6	223.1	5.4	36.2
5	BDL		3.5	0.05	0.01	0.06	BDL		2.9	BDL		0.9	BDL		1.6	214.4	6.9	35.9
10	BDL		3.5	0.05	0.01	0.06	BDL		2.9	BDL		0.9	BDL		1.6	217.5	12.8	36.1
15	BDL		3.5	0.05	0.02	0.06	BDL		2.9	BDL		0.9	BDL		1.5	202.3	7.0	35.8
20	BDL		3.5	0.05	0.01	0.06	BDL		2.9	BDL		0.9	BDL		1.5	210.4	7.1	35.7
25	BDL		3.5	0.05	0.03	0.06	BDL		2.9	BDL		0.9	BDL		1.6	214.4	9.5	36.2
30	BDL		3.5	0.05	0.02	0.06	BDL		2.9	BDL		0.9	BDL		1.6	220.0	10.0	36.0
40	BDL		3.5	0.05	0.02	0.06	BDL		2.9	BDL		0.9	BDL		1.6	214.8	3.3	36.3
50	BDL		3.5	0.05	0.01	0.06	BDL		2.9	BDL		0.9	BDL		1.6	213.5	6.4	36.2
60	BDL		3.5	0.05	0.00	0.06	BDL		2.9	BDL		0.9	BDL		1.6	205.0	8.6	36.0
90	BDL		3.5	0.05	0.00	0.06	BDL		2.9	BDL		0.9	BDL		1.6	214.1	12.0	35.9
120	BDL		3.5	0.05	0.01	0.06	BDL		2.9	BDL		0.9	BDL		1.6	212.5	5.9	35.9
150	BDL		3.5	0.05	0.00	0.06	BDL		2.9	BDL		0.9	BDL		1.6	206.6	3.5	36.1
180	BDL		3.5	0.05	0.01	0.06	BDL		2.9	BDL		0.9	BDL		1.6	203.1	3.5	36.2
210	BDL		3.5	0.05	0.01	0.06	BDL		2.9	BDL		0.9	BDL		1.6	199.4	3.4	36.0
240	BDL		3.5	0.05	0.00	0.06	BDL		2.9	BDL		0.9	BDL		1.6	203.4	7.4	36.3
270	BDL		3.5	0.05	0.01	0.06	BDL		2.9	BDL		0.9	BDL		1.6	205.2	3.4	36.4
330	BDL		3.6	0.05	0.00	0.06	BDL		3.0	BDL		0.9	BDL		1.6	208.2	3.8	37.0
480	BDL		3.5	0.05	0.02	0.06	BDL		2.9	BDL		0.9	BDL		1.6	207.7	3.2	35.9
1320	BDL		3.6	0.05	0.01	0.06	BDL		2.9	BDL		0.9	BDL		1.6	223.7	4.6	36.4
1620	BDL		3.5	0.05	0.01	0.06	BDL		2.9	BDL		0.9	BDL		1.6	223.2	4.3	36.3
1650	BDL		3.5	0.05	0.01	0.06	BDL		2.9	BDL		0.9	BDL		1.6	208.8	6.5	36.0

Table C-1 (Continued). Concentrations (conc.) of elements in FPW as a function of time in Experiment CA based on ICP-MS analysis. Errors are reported as 1σ. Detection limit (DL) is sample-specific. BDL: below detection limit.

T (min)	Sr			As			Ba			Pb		
	Conc. (ppm)	Error (ppm)	DL (ppm)	Conc. (ppm)	Error (ppm)	DL (ppm)	Conc. (ppm)	Error (ppm)	DL (ppm)	Conc. (ppm)	Error (ppm)	DL (ppm)
0	860.2	15.1	20.9	BDL		1.2	3.6	0.1	1.3	BDL		0.05
5	831.4	33.1	20.7	BDL		1.2	3.4	0.2	1.3	BDL		0.05
10	830.1	26.0	20.8	BDL		1.2	3.3	0.1	1.3	BDL		0.05
15	789.9	32.2	20.6	BDL		1.2	3.1	0.2	1.3	BDL		0.05
20	807.2	22.9	20.6	BDL		1.2	3.1	0.1	1.3	BDL		0.05
25	811.9	21.0	20.9	BDL		1.2	3.1	0.1	1.3	BDL		0.05
30	832.3	22.5	20.8	BDL		1.2	3.1	0.2	1.3	BDL		0.05
40	816.7	19.7	20.9	BDL		1.3	3.4	0.1	1.3	BDL		0.05
50	835.9	19.8	20.9	BDL		1.2	3.4	0.1	1.3	BDL		0.05
60	804.5	23.4	20.7	BDL		1.2	3.2	0.1	1.3	BDL		0.05
90	836.8	32.5	20.7	BDL		1.2	3.4	0.1	1.3	BDL		0.05
120	826.5	22.5	20.7	BDL		1.2	3.3	0.1	1.3	BDL		0.05
150	815.4	17.4	20.8	BDL		1.2	3.4	0.2	1.3	BDL		0.05
180	796.1	22.9	20.9	BDL		1.2	3.3	0.1	1.3	BDL		0.05
210	794.5	16.4	20.8	BDL		1.2	3.3	0.1	1.3	BDL		0.05
240	817.4	25.9	21.0	BDL		1.3	3.3	0.1	1.3	BDL		0.05
270	813.2	21.3	21.0	BDL		1.3	3.3	0.1	1.3	BDL		0.05
330	822.7	16.1	21.4	BDL		1.3	3.3	0.1	1.4	BDL		0.05
480	819.2	22.3	20.7	BDL		1.2	3.3	0.1	1.3	BDL		0.05
1320	862.9	19.4	21.0	BDL		1.3	3.5	0.2	1.3	BDL		0.05
1620	861.6	24.9	20.9	BDL		1.3	3.4	0.3	1.3	BDL		0.05
1650	820.5	19.1	20.8	BDL		1.2	3.4	0.0	1.3	BDL		0.05

Table C-2. Concentrations (conc.) of elements in FPW as a function of time in Experiment CB based on ICP-MS analysis. Errors are reported as 1σ. Detection limit (DL) is sample-specific. BDL: below detection limit.

	Li			B			Mg			Al			Si			K		
T (min)	Conc. (ppm)	Error (ppm)	DL (ppm)	Conc. (ppm)	Error (ppm)	DL (ppm)	Conc. (ppm)	Error (ppm)	DL (ppm)	Conc. (ppm)	Error (ppm)	DL (ppm)	Conc. (ppm)	Error (ppm)	DL (ppm)	Conc. (ppm)	Error (ppm)	DL (ppm)
0	30.2	0.4	18.7	53.3	0.4	9.6	214.2	7.8	81.8	BDL		2.7	BDL		5.5	1631.0	51.8	84.4
5	30.6	0.3	19.0	56.2	0.7	9.8	339.8	13.1	83.0	BDL		2.7	BDL		5.6	1634.4	43.5	85.7
10	32.7	0.3	18.4	59.9	0.2	9.5	409.9	11.4	80.7	BDL		2.7	BDL		5.5	1614.2	66.1	83.3
15	28.2	0.2	19.0	51.7	0.5	9.8	538.2	17.3	83.3	BDL		2.8	BDL		5.6	1571.8	40.4	85.9
20	29.2	0.2	19.0	51.2	0.5	9.8	616.5	33.8	83.4	BDL		2.8	BDL		5.6	1592.8	45.7	86.0
25	32.0	0.2	19.0	56.5	0.6	9.8	696.6	19.2	83.1	BDL		2.7	BDL		5.6	1751.9	82.2	85.8
30	28.3	0.6	18.5	54.7	0.8	9.6	660.0	23.7	81.0	BDL		2.7	6.8	0.3	5.5	1563.4	47.9	83.6
40	31.6	0.3	18.8	62.8	0.2	9.7	680.9	16.9	82.3	BDL		2.7	8.7	0.5	5.6	1562.9	56.3	85.0
50	27.2	0.6	18.9	54.1	1.6	9.8	723.9	17.4	82.8	BDL		2.7	9.5	0.4	5.6	1691.5	40.3	85.4
60	32.3	0.2	18.7	64.9	0.3	9.7	722.2	34.9	82.0	BDL		2.7	9.5	0.1	5.5	1649.5	42.4	84.7
90	29.1	0.3	18.6	60.2	0.1	9.6	708.0	36.5	81.5	BDL		2.7	9.9	0.1	5.5	1609.1	76.9	84.1
120	29.7	0.2	18.7	59.1	0.4	9.7	705.2	26.0	82.1	BDL		2.7	10.2	0.6	5.5	1625.3	91.3	84.8
150	28.0	0.0	18.4	56.8	0.3	9.5	656.1	23.7	80.6	BDL		2.7	10.2	0.2	5.4	1520.5	61.7	83.1
180	27.4	0.6	18.8	56.7	0.4	9.7	679.6	32.3	82.4	BDL		2.7	9.8	0.2	5.6	1548.0	51.7	85.0
210	27.5	0.4	18.7	57.0	0.8	9.7	683.1	33.1	81.9	BDL		2.7	10.0	0.2	5.5	1555.9	71.4	84.5
240	29.3	0.4	19.2	60.1	0.7	9.9	707.8	25.5	83.9	BDL		2.8	10.0	0.1	5.7	1617.6	80.5	86.6
270	29.7	0.2	18.9	59.4	1.1	9.8	707.6	27.9	83.0	BDL		2.7	9.0	0.3	5.6	1609.5	62.2	85.6
330	29.0	0.4	18.5	56.6	0.6	9.5	696.8	24.2	80.8	BDL		2.7	10.0	0.6	5.5	1596.5	74.6	83.4
480	32.6	0.2	18.6	65.3	0.6	9.6	706.3	27.1	81.5	BDL		2.7	10.4	0.4	5.5	1619.1	41.6	84.1
1320	22.3	0.1	18.6	48.4	0.6	9.6	686.2	19.8	81.7	BDL		2.7	10.3	0.1	5.5	1591.0	55.4	84.3
1620	28.0	0.1	19.2	57.4	0.6	9.9	690.9	27.0	84.0	BDL		2.8	10.0	0.2	5.7	1576.3	53.8	86.7
1650	28.4	0.2	18.9	57.4	0.6	9.8	699.3	27.9	82.9	BDL		2.7	9.4	0.5	5.6	1588.4	64.7	85.5

Table C-2 (Continued). Concentrations (conc.) of elements in FPW as a function of time in Experiment CB based on ICP-MS analysis. Errors are reported as 1σ. Detection limit (DL) is sample-specific. BDL: below detection limit.

	P			S			Ca			Ti			Cr			Mn		
T (min)	Conc. (ppm)	Error (ppm)	DL (ppm)	Conc. (ppm)	Error (ppm)	DL (ppm)	Conc. (ppm)	Error (ppm)	DL (ppm)	Conc. (ppm)	Error (ppm)	DL (ppm)	Conc. (ppm)	Error (ppm)	DL (ppm)	Conc. (ppm)	Error (ppm)	DL (ppm)
0	BDL		6.5	48.8	1.5	25.0	8953.7	111.6	85.1	0.3	0.6	0.3	BDL		0.7	BDL		0.5
5	BDL		6.6	45.0	2.2	25.4	8709.1	8.2	86.5	BDL		0.3	BDL		0.7	BDL		0.5
10	BDL		6.4	47.4	0.5	24.7	8431.2	64.2	84.1	0.3		0.3	BDL		0.7	BDL		0.5
15	BDL		6.6	41.9	1.1	25.5	7917.5	72.7	86.7	0.4	0.6	0.3	BDL		0.7	BDL		0.5
20	BDL		6.7	45.0	1.6	25.5	8031.8	220.2	86.8	BDL		0.3	BDL		0.7	BDL		0.5
25	BDL		6.6	45.2	0.6	25.4	8089.8	85.6	86.6	BDL		0.3	BDL		0.7	BDL		0.5
30	BDL		6.5	33.1	1.5	24.8	7659.8	57.4	84.4	BDL		0.3	BDL		0.7	BDL		0.5
40	BDL		6.6	37.3	0.6	25.2	7346.7	78.1	85.7	BDL		0.3	BDL		0.7	BDL		0.5
50	BDL		6.6	42.2	0.7	25.3	8114.8	82.5	86.2	BDL		0.3	BDL		0.7	BDL		0.5
60	BDL		6.6	35.5	1.0	25.1	7746.9	118.6	85.4	BDL		0.3	BDL		0.7	BDL		0.5
90	BDL		6.5	36.8	0.7	24.9	7739.3	49.5	84.8	BDL		0.3	BDL		0.7	BDL		0.5
120	BDL		6.6	36.9	0.7	25.1	7824.4	79.6	85.5	0.3	0.6	0.3	BDL		0.7	BDL		0.5
150	BDL		6.4	33.2	1.7	24.7	7810.7	41.6	83.9	BDL		0.3	BDL		0.7	BDL		0.5
180	BDL		6.6	34.1	1.3	25.2	7406.0	80.9	85.8	BDL		0.3	BDL		0.7	BDL		0.5
210	BDL		6.5	33.3	0.8	25.1	7511.8	37.5	85.3	BDL		0.3	BDL		0.7	BDL		0.5
240	BDL		6.7	32.6	1.2	25.7	7719.5	155.3	87.4	0.4	0.6	0.3	BDL		0.7	BDL		0.5
270	BDL		6.6	31.9	0.4	25.4	7553.3	107.4	86.4	0.3	0.6	0.3	BDL		0.7	BDL		0.5
330	BDL		6.5	29.8	0.1	24.7	7493.9	150.6	84.2	0.4	0.3	0.3	BDL		0.7	BDL		0.5
480	BDL		6.5	31.9	1.1	24.9	7677.1	65.2	84.8	0.4	0.6	0.3	BDL		0.7	BDL		0.5
1320	BDL		6.5	34.2	1.7	25.0	7907.7	48.6	85.0	0.3	0.6	0.3	BDL		0.7	0.6	0.0	0.5
1620	BDL		6.7	33.6	2.1	25.7	7646.5	17.1	87.5	BDL		0.3	BDL		0.7	0.7	0.0	0.5
1650	BDL		6.6	29.9	1.4	25.4	7583.2	100.9	86.3	0.4	0.6	0.3	BDL		0.7	0.7	0.0	0.5

Table C-2 (Continued). Concentrations (conc.) of elements in FPW as a function of time in Experiment CB based on ICP-MS analysis. Errors are reported as 1σ. Detection limit (DL) is sample-specific. BDL: below detection limit.

T (min)	Fe			Co			Ni			Cu			Zn			Br		
	Conc. (ppm)	Error (ppm)	DL (ppm)	Conc. (ppm)	Error (ppm)	DL (ppm)	Conc. (ppm)	Error (ppm)	DL (ppm)	Conc. (ppm)	Error (ppm)	DL (ppm)	Conc. (ppm)	Error (ppm)	DL (ppm)	Conc. (ppm)	Error (ppm)	DL (ppm)
0	BDL		3.5	0.05	0.03	0.06	BDL		2.9	BDL		0.9	BDL		1.6	211.4	7.5	36.1
5	BDL		3.6	0.05	0.01	0.06	BDL		3.0	BDL		0.9	BDL		1.6	218.6	9.4	36.6
10	BDL		3.5	0.05	0.03	0.06	BDL		2.9	BDL		0.9	BDL		1.5	210.1	5.0	35.6
15	BDL		3.6	0.05	0.01	0.06	BDL		3.0	BDL		0.9	BDL		1.6	206.1	8.8	36.7
20	BDL		3.6	0.05	0.00	0.06	BDL		3.0	BDL		0.9	BDL		1.6	208.4	10.9	36.8
25	BDL		3.6	0.05	0.01	0.06	BDL		3.0	BDL		0.9	BDL		1.6	223.4	10.9	36.7
30	BDL		3.5	0.05	0.01	0.06	BDL		2.9	BDL		0.9	BDL		1.5	199.5	2.7	35.7
40	BDL		3.5	0.05	0.02	0.06	BDL		2.9	BDL		0.9	BDL		1.6	203.6	3.5	36.3
50	BDL		3.6	0.05	0.01	0.06	BDL		3.0	BDL		0.9	BDL		1.6	193.8	3.6	36.5
60	BDL		3.5	0.05	0.02	0.06	BDL		2.9	BDL		0.9	BDL		1.6	209.8	14.4	36.2
90	BDL		3.5	0.05	0.00	0.06	BDL		2.9	BDL		0.9	BDL		1.6	210.8	9.0	35.9
120	BDL		3.5	0.05	0.01	0.06	BDL		2.9	BDL		0.9	BDL		1.6	202.7	8.7	36.2
150	BDL		3.5	0.05	0.02	0.06	BDL		2.9	BDL		0.9	BDL		1.5	181.9	6.4	35.5
180	BDL		3.5	0.05	0.01	0.06	BDL		2.9	BDL		0.9	BDL		1.6	204.4	9.1	36.3
210	BDL		3.5	0.05	0.02	0.06	BDL		2.9	BDL		0.9	BDL		1.6	200.9	7.8	36.1
240	BDL		3.6	0.05	0.02	0.06	BDL		3.0	BDL		0.9	BDL		1.6	200.0	6.8	37.0
270	BDL		3.6	0.05	0.01	0.06	BDL		3.0	BDL		0.9	BDL		1.6	202.9	9.9	36.6
330	BDL		3.5	0.05	0.01	0.06	BDL		2.9	BDL		0.9	BDL		1.5	196.9	7.0	35.6
480	BDL		3.5	0.05	0.01	0.06	BDL		2.9	BDL		0.9	BDL		1.6	203.2	9.9	35.9
1320	BDL		3.5	0.05	0.01	0.06	BDL		2.9	BDL		0.9	BDL		1.6	208.0	10.2	36.0
1620	BDL		3.6	0.05	0.01	0.06	BDL		3.0	BDL		0.9	BDL		1.6	208.1	2.0	37.1
1650	BDL		3.6	0.05	0.01	0.06	BDL		3.0	BDL		0.9	BDL		1.6	204.9	5.7	36.6

Table C-2 (Continued). Concentrations (conc.) of elements in FPW as a function of time in Experiment CB based on ICP-MS analysis. Errors are reported as 1σ. Detection limit (DL) is sample-specific. BDL: below detection limit.

T (min)	Sr			As			Ba			Pb		
	Conc. (ppm)	Error (ppm)	DL (ppm)	Conc. (ppm)	Error (ppm)	DL (ppm)	Conc. (ppm)	Error (ppm)	DL (ppm)	Conc. (ppm)	Error (ppm)	DL (ppm)
0	855.7	28.7	20.8	BDL		1.2	3.6	0.2	1.3	BDL		0.05
5	859.6	27.8	21.1	BDL		1.3	3.5	0.1	1.3	BDL		0.05
10	841.3	20.1	20.5	BDL		1.2	3.4	0.1	1.3	BDL		0.05
15	799.7	17.2	21.2	BDL		1.3	3.2	0.1	1.4	BDL		0.05
20	813.1	31.0	21.2	BDL		1.3	3.2	0.1	1.4	BDL		0.05
25	851.9	22.0	21.1	BDL		1.3	3.3	0.1	1.3	BDL		0.05
30	783.6	15.0	20.6	BDL		1.2	3.3	0.1	1.3	BDL		0.05
40	793.8	16.0	20.9	BDL		1.3	3.3	0.1	1.3	BDL		0.05
50	828.6	13.1	21.1	BDL		1.3	3.5	0.1	1.3	BDL		0.05
60	815.8	29.3	20.9	BDL		1.2	3.4	0.2	1.3	BDL		0.05
90	820.7	32.2	20.7	BDL		1.2	3.4	0.2	1.3	BDL		0.05
120	826.8	31.4	20.9	BDL		1.2	3.3	0.2	1.3	BDL		0.05
150	764.8	22.1	20.5	BDL		1.2	3.2	0.1	1.3	BDL		0.05
180	807.9	36.6	20.9	BDL		1.3	3.3	0.1	1.3	BDL		0.05
210	795.0	38.0	20.8	BDL		1.2	3.2	0.2	1.3	BDL		0.05
240	802.3	22.4	21.3	BDL		1.3	3.4	0.1	1.4	BDL		0.05
270	826.8	24.9	21.1	BDL		1.3	3.3	0.1	1.3	BDL		0.05
330	809.7	15.6	20.6	BDL		1.2	3.2	0.05	1.3	BDL		0.05
480	812.8	21.4	20.7	BDL		1.2	3.3	0.1	1.3	BDL		0.05
1320	798.2	21.5	20.8	BDL		1.2	3.2	0.05	1.3	BDL		0.05
1620	810.8	31.7	21.4	BDL		1.3	3.3	0.05	1.4	BDL		0.05
1650	825.9	21.4	21.1	BDL		1.3	3.3	0.2	1.3	BDL		0.05

Table C-3. The concentrations (conc.) of trace elements in the precipitates from Experiment CA and CB in ppm. Analytical error is reported as 1 standard deviation. All values are reported as 3 significant figures.

Sample Name	Li		Mg		P		S		Ca	
	Conc. (ppm)	Error (ppm)	Conc. (ppm)	Error (ppm)	Conc. (ppm)	Error (ppm)	Conc. (ppm)	Error (ppm)	Conc. (ppm)	Error (ppm)
CA t = 0 min	< 99.2		1150000	18800	< 150		885	219	4800	50
CA t = 50 min	159	2	3780	150	< 59.5		9580	230	1020000	8000
CA t = 150 min	167	6	3140	190	< 87.9		9780	1140	922000	4000
CA t = 27.5 h	150	2	3640	140	< 70.6		15100	200	1130000	10000
CB t = 27.5 h	152	5	3610	130	< 73.2		15500	700	1080000	10000
	Ti		**Cr**		**Mn**		**Fe**		**Co**	
	Conc. (ppm)	Error (ppm)	Conc. (ppm)	Error (ppm)	Conc. (ppm)	Error (ppm)	Conc. (ppm)	Error (ppm)	Conc. (ppm)	Error (ppm)
CA t = 0 min	< 0.903		< 14.7		8790	90	900	39	< 9.91	
CA t = 50 min	< 0.361		< 5.88		2180	40	248	12	< 3.96	
CA t = 150 min	< 0.533		< 8.68		2180	30	201	21	< 5.85	
CA t = 27.5 h	< 0.429		< 6.98		2260	30	283	17	< 4.70	
CB t = 27.5 h	< 0.444		< 7.23		2470	60	290	12	< 4.87	
	Cu		**Zn**		**Br**		**Sr**		**As**	
	Conc. (ppm)	Error (ppm)	Conc. (ppm)	Error (ppm)	Conc. (ppm)	Error (ppm)	Conc. (ppm)	Error (ppm)	Conc. (ppm)	Error (ppm)
CA t = 0 min	81.0	8.9	2010	90	29400	2400	163	2	< 21.1	
CA t = 50 min	5.58	0.81	462	13	13200	760	20700	600	< 8.43	
CA t = 150 min	12.3	2.0	458	14	18500	1730	19600	400	< 12.5	
CA t = 27.5 h	17.5	1.2	664	24	15400	750	24300	600	< 10.0	
CB t = 27.5 h	6.78	1.67	659	24	14700	300	25800	500	< 10.4	
	Cd		**Ba**		**Pb**		**Ni**			
	Conc. (ppm)	Error (ppm)	Conc. (ppm)	Error (ppm)	Conc. (ppm)	Error (ppm)	Conc. (ppm)	Error (ppm)		
CA t = 0 min	< 4.43		13.4	4.6	67.5	0.2	< 5.38			
CA t = 50 min	< 1.77		178	4	24.9	0.1	< 2.11			
CA t = 150 min	< 2.61		182	3	23.2	0.3	< 3.12			
CA t = 27.5 h	< 2.10		272	9	28.6	0.3	< 2.51			
CB t = 27.5 h	< 2.18		264	7	27	0.4	< 2.60			